High-resolution spectroscopic view of planet formation sites

PhD Dissertation

Written by: Zsolt Regály

LORÁND EÖTVÖS UNIVERSITY, FACULTY OF SCIENCES
PHD SCHOOL OF PHYSICS
PHD PROGRAM OF PARTICLE- AND ASTROPHYSICS

Head of PhD School of Physics: Prof. Dr. Ferenc Csikor (Doctor of HAS)
Head of the PhD program: Prof. Dr. Ferenc Csikor (Doctor of HAS)

Associate supervisors: Prof. Dr. Cornelis Petrus Dullemond

Institut für Theoretische Astrophysik, Universität Heidelberg

Dr. Zsolt Sándor (PhD)

Max-Planck-Institut für Astronomie, Heidelberg

Dr. Péter Ábrahám (Doctor of HAS)

Konkoly Observatory of the Hungarian Academy of Sciences

Dr. László L. Kiss (Doctor of HAS)

Konkoly Observatory of the Hungarian Academy of Sciences

Loránd Eötvös University
Budapest, Hungary
2011

FOREWORD

As of writing we know about half thousand extrasolar planets (so-called exoplanets). The exoplanets as well as the planets in our Solar System are believed to emerge from the remnant material of nebular contraction forming circumstellar disks around pre-main sequence stars. In order to better understand the planet formation phenomena, detection of young planets still embedded in their host disk seems to be indispensable.

Despite the fact that planet formation should be a common phenomenon, only two young planet bearing systems are known to date. This might be accounted for multiple problems: First, although the amazing development of optical and infrared high-contrast imaging with adaptive optics aided 8 meter class telescopes, only extremely close young stellar objects can be spatially resolved; Second, radial velocity measurements aiming at detecting the reflex motion of the planet host stars may encounter difficulties, because young stars are very active. Thus, development of novel observational techniques which can overcome the difficulties mentioned would be important.

This PhD thesis presents an investigation on how to map the planet forming regions of protoplanetary disks with high-resolution near-infrared spectroscopy.

Contents

1. INTRODUCTION

During the star formation process pre-main sequence stars slowly evolve from a deeply embedded core to fully revealed stars. After the initial collapse of a dense core, the star enters the class 0/I phase in which it is rapidly accreting mass from its massive envelope. As the envelope dissipates the accretion rate decreases, the star enters the class II phase, where it becomes optically revealed and is slowly being fed by a viscously-evolving irradiated circumstellar accretion disk. The dust particles of the circumstellar disk eventually coalesce into planetesimals, while the gas dissipates from the system leaving a class III star. During this phase, planetesimals form terrestrial planets and cores of giant planets via mutual collisions over millions of years. As a planetary core becomes massive enough ($> 10 \, M_{\oplus}$), the run-away accretion of the disk's gas onto this solid core (consisting of rocky and icy materials) eventually leads to the formation of giant gas planet. Thus, the disks around young stars, also called protoplanetary disk, play a fundamental role both in the formation of stars and planets.

An important feature of protoplanetary disks is their relatively high column density in dust, which effectively blocks the stellar radiation at both optical and ultraviolet wavelengths. The gaseous component dominates the mass of the system, with the dust only contributing to roughly 1-2% of the total disk mass. The dynamics of the disk is thus almost completely dominated by the gas. On the other hand, the dust component is very important, as it dominates the opacity and, therefore, the emission properties of the disk (Lodato 2008). Due to the high dust opacity, the interstellar molecules, that would have short lifetimes against ultraviolet photodissociation in unshielded regions of space, are able to survive and proliferate. Most of the molecules observed in protoplanetary disks to date contain one or more carbon atoms. Since the cosmic abundance of oxygen exceeds that of carbon, it is no surprise that the relatively tightly bound carbon monoxide (CO) is the most abundant species after H_2 itself. Thus, the observations of CO, pursued since 1970, have yielded more information on star-forming regions than any other molecules (Stahler & Palla 2005).

The disk masses are generally estimated from submillimeter emission, since the dust emission

is usually optically thin at these wavelengths (Beckwith et al. 1990). A survey around solar mass stars in the Taurus-Auriga region revealed that the mass of disks are in the range of $0.0001\,M_\odot \lesssim M_{\rm disk} \lesssim 0.1\,M_\odot$ with a median value of $0.005\,M_\odot$ (Andrews & Williams 2005). However, in a recent survey by Andrews & Williams (2007), the median disk mass is found to be one order of magnitude larger. Taking into account that the stellar mass of these sources are in the range of $0.1\,M_\odot \lesssim M_* \lesssim 1\,M_\odot$, the median value of the stellar-to-disk mass ratio is in the range of $0.001\,M_\odot \lesssim M_{\rm disk} \lesssim 0.1\,M_\odot$.

The disk size can be inferred by spatially resolved imaging, usually done with submillimeter interferometry. Andrews & Williams (2007) found that protoplanetary disks extend up to $100\,{\rm AU}$ or even $1000\,{\rm AU}$ around low mass ($0.1\,M_\odot \lesssim M_* \lesssim 2\,M_\odot$) young stars. Disk sizes around high-mass stars ($M_* \gtrsim 2\,M_\odot$) or in the brown dwarf regime ($M_* \lesssim 0.1\,M_\odot$) are found to be smaller and larger, respectively.

The vertical size of the protoplanetary disk is determined by the equilibrium of the pressure of the gas and the vertical component of the gravitational force of the central star. Assuming hydrodynamical equilibrium, it turns out that protoplanetary disks are often geometrically thin. This means that the typical vertical thickness H is much smaller than the radial distance R measured from the central star. The standard value of the aspect ratio $H/R \simeq 0.05$ used in disk modeling for disks around small mass stars. Consequently, the hydrodynamical simulations of protoplanetary disks can be done with two-dimensional approximation.

During the evolution of the protoplanetary disk, its gas and dust contents are consumed because of mainly the accretion of disk material onto the central star, photoevaporation of the dust, and disk winds. Thus, the life time of protoplanetary disks can be estimated from the accretion rate inferred by the strength of gas emission lines formed near the inner edge of the disk (Lodato 2008). The typical value of the accretion rate is in the range of $10^{-9}\,M_\odot\,{\rm yr}^{-1} \lesssim \dot{M} \lesssim 10^{-7}\,M_\odot\,{\rm yr}^{-1}$ for disks around small mass stars. Note that occasionally the accretion rate increases dramatically ($\dot{M} \simeq 10^{-4}\,M_\odot\,{\rm yr}^{-1}$) and the star produces large outburst, which may lasts for several hundred years called FU Orionis phenomenon (Hartmann & Kenyon 1996), or less than several months for EXor phenomenon (Herbig 1977). Taking into account the median disk mass and the above quiescent accretion rate, one can conclude that the disk life time around a small mass stars is $\lesssim 10 \times 10^6\,{\rm yr}$. Thus, the time available for planet formation is fairly short.

The core-accretion scenario of planet formation (Bodenheimer & Pollack 1986; Pollack et al. 1996) predicts the birth of giant planets in the inner, dense, and gas-rich regions of the protoplanetary disks. These are the regions where strong near-infrared band ($4.7\,\mu$m) CO emission or

absorption is expected to form. Thus, high-resolution near-infrared spectra of protoplanetary disks provide us a tool to map the planet formation sites (Najita et al. 2003). Observations with reliable techniques such as radial velocity measurements or high-contrast direct imaging have so far been unable to confirm the presence of planets caught in formation. Consequently, the study on the inner part of protoplanetary disks by high-resolution near-infrared spectroscopy provides major clues to the understanding of the formation of extrasolar planets.

In order to model the near-infrared emission or absorption of carbon monoxide in protoplanetary disks, I developed a two-dimensional semi-analytical radiative transfer code. This code uses the double-layer flaring disk model of Chiang & Goldreich (1997), in which the disk is heated by the stellar irradiation and accretion processes. The incident stellar flux heats the disk atmosphere, and its dust content reprocesses the stellar light and irradiates the disk interior, while the accretion processes heats the disk interior directly. As a result, the near-infrared emission or absorption forms in the optically thin disk atmosphere above the optically thick disk interior within the confines of this double-layer disk model.

A planet embedded in protoplanetary disks exerts tidal torques on the disk and induces trailing spiral shocks (Lin & Papaloizou 1980; Goldreich & Tremaine 1980; Papaloizou & Lin 1984), which transport angular momentum, and material is pushed away from the planet. This process leads eventually to the opening of a gap in the disk. Viscous torques in the disk counteract the gravitational torques generated by the planet, leading to an equilibrium configuration. The radial extent of the gap depends on the mass of the planet, the magnitude of the viscosity and the pressure in the disk (Lin et al. 1993). For a disk around an ordinary T Tauri star, the critical mass for gap opening to occur is of the order of about one Jupiter mass (M_J) (Lin et al. 1993). Recent hydrodynamical simulations using homogeneous kinematic viscosity assumption (Nelson et al. 2000; Papaloizou et al. 2001; Kley & Dirksen 2006), have shown that the gap is not circular, rather elliptic in shape. The excitation of the Lindblad 3:1 resonances caused by the orbiting planet results in local disk eccentricity development, for which gas the orbit of gas parcels are elliptic (Kley & Dirksen 2006). My hydrodynamical simulations using the α-type viscosity prescription of Shakura & Sunyaev (1973) – a more reasonable assumption for the viscosity, than the homogeneous kinematic viscosity –, confirming the above mentioned disk eccentricity development, revealed that the local disk eccentricity causes supersonic velocity disturbances. Supersonic velocity disturbance of the orbiting gas is expected to distort the molecular line profiles (Horne 1995) that would be symmetric and double-peaked emerging from axisymmetric, circular Keplerian disks. Combining the results of the hydrodynamical simulations with the own developed

spectral code, the emergent molecular line profiles are found to be strongly distorted for a giant planet bearing disk. Observations of such distorted near-infrared line profiles would enable us to indirectly detect giant planets still embedded in their protoplanetary disk.

According to the theory of resonant excitation mechanisms in the circumstellar disks of close-separation young binaries (Lubow 1991a), the circumprimary disk (circumstellar disk formed around the primary star) becomes fully eccentric. In line with the previous numerical investigations (Kley et al. 2008), my hydrodynamical simulations (using α-viscosity prescription) confirmed that the orbits of gas parcels are eccentric everywhere in the circumprimary disk of medium-separation binaries ($10\,\mathrm{AU} \leq a_{\mathrm{bin}} \leq 50\,\mathrm{AU}$), i.e. the disk is globally eccentric. The average disk eccentricity is found to be $e_{\mathrm{disk}} \simeq 0.2$, independent of some important binary parameters such as the binary mass ratio and the magnitude of disk viscosity. The near-infrared molecular line profiles are expected to be strongly distorted, because the global disk eccentricity (concerning the entire disk for this case) causes supersonic velocity perturbations. My synthetic spectral line profile calculations using the results of my hydrodynamical simulations of circumprimary disk perturbations showed that the near-infrared molecular line profiles of carbon monoxide are significantly asymmetric. The peak-to-peak line profile asymmetry is found to be $\sim 20\%$ measured to the total line flux and varies on the time scale of the binary orbital period. I demonstrated that high-resolution near-infrared band (4.7 micron) carbon monoxide molecular spectra provide us a tool to reveal the disk eccentricity within the 3 AU regions, where planets are expected to form.

It is no doubt that the first glimpse at a giant planet being on birth would provide clues for planet formation theories. Furthermore, as the planet formation via core-accretion is strongly affected by the disk eccentricity in binaries as showed by recent numerical investigations (see, e.g., Zsom et al. (2011) and references therein), major consequences could be drawn to the core-accretion theory by observing and measuring disk eccentricity. Hence, the high-resolution near-infrared carbon monoxide spectra provided by contemporary or future high-resolution spectrographs such as CRIRES (CRiogenic high-resolution InfraRed Echelle Spectrograph) (Kaeufl et al. 2004) on the ESO-VLT (European Southern Observatory Very Large Telescope) or METIS (Mid-infrared E-ELT Imager and Spectrograph) on the planned E-ELT (European Extremely Large Telescope) could serve us a novel method to test and improve planet formation theories.

My PhD thesis is organized as follows. Chapter 2 gives a detailed description of physics behind the radiative transfer calculation implemented in my semi-analytical two-dimensional spectral code. Chapter 3 presents the accretion phenomena that so far are known to play major roles

in protoplanetary disks. The thermal disk model required for the calculation of molecular spectra formed in protoplanetary disks, known as the double-layer flaring disk model is presented in Chapter 4. My results concerning the detectability of giant planets still embedded in their protoplanetary disk and the detectability of the fully eccentric disk state in circumprimary disks of medium-separation young binaries are presented in Chapters 5 and 6, respectively. The thesis closes with the summary of my investigations and the proposed future works.

1. Introduction

2. MOLECULAR SPECTRA OF PROTOPLANETARY DISKS

Section 2.1 deals with the analytical solution of the radiative transfer equation that is used to model the molecular spectral lines of carbon monoxide (CO) emerging from protoplanetary disks. The strength of emission or absorption lines of CO gas in protoplanetary disks is determined by the temperature distributions, and the population of energy levels of CO, which is described in detail in Sect. 2.3 following the textbook of Rybicki & Lightman (1986). The intrinsic line profile emitted by a gas parcel of the disk is shaped by the thermal broadening. In this case the molecules are excited only by collisions due to their thermal motions in local thermodynamic equilibrium approximation, which is described in Sect. 2.4. Finally, Sect. 2.5 gives a short introduction to the formation of rotational-vibrational (ro-vibrational) spectra of the CO molecule following the text book of Stahler & Palla (2005).

2.1 Radiative transfer equation

The propagation of specific intensity along a ray s can be described by the change on specific intensity due to absorption and emission that can be expressed by the fundamental equation of radiative transfer theory, which can be written as

$$\frac{dI_\nu(s)}{ds} = j_\nu(s) - \chi_\nu(s)I_\nu(s), \tag{2.1}$$

where $I_\nu(s)$ is the monochromatic intensity, $\chi_\nu(s)$ and $j_\nu(s)$ are the absorption and emission of the medium at frequency ν, respectively. Let us define the monochromatic optical depth $\tau_\nu(s)$ along the beam as

$$\tau_\nu(s) = \chi_\nu(s)ds. \tag{2.2}$$

Thus, the $\tau_\nu = \tau_\nu(D)$ monochromatic optical depth of a medium with total thickness D is

$$\tau_\nu = \int_0^D \chi_\nu(s)ds. \tag{2.3}$$

With this definition of the optical depth, the radiative transport equation given by Eq. (2.1), can be rewritten as

$$\frac{dI_\nu(\tau_\nu)}{d\tau_\nu} = \frac{j_\nu(\tau_\nu)}{\chi_\nu(\tau_\nu)} - I_\nu(\tau_\nu). \tag{2.4}$$

This equation can be represented by a first order linear differential equation of the form

$$\frac{dy}{dx} + p(x)y = q(x). \tag{2.5}$$

The general solution to this equation is

$$y = \frac{\int u(x)q(x)dx + C}{u(x)}, \ \ u(x) = e^{\int p(x)dx}, \tag{2.6}$$

where I introduced the following variables

$$x \equiv \tau_\nu, \ y \equiv I_\nu(\tau_\nu), \ p(x) \equiv 1, \ q(x) \equiv B_\nu(T). \tag{2.7}$$

Thus, using the standard notation of the source function of the emission as $S_\nu(\tau_\nu) = j_\nu(\tau_\nu)/\chi_\nu(\tau_\nu)$, we obtain the analytical solution to the radiative transfer problem described by Eq. (2.4), which is

$$I_\nu(\tau_\nu) = I_\nu(0)e^{-\tau_\nu} + \int_0^{\tau_\nu} S_\nu(\tau')e^{-(\tau_\nu - \tau')}d\tau', \tag{2.8}$$

where the intensity at the origin of radiation is $I_\nu(0)$. This formula describes the intensity along a ray passed through a medium with τ_ν optical depth at frequency ν.

2.2 Solution to radiative transfer in homogeneous medium

In a medium with density of $\rho(s)$ along the propagation path of the radiation s, the absorption at a given frequency ν can be given by

$$\chi_\nu(s) = \rho(s)\kappa_\nu, \tag{2.9}$$

where κ_ν is defined as the monochromatic mass absorption coefficient of the medium, i.e., the specific absorption coefficient of the medium measured in units of $\mathrm{cm}^2\,\mathrm{g}^{-1}$. Here I assume that the mass absorption coefficient is constant in the medium along the ray, i.e., $\kappa_\nu(s) = \kappa_\nu$. Thus, using Eq. (2.3), the optical depth along the ray can be given as

$$\tau_\nu = \int_0^D \rho(s)\kappa_\nu ds = \kappa_\nu \int_0^D \rho(s) = \kappa_\nu \Sigma, \tag{2.10}$$

where Σ is density integrated along the ray, which can be interpreted as the surface mass density.

Assuming that the investigated medium radiates as a blackbody, its radiation can be described by the Planck function:

$$B_\nu(T) = \frac{2h\nu^3}{c^2}\frac{1}{e^{\frac{h\nu}{kT}} - 1}, \tag{2.11}$$

where k, h and c are the Boltzmann, Planck constants and the light speed, respectively. If this medium is in local thermodynamical equilibrium (LTE), the emitted and absorbed energy equilibrates. For this case $dI_\nu(\tau_\nu)/d\tau_\nu = 0$, and using Eq. (2.4), we obtain

$$S_\nu(\tau_\nu) = \frac{j_\nu(\tau_\nu)}{\chi_\nu(\tau_\nu)} = I_\nu(\tau_\nu) = B_\nu(T), \tag{2.12}$$

which is known as the *Kirchhoff's law*.

Applying Eq. (2.12), the source function S_ν in Eq. (2.8) can be replaced by the Planck function, and finally the solution to the radiative transfer problem (Eq. 2.8) can be explicitly expressed as

$$\boxed{I_\nu = I_\nu(0)e^{-\kappa_\nu\Sigma} + B_\nu(T)(1 - e^{-\kappa_\nu\Sigma}).} \tag{2.13}$$

This equation describes that the originally emitted intensity $I_\nu(0)$ is decreased due to the absorption of the medium (first term), while increased due to the emission of the medium (second term).

2.3 Mass absorption coefficient

In order to solve Eq. (2.13) we have to know the monochromatic mass absorption coefficient κ_ν of the gas, which is determined by the line emission and absorption processes. Let us consider a simple two level atomic system with energy $\varepsilon_\mathrm{u} = \varepsilon_\mathrm{l} + h\nu_0$, where ε_u and ε_l denote the upper and lower level energy states, respectively. The atomic system changes its energy state from l to u via absorbing, while back to l from u via emitting a photon with frequency ν_0. According to Einstein's theory three processes can occur during this transition.

2. Molecular spectra of protoplanetary disks

- **Spontaneous emission** occurs when the system drops from the higher energy state u to the lower energy state l spontaneously resulting in emission of a photon. The transition probability for spontaneous emission per unit time is defined by A_{ul}.

- **Absorption of a photon** with frequency ν_0 occurs in the presence of a radiation field and resulting in that the system goes from the lower energy state l to the higher energy state u. It is reasonable to expect that the probability of this transition is proportional to the mean intensity $\bar{J}$ (which is the intensity averaged over all directions) at frequency ν_0, defined as

$$\bar{J} = \frac{1}{4\pi} \int_0^\infty \int_0^{2\pi} \int_0^\pi I_\nu \sin(\theta) d\theta d\varphi \phi_\nu d\nu. \tag{2.14}$$

  Thus, the transition probability for absorption of a photon per unit time is given by $B_{lu}\bar{J}$. The line profile function ϕ_ν in Eq. (2.14) describes the relative effectiveness of neighboring frequencies of ν_0 for causing transition (see details in Sect. 2.4).

- **Stimulated emission** resulting in a transition from the higher energy state u to the lower energy state l. The excitation to the higher energy state was previously due to the absorption of a photon with frequency ν_0. The transitional probability is also proportional to the mean intensity. Thus, the transition probability of stimulated emission is given by $B_{ul}\bar{J}$.

In local thermodynamic equilibrium, the number of transitions per unit time per unit volume from a given state is equal to that to the same state. Let the number of atoms in state l and u n_l and n_u, respectively, we can write that

$$n_u A_{ul} = n_u B_{lu}\bar{J} - n_l B_{lu}\bar{J}, \tag{2.15}$$

taking into account the three transition processes mentioned above. The rate of level populations – the ratio of the number of species in upper (n_u) and lower (n_l) level states – in local thermodynamic equilibrium can be given by

$$\frac{n_u}{n_l} = \frac{g_l e^{-\varepsilon_l/kT}}{g_u e^{-(\varepsilon_l + h\nu_0)/kT}} = \frac{g_u}{g_l} e^{-\frac{\varepsilon_u - \varepsilon_l}{kT}}, \tag{2.16}$$

The Einstein coefficients (A_{ul}, B_{ul} and B_{lu}) are coupled to each other. Using Eqs. (2.15), (2.16), and due to the fact that in local thermodynamical equilibrium $\bar{J} = B_\nu(T)$ must be valid for all temperatures, the Einstein coefficients must be coupled by the following relations

$$B_{ul} = \frac{c^2}{2h\nu_0^3} A_{ul}, \quad B_{lu} = \frac{g_u}{g_l} B_{ul}. \tag{2.17}$$

Since the values A_{ul}, B_{lu}, and B_{lu} have no any reference to the temperature, Eq. (2.17) holds for non thermodynamic equilibrium, as well.

The energy absorbed out of a beam in frequency range $d\nu$, solid angle $d\Omega$, unit time dt by a surface element dA is

$$dE = dA\,ds\,dt\,d\Omega\,d\nu \frac{h\nu_0}{4\pi} n_1 B_{lu} \phi_\nu I_\nu, \tag{2.18}$$

thus, the absorption in Eq. (2.1) of the gas is

$$\chi_\nu(s) = \frac{h\nu}{4\pi} n_l B_{lu} \phi_\nu, \tag{2.19}$$

where we apply the relation between energy and intensity: $dE = I_\nu dA\,dt\,d\Omega\,d\nu$. To take into account the stimulated emission, let us assume that it is proportional to the intensity and only affects the photons along the given beam, in close analogy to the process of absorption. Thus, the stimulated emission is taken into account as a negative absorption. As a consequence, the absorption coefficient of the gas corrected for stimulated emission is

$$\chi_\nu(s) = \frac{h\nu}{4\pi}(n_l B_{lu} - n_u B_{ul})\phi_\nu, \tag{2.20}$$

and the monochromatic mass absorption coefficient defined by Eq. (2.9) can be given as

$$\kappa_\nu = \frac{1}{m_{\mathrm{mol}} n} \frac{h\nu}{4\pi}\left(n_1 B_{\mathrm{lu}} - n_u B_{\mathrm{ul}}\right)\phi_\nu. \tag{2.21}$$

Here we assume a homogeneous medium, i.e. $\rho(s) = m_{\mathrm{mol}} n$, where m_{mol} and n are the mass and number density of molecules in gas, respectively, are constant along the propagation of the radiation. Assuming only thermal excitation, the total number of the molecules, i.e. the number density, is the sum of molecules being in the ith state

$$n = \sum_i n_i = \frac{n_0}{g_0} \sum_i g_i e^{-\frac{\varepsilon_i - \varepsilon_0}{kT}}, \tag{2.22}$$

where n_i is the number of species in ground and i'the excitation state, the expression $\varepsilon_i - \varepsilon_0$ is the excitation potential of the i'th excitation level and ε_0 is the energy of ground state level. Defining Q_{T} as the partition function

$$Q_{\mathrm{T}} = \sum_i g_i e^{-\frac{\varepsilon_i - \varepsilon_0}{kT}}, \tag{2.23}$$

11

TABLE 2.1: Constants for calculating Q_T of $C^{12}O^{16}$.

c_i	value
c_0	1.17133×10^1
c_1	3.01374×10^{-1}
c_2	5.68592×10^{-5}
c_3	1.10085×10^{-8}

the level population of the ith excited state can be expressed by

$$n_i = n \frac{g_i}{Q_T} e^{-\frac{\Delta \varepsilon_i}{kT}}. \tag{2.24}$$

Since my disk model follows semi-analytical approach in a sense that the temperature of emitting gas is given analytically, while the intensity of radiation is calculated numerically at each disk parcels, it is expedient to find an approximate formula for Q_T as a function of temperature T in a polynomial form, given by

$$Q_T = \sum_i c_i T^i. \tag{2.25}$$

Quadratic coefficients c_i for the $^{12}C^{16}O$ molecule are shown in Table 2.1, the calculation is based on transitional parameters given by Goorvitch (1994).

Combining Eqs. (2.21), (2.17), and (2.24), and taking into account spontaneous emission, absorption and stimulated emission of radiation, the monochromatic mass absorption coefficient of the gas at temperature T for a given transition at frequency ν_0 can be expressed as

$$\kappa_\nu = \frac{1}{m_{mol}} \frac{1}{8\pi} \frac{1}{Q_T} \left(\frac{c}{\nu_0} \right)^2 A_{ul} g_u \left(e^{-\frac{\varepsilon_l}{kT}} - e^{-\frac{\varepsilon_u}{kT}} \right) \phi_\nu, \tag{2.26}$$

where A_{ul} is the spontaneous emission probability, ε_l and ε_u are the energy of lower and upper states, respectively.

2.4 Intrinsic line profile

Now let us determine the intrinsic line profile function ϕ_ν required to calculate the monochromatic absorption coefficient given in Eq. (2.26). First, we examine the Doppler line broadening caused

by the thermal motion of emitting molecules in the gas. The frequency of the emitted radiation of the moving molecule in its own frame (ν_0) corresponds to a different frequency for an observer ($\nu_0 \pm \Delta\nu$). As a result, the line emitted by a certain amount of gas is broadened without change in the net flux. Assuming that $v/c \ll 1$, the Doppler shift of the emission of a molecule moving with line-of-sight velocity v is $\nu - \nu_0 = \nu_0(v/c)$, where v is the apparent velocity of the molecule in the observer's frame, c is the speed of light. Assuming the Maxwell speed distribution, the number of molecules $N(v)$ in the velocity range $v + dv$ is

$$N(v) = e^{-\frac{m_{mol}v^2}{2kT}} dv. \tag{2.27}$$

Using the definition of the Doppler shift one can derive that $dv = c\, d\nu/\nu_0$, thus the number of atoms emitting in the frequency range $\nu_0 + d\nu$ is

$$N(\nu) = e^{-\left(\frac{c}{\nu_0}\right)^2 \frac{m_{mol}}{2kT}(\nu - \nu_0)^2}. \tag{2.28}$$

Since the strength of the emission is proportional to $N(\nu)$, i.e., $\phi_\nu \sim N(\nu)$, the intrinsic line profile ϕ_ν for thermal broadening is a Gaussian function:

$$\phi_\nu = \frac{1}{\sigma\sqrt{\pi}} e^{-\left(\frac{\nu - \nu_0}{\sigma}\right)^2}. \tag{2.29}$$

Note that with normalization factor $1/\sigma\sqrt{\pi}$ in Eq. (2.29), the line profile function is normalized such that $\int \phi_\nu d\nu = 1$. In Eq.(2.29) σ is the line width at half maximum caused by the thermal broadening, which can be given as

$$\sigma = \sigma_T = \frac{\nu_0}{c}\sqrt{\frac{2kT}{m_{mol}}}. \tag{2.30}$$

Considering additional broadening, e.g., due to the turbulent motions of the gas parcels, the resulting line profile is the convolution of natural and turbulent broadened line profiles. Consequently, the resulting line profile is also a Gaussian function with half width at maximum $\sigma_{tot} = (\sigma_T^2 + \sigma_{turb}^2)^{1/2}$, where σ_T and σ_{turb} are the thermal and turbulent broadening. The turbulent broadening at line center depends on the turbulent velocity, which is

$$\sigma_{turb} = \eta\sqrt{\frac{\gamma kT}{m_{gas}}} \tag{2.31}$$

for an ideal gas with adiabatic index γ, assuming that the turbulent velocity is η times the sound speed measured in the gas. Similarly to expression of thermal broadening given by Eq.(2.30), the

turbulent broadening can be given as

$$\sigma_{\text{turb}} = \frac{\nu_0}{c}\eta\sqrt{\frac{\gamma}{2}\frac{m_{\text{mol}}}{m_{\text{gas}}}}\sigma_T.$$

(2.32)

Combining Eqs. (2.30) and (2.32), the line profile width at half maximum due to thermal and turbulent broadening is

$$\sigma_{\text{tot}} = \frac{\nu_0}{c}\sqrt{1 + \alpha^2\frac{\gamma}{2}\frac{m_{\text{CO}}}{m_{\text{H}_2}}}\sqrt{\frac{2kT}{m_{em}}},$$

(2.33)

where we assume that the main constituent of the gas of protoplanetary disk is the hydrogen with atomic mass m_{H_2}, and the examined emitting constituent of the gas is the carbon monoxide with molecular mass m_{CO}.

In a protoplanetary disk the gas orbits the central star causing additional change in the line-of-site velocity of emitting gas parcels relative to the observer. As a result, the line emitted by a parcel of gas is Doppler-shifted with $\Delta\nu$ relative to the fundamental frequency ν_0. Taking into account the orbital flow of the gas, the intrinsic line profile function of emitting gas in protoplanetary disks is

$$\phi_\nu = \frac{1}{\sigma_{\text{tot}}\sqrt{\pi}}e^{-\left(\frac{\nu-\nu_0+\Delta\nu}{\sigma_{\text{tot}}}\right)^2}.$$

(2.34)

2.5 Ro-vibrational transitions of CO molecule

An important feature of protoplanetary disks is their relatively high column density in dust, which effectively blocks the stellar radiation at both optical and ultraviolet wavelengths. Hence, interstellar molecules, that would have short lifetimes against ultraviolet photodissociation in unshielded regions of space, are able to survive and proliferate. Most of the molecules observed to date contain one or more carbon atoms. Since the cosmic abundance of oxygen exceeds that of carbon, it is no surprise that the relatively tightly bound CO is the most abundant species after H_2 itself. Thus, the observations of CO, pursued since 1970, have yielded more information on star-forming regions than any other molecules (Stahler & Palla 2005).

Contrary to atoms, for which only the energy of the electrons intervene in the transitions, molecules have three types of transitions: electronic, vibrational and rotational (Lequeux 2005). The total energy of a molecule is the sum of its rotational, vibrational, and electronic contributions:

$$E_{\text{tot}} = E_{\text{rot}} + E_{\text{vib}} + E_{\text{el}}.$$

(2.35)

In quantum mechanics, the kinetic energy of a dumbbell[1] rotating about an axis through the center of mass and perpendicular to the plane of rotation, can be given by

$$E_{\text{rot}} = \frac{\hbar^2}{2I} J(J+1),$$ (2.36)

while the energy of a simple harmonic oscillator of fundamental frequency ν_0 can be given by

$$E_{\text{vib}} = \hbar 2\pi\nu_0 \left[\left(V + \frac{1}{2} \right) - x \left(V + \frac{1}{2} \right)^2 \right],$$ (2.37)

where J and V are the rotational and vibrational quantum numbers, respectively, and I denotes the moment of inertia of the molecule. The electronic transitions of molecules are the equivalent of the atomic transitions. Their energy is of order of several eV, and resulting in photon emission/absorption generally in the far-ultraviolet wavelengths. For the harmonic oscillator, the selection rule for vibrational transitions is $\Delta V = \pm 1, \pm 2$, etc.. The rotation of the dumbbell around the principal axis of inertia, thus the allowed transitions are $\Delta J \pm 1, \pm 2$, etc.. While vibrational energies are typically a fraction of eV, and the corresponding emission/absorption wavelengths are in the near-infrared, the rotational energies associated with rotation are of the order of the meV and the corresponding wavelengths are in the submillimeter to centimeter range (Lequeux 2005).

In environments where vibrational states are excited, the molecule relaxes through ro-vibrational transitions, in which both J and V change. When observed in low resolution, each electronic transition of a molecule is resolved as a broad band spectrum resulting from the superposition of all the rotational and vibrational lines, called ro-vibrational lines. While the CO molecule has a permanent electric dipole moment, electric dipole transitions can occur. The $J = 1$ state is elevated above the ground state in $^{12}C^{16}O$ by an equivalent temperature of only $5.5\,\text{K}$. It is therefore easy to excite this level inside a quiescent cloud and even to populate $J = 2$, which lies $16\,\text{K}$ above the ground state. When the $J = 1 \rightarrow 0$ transition is made radiatively, the emitted photon has a wavelength of $2.60\,\text{mm}$.

As can be seen in Eq. (2.37), E_{vib} does not increase precisely as $V + 1/2$, but contains a relatively small negative term proportional to $(V + 1/2)^2$. As a consequence, the frequencies of photons emitted by the transitions with $V = 1 \rightarrow 0, 2 \rightarrow 1$, etc., decrease slowly with the starting V-value. Such fundamental vibrational transitions have the largest possibility, however other overtone transitions with $\Delta V = \pm 2, \pm 3$, etc. also occur. Each band corresponds to a pair of vibrational quantum numbers, say V' and V'', while the lines within a band are individual

---

[1]The CO molecules can be modeled as a dumbbell shaped mass distribution.

ro-vibrational transitions. The spacing between these lines gradually decreases toward higher frequencies. Eventually, the lines merge in a band head (Stahler & Palla 2005).

For downward dipole transitions within the same vibrational state $(J \rightarrow J - 1)$, Eq. (2.36) predicts that ΔE_{rot} is proportional to J, so that the lines are equally spaced. However, a CO molecule in a higher V-state has a slightly larger average separation between atoms. Its moment of inertia, I, is therefore greater. If V' and V'' denote the upper and lower vibrational states, respectively, then the $J \rightarrow J - 1$ transition now yields an energy of

$$\Delta E(V', V'') = \Delta E_{\text{vib}}(V', V'') + \frac{\hbar^2}{2} \left[\left(\frac{1}{I(V')} + \frac{1}{I(V'')} \right) J - \left(\frac{1}{I(V')} - \frac{1}{I(V'')} \right) J^2 \right],$$
(2.38)

where $J = 1, 2, 3$, etc., and $\Delta E_{\text{vib}}(V', V'')$ is the energy difference between two vibrational levels, where $J = 0$. Note that $J = 0 \rightarrow 0$ dipole transitions do not exist, so that the band contains a gap at the corresponding frequency. Since $I(V'')$ is slightly smaller than $I(V')$, Eq. (2.38) shows that the frequencies of the $J \rightarrow J - 1$ lines, known collectively as the R-branch of the band, increase, reach a maximum, and then begin to decline with higher J. For the fundamental $V = 1 \rightarrow 0$ band, this maximum is reached at $\lambda = 4.30 \, \mu$m, while it occurs at $2.29 \, \mu$m in the first overtone $V = 2 \rightarrow 0$ band. The lines from $J - 1 \rightarrow J$ fall on the other side of the central gap, which lies to the right of the spectrum. The energies in this P-branch are

$$\Delta E(V', V'') = \Delta E_{\text{vib}}(V', V'') + \frac{\hbar^2}{2} \left[- \left(\frac{1}{I(V')} + \frac{1}{I(V'')} \right) J + \left(\frac{1}{I(V')} - \frac{1}{I(V'')} \right) J^2 \right],$$
(2.39)

where, again, $J = 1, 2, 3$, etc. Because of the sign change inside square brackets of Eq. (2.39), the frequency falls below the gap for any J. The spacing between successive lines widens, and there is no convergence to a band head.

Figure 2.1 shows the fundamental band ro-vibrational emission spectra of the $^{12}\text{C}^{16}\text{O}$ molecule. In this fundamental band $\Delta V = \pm 1$, and the spectrum lies between $4.3 \, \mu\text{m} \leq \lambda \leq 5.3 \, \mu\text{m}$. The so-called band head ro-vibrational emission spectra of $^{12}\text{C}^{16}\text{O}$ is shown in Fig. 2.2. In the band head $\Delta V = \pm 2$, and the spectrum lies in the range of $2.29 \, \mu\text{m} \leq \lambda =\leq 2.5 \, \mu\text{m}$.

FIGURE 2.1: Emission spectra of $^{12}C^{16}O$ molecule in the fundamental ro-vibrational band for $V = 1 \rightarrow 0$ (*black*), $V = 2 \rightarrow 1$ (*blue*) and $V = 3 \rightarrow 2$ (*red*), assuming local thermodynamical equilibrium at temperatures 1000 K (*upper panel*) and 2000 K (*lower panel*). Each ro-vibration band has a left and a right sided branch, called R and P branch, respectively. The intensity of spectral lines are normalized to the strongest fundamental ($V = 1 \rightarrow 0$) line intensity. As the excitation energy increases for higher vibrational bands ($V = 2 \rightarrow 1$, $V = 3 \rightarrow 2$), the line intensities decrease. It is apparent that the higher excitation transitions ($V = 2 \rightarrow 1$, $V = 3 \rightarrow 2$) strengthen relative to the fundamental band ($V = 1 \rightarrow 0$) as the temperature is increasing.
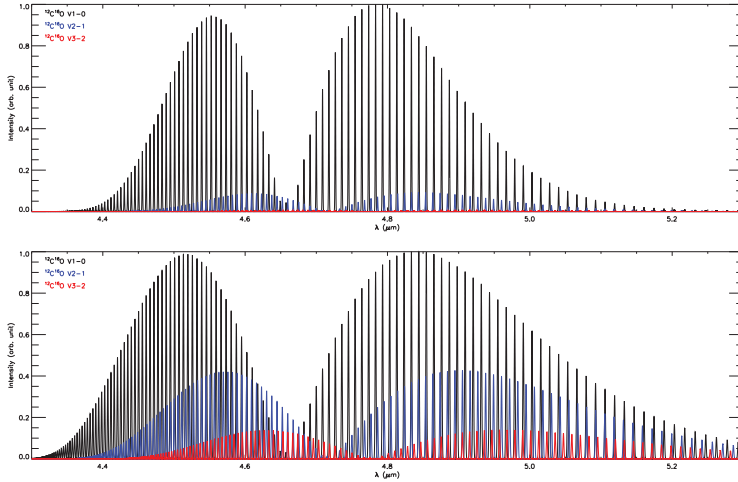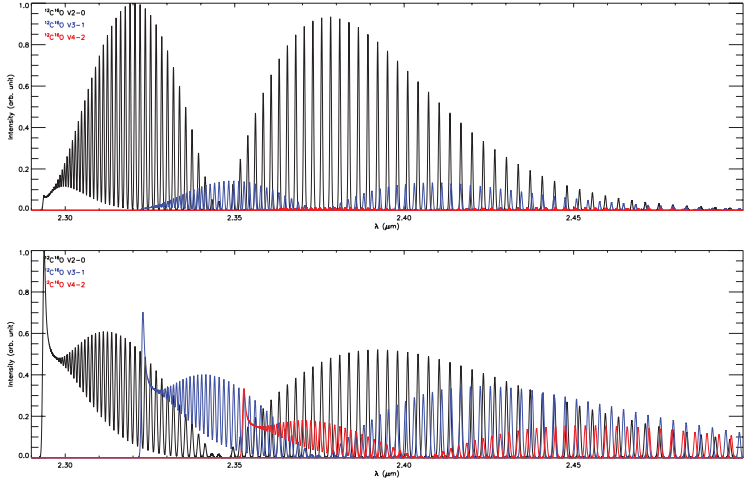
FIGURE 2.2: Emission spectra of $^{12}C^{16}O$ molecule in the band head ro-vibrational band for $V = 1 \rightarrow 0$ (*black*), $V = 2 \rightarrow 1$ (*blue*) and $V = 3 \rightarrow 2$ (*red*), assuming local thermodynamical equilibrium at temperatures $1000\,K$ (*upper panel*) and $2000\,K$ (*lower panel*). Similarly to the fundamental bands, each ro-vibration transition has a left and a right side branch, called R and P branch, respectively. The intensity of spectral lines was normalized to the strongest band head ($V = 2 \rightarrow 0$) line intensity. As the excitation energy increases for higher vibrational bands ($V = 3 \rightarrow 1$, $V = 4 \rightarrow 2$), the line intensities decrease. The intensity of high excitation transitions increases with temperature as for the fundamental band. It is evident that the lower the wavelength (the higher the energy of emitted photon), the smaller the distance between the lines, which is more apparent for high temperature spectra.

3. ACCRETION PROCESS IN DISKS

In order to determine the population levels of the investigated molecules, which is required to calculate the monochromatic mass absorption coefficient for a given ro-vibrational transition defined by Eq. (2.26), the thermal disk structure must be known in the protoplanetary disks. In a simplest scenario, the protoplanetary disks are non-irradiated, in which case the heating is provided by the gas accretion in the disk midplane. For isothermal disks, the accretion process can be described by the system of hydrodynamical differential equations of an ideal fluid presented in Sect. 3.1. Section 3.2 is dealing with the governing equation of the viscous evolution of the protoplanetary disks. The simplest analytical solution to the viscous evolution, the so-called steady state accretion disk, and the temperature distribution developed by viscous heating, are presented in Sect. 3.3. The discussion on the accretion processes presented in this Chapter follows the text book of (Frank et al. 2002). The origin of the viscosity is still a matter of debate, and its value cannot be determined directly from the assumed physical processes yet. A simple parametrization of the disk's viscosity, which is based on a dimensional analysis, known as α prescription described in Sect. 3.4 following the paper of Lodato (2008).

3.1 Hydrodynamic governing equations

The viscous evolution of protoplanetary disks can be described by the basic equations of viscous fluid dynamics. These are the continuity equation

$$\frac{\partial \rho}{\partial t} + \nabla(\rho \mathbf{u}) = \mathbf{0}, \tag{3.1}$$

and the Navier–Stokes equation

$$\frac{\partial \mathbf{u}}{\partial t} + \mathbf{u} \cdot \nabla(\mathbf{u}) = \frac{1}{\rho} \mathbf{P} - \nabla \mathbf{\Phi} + \nu \left[\nabla^2 \mathbf{u} + \frac{1}{3} \nabla(\nabla \cdot \mathbf{u}) \right], \tag{3.2}$$

where ρ and $\mathbf{u}$ are the density and velocity distribution of the fluid, P, $\Phi = -GM/r$ and ν are the pressure, the gravitational potential of the central star, and the kinematic viscosity of the fluid.

3. Accretion process in disks

For isothermal case, the equation of state of the gas determines the pressure as $P = P(\rho)$. However, for non-isothermal case, $P = P(\rho, T)$, hence taking into account the energy conservation equation is also needed to solve the system of differential equation. In the following, isothermal case is assumed. Here we neglect the disk self-gravity as the disk mass (being in the range $0.001\, M_* \leq M_{\mathrm{disk}} \leq 0.1\, M_*$ for an ordinary T Tauri disks, (Andrews & Williams 2005, 2007)) is negligible compared to that of the central star. The expression in brackets of the right hand side of Eq. (3.2) is the stress tensor σ. Note that the bulk viscosity of the fluid can usually be neglected in astrophysical fluids – the important exception to this being in shocks –, thus the stress tensor in Eq. (3.2) does not incorporate the bulk viscosity.

Accretion disks are often assumed to be geometrically thin, thus we can neglect the vertical motions. In this case, the fluid motions can be described in two-dimensional cylindrical coordinate system centered on the central star. Neglecting the fluid motions into vertical directions, the density could be vertically integrated to a thin surface represented by the so-called surface density $\Sigma(R, \phi) = \int_{-\infty}^{+\infty} \rho(R, \phi, z) dz$. In this approximation, $\Sigma = \Sigma(R, \phi)$ and $\mathbf{u} = u_R(R, \phi)\mathbf{i}_R + u_\phi(R, \phi)\mathbf{i}_\phi$, where $\mathbf{i}_R$ and $\mathbf{i}_\Phi$ are unit vectors into the radial and azimuthal directions, respectively. Similarly to the surface density, the stress tensor σ also must be vertically integrated leading to the vertically integrated stress tensor τ.

For the sake of simplicity, let us assume that the disk is axisymmetric. In this case, the continuity equation (Eq. 3.1) can be written as

$$\frac{\partial \Sigma}{\partial t} + \frac{\partial}{\partial R}(R\Sigma u_R) = 0. \tag{3.3}$$

Assuming axisymmetry, the pressure and the gravitational force give no contribution to the azimuthal direction (ϕ) component of Navier-Stokes equation, thus the azimuthal component of the momentum change is

$$\Sigma \left(\frac{\partial v_\Phi}{\partial t} + \frac{v_R v_\Phi}{R} + v_R \frac{\partial v_\Phi}{\partial R} \right) = \frac{1}{R^2} \frac{\partial}{\partial R} \left(R^2 \tau \right). \tag{3.4}$$

Note that the last two terms in the left hand side bracket appear due to the form of the operator $\mathbf{u}\nabla$ in cylindrical coordinate system. Combining Eq. (3.4) with the continuity equation Eq. (3.1) one can get

$$\frac{\partial}{\partial t} \left(\Sigma R v_\Phi \right) + \frac{1}{R} \frac{\partial}{\partial R} \left(R^2 v_R \Sigma v_\Phi \right) = \frac{\partial}{\partial R} \left(R^2 \tau \right). \tag{3.5}$$

To describe the gas accretion, the magnitude of angular momentum transfer per unit time, i.e., the torque has to be known. In the basic model of Hartmann (1998), the turbulent elements of gas moving at typical random velocity v_{turb} travel a mean free path λ before mixing with other material. Thus, the net torque is the different momenta of two streams of material; one from material originating at $R - \lambda/2$ and moving outward across R to mix with other material originating at $R + \lambda/2$; and the other starting at $R + \lambda/2$ and moving inward across R to mix with the inner annulus at $R - \lambda/2$. Assuming that the material in the vertical direction can be averaged, thus has surface density Σ, and moving with turbulent velocity v_{turb}, the material originating at $R - \lambda/2$ has an angular momentum of

$$J_{\text{in}} = v_{\text{turb}}\Sigma \left(R - \frac{\lambda}{2} \right)^2 \left[\Omega(R) - \frac{\lambda}{2} \left(\frac{d\Omega}{dR} \right) \right], \tag{3.6}$$

while the outer material has angular momentum of

$$J_{\text{out}} = v_{\text{turb}}\Sigma \left(R + \frac{\lambda}{2} \right)^2 \left[\Omega(R) + \frac{\lambda}{2} \left(\frac{d\Omega}{dR} \right) \right]. \tag{3.7}$$

If we adopt the assumption of that the streamwise momentum is conserved during the motion of elements, then the net outward transfer of angular momentum across R per unit length to first order in λ is

$$J_{\text{in}} - J_{\text{out}} = -\Sigma v_{\text{turb}}\lambda R^2 \frac{d\Omega}{dR}, \tag{3.8}$$

where we assume that the net inward motion of material in comparison with turbulent velocity is small, and λ is short distance compared with the scale over which Ω varies significantly. With this result, the net torque is

$$J = -2\pi R \Sigma v_{\text{turb}}\lambda R^2 \frac{d\Omega}{dR}. \tag{3.9}$$

As a consequence, decreasing angular velocity with radius, as the case in Keplerian disk, leads to outward flux of angular momentum. In Eq. (3.9), $v_{\text{turb}}\lambda$ can be considered as the kinematic viscosity ν. Note however that the expression $\nu = v_{\text{turb}}\lambda$, which can be identified as collisional viscosity, would result in too low bulk viscosity for protoplanetary disk contradicting the observations, see details in Sect. 3.4.

3.2 Accretion induced diffusion

The change in the angular momentum per unit mass at a distance R is equal to the torque exerted by viscous forces at that distance. In the simplest case, the vertically integrated stress tensor (τ) can be approximated as the only non vanishing component of stress tensor (σ) in a circular shearing flow is the $(R\Phi)$ component, proportional to the rate of strain $Rd\Omega/dR$. Thus, applying the relationship between the torque and stress ($\tau_{R\Phi} = J/2\pi R^2$) Eq. (3.9) leads to

$$\tau_{R\Phi} = \Sigma\nu R\frac{d\Omega}{dR}, \tag{3.10}$$

where we assume that the kinematic viscosity is expressed as $\nu = v_{\text{turb}}\lambda$. Taking into account that the only non-vanishing component of the torque is $\tau_{R\Phi}$, Eq. (3.5) can be rewritten as

$$\frac{\partial}{\partial t}\left(\Sigma R^2\Omega\right) = \frac{1}{R}\frac{\partial}{\partial R}\left(\Sigma v_R R^3\Omega\right) = \frac{1}{R}\frac{\partial}{\partial R}\left(\nu\Sigma R^3\frac{d\Omega}{dR}\right), \tag{3.11}$$

which yields

$$\frac{\partial\Sigma}{\partial t} = \frac{3}{R}\frac{\partial}{\partial R}\left[\sqrt{R}\frac{\partial}{\partial R}\left(\nu\Sigma\sqrt{R}\right)\right]. \tag{3.12}$$

As one can see, the evolution of the surface density can be described by a diffusion equation, and the evolution of disks is determined only by the kinematic viscosity ν.

3.3 Viscous heating in steady state accretion

In what follows, the steady state solution to the Eq. (3.12) is described (see more details in Lodato (2008)). Equation (3.3) represents the constant inflow of mass through each point of the disk, which process is called steady accretion. For this case, the accretion rate is defined as $\dot{M} = 2\pi\dot{\Sigma}Rdr$. Azimuthal integration of Eq. (3.3) for 2π, leads to accretion rate of

$$\dot{M} = -2\pi R\Sigma v_R, \tag{3.13}$$

where the inflow velocity is defined as $v_R < 0$ for inward direction flow. Analogously, azimuthal integration of Eq. (3.5) yields

$$\dot{M}\Omega R^2 + 2\pi\Sigma v R R^3\Omega = 2\pi\nu\Sigma R^3\frac{d\Omega}{dR}, \tag{3.14}$$

The first term in the left hand side of Eq. (3.14) represents the angular momentum advected due to accretion process, while the right hand side is the outward angular momentum flux due to viscous torques. The second term in the left hand side of Eq. (3.14) represents the net flux of angular momentum J, which can be expressed as

$$J = \dot{M}\Omega R^2 - 3\pi\nu\Sigma\Omega R^2. \tag{3.15}$$

Assuming that the angular velocity remains Keplerian at the inner boundary ($R_{\rm in}$) of the disk the net flux of angular momentum at $R_{\rm in}$ can be given as

$$J = \dot{M}\Omega R^2 - \dot{M}\sqrt{GM_*R_{\rm in}}, \tag{3.16}$$

which leads to

$$3\pi\nu\Sigma = \dot{M}\left[1 - \left(\frac{R_{in}}{R}\right)^{\frac{1}{2}}\right]. \tag{3.17}$$

Note, however, that the angular velocity profile should flatten at the inner boundary due to the presence of a boundary layer[1], which results in vanishing Ω'.

As a consequence of the accretion, significant amount of gravitational potential energy has to be dissipated by viscous forces. The net torque exerted on an annulus with radial extent ΔR can be given by Eq. (3.9) as

$$J\left(R - \frac{\Delta R}{2}\right) - J\left(R + \frac{\Delta R}{2}\right) = -\frac{\partial J}{\partial R}\Delta R. \tag{3.18}$$

Thus, the power produced by this torque in an infinitesimally thin ring of ΔR is

$$-\frac{\partial J}{\partial R}\Omega = -\left[\frac{\partial}{\partial R}(J\Omega) - J\frac{\partial\Omega}{\partial R}\right]. \tag{3.19}$$

The annulus looses energy in two ways: 1.) via the gradient of $J\Omega$, which is related to the transport of energy due to viscosity, which vanishes when integrating over the disk surface, except for the energy transported out at the disk boundaries; 2.) via the second term representing the dissipation of energy due to viscosity. Thus, the power dissipated by the disk per unit area is

$$D(R) = -\frac{1}{2\pi R}J\frac{\partial\Omega}{\partial R} = \nu\Sigma\left(R\frac{\partial\Omega}{\partial R}\right)^2. \tag{3.20}$$

---

[1]The boundary layer is a transitional layer between the protoplanetary disk and the accreting star.

Far from the disk inner boundary, the angular velocity is surely Keplerian (possible flattening of Ω due to the presence of boundary layer is negligible), thus, using Eq. (3.17), the viscosity generates dissipation is

$$D(R) = \frac{3GM_*\dot{M}}{8\pi R^3} \left[1 - \left(\frac{R_{\text{in}}}{R} \right)^{1/2} \right].$$

(3.21)

If the disk radiates the viscous heat as a black body, i.e., the disk is optically thick to its radiation, the temperature distribution caused by viscous heating can be given by

$$T_{\text{visc}} = \left(\frac{3GM_*\dot{M}}{8\pi\sigma} \right)^{1/4} R^{-3/4} \left[1 - \left(\frac{R_{\text{in}}}{R} \right)^{1/2} \right]^{1/4},$$

(3.22)

where σ is the Stefan-Boltzmann constant. As a consequence, the viscous temperature distribution asymptotically $(R \gg R_{\text{in}})$ tends to be

$$T_{\text{visc}} \simeq \left(\frac{3GM_*\dot{M}}{8\pi\sigma} \right)^{1/4} R^{-3/4}.$$

(3.23)

As one can see, the energy released by the accretion is independent of the viscosity ν for steady state mass accretion rate. Integration of the dissipation energy over the radial distance R yields the total energy released by the accretion, which is

$$L_{\text{acc}} = \frac{1}{2} \frac{GM_*\dot{M}}{R_*}.$$

(3.24)

Note that, since the extent of boundary layer is relatively small (if it exists at all), comparing to the stellar radius, one can say that $R_{\text{in}} \simeq R_*$.

3.4   The α viscosity prescription

Although the viscous heating described by Eq. (3.22) is independent of the magnitude of viscosity, the fluid motion depends on the shear viscosity ν (see the last term of Eq. (3.2)). Therefore, it is clear that to model the evolution of a protoplanetary disk, one should know the value of ν. The viscous evolution of a protoplanetary disk in steady state approximation governing by Eq. (3.12) takes place on the time-scale of $t_\nu \sim R^2/\nu$. In the simplest case, the kinematic viscosity ν can be expressed as the product of typical random velocity of molecules (being in the order of the

local sound speed) c_s and the collisional mean free path λ, i.e., $\nu = c_s\lambda$. Assuming canonical disk properties (disk mass $\simeq 0.005\,M_\odot$, disk size $R \simeq 50\,\mathrm{AU}$, and aspect ratio $H/R \simeq 0.1$), one can find that the viscous time-scale is 10^{11} times that of the dynamical time-scale ($t_{\mathrm{dyn}} \sim 0.1 \times 10^3\mathrm{yr}$) of the disk. Thus, based on the fact that the average lifetime of protoplanetary disks is of the order of $10 \times 10^6\mathrm{yr}$, another phenomenon than bulk viscosity must act to power the disk accretion.

Since the Reynolds number of the fluid $Re = t_\nu/t_{\mathrm{dyn}}$ is considerably large, the protoplanetary disk is subject to development of turbulent motions. In this case, the resulting viscosity could be much higher due to the high loss of angular momentum. It can be shown that the stress provided by turbulent motions plays exactly the same role as a viscous stress in Eq. (3.2). Regarding the energy dissipation mechanism, it is however questionable whether this effective viscosity acts exactly as bulk viscosity. In a seminal paper Shakura & Sunyaev (1973) introduced a useful parametrization of the disk viscosity. Since the stress tensor τ in Eq. (3.4) has the physical dimension of density times the square of the velocity, the simplest assumption is that $\tau \sim \Sigma c_s^2$. In another way of expressing the α-prescription is to assume that the kinematic viscosity is $\nu \sim v_{\mathrm{turb}}l$, where v_{turb} is the average turbulent velocity of gas, and l is the characteristic size of turbulent cells. It is reasonable to assume that the characteristic scale of turbulent motions is smaller than the disk scale height H. Moreover, the velocity of turbulent motions should be smaller than the local sound speed c_s, otherwise it would be dissipated through shocks. Thus, the kinematic viscosity can be approximated as

$$\nu \simeq \alpha c_s H. \tag{3.25}$$

Due to the upper limit of the velocity of turbulence being the sound speed, the α parameter should be less than unity. Note, however, that there is certainly no cogent reason for believing $\alpha \leq 1$ throughout the disk, these assumption might be violated in small regions of the disk where some physical input continually feeds the supersonic turbulence (Frank et al. 2002). For example, Najita et al. (2003) suggested that supersonic turbulence may cause strong distortion of the molecular line profiles emitted by the disk: the double-peaked Kepler profile, as an indication of Keplerian rotation, could be smeared out producing single peaked line profiles.

We emphasize that the α-prescription is not an exact description of the viscosity, rather just a simple parametrization of viscous processes based on dimensional analysis. Thus, the value of α can only be constrained by observations. For example, the inferred viscous time-scale of the disks evolution suggests that $\alpha \simeq 0.01$ (Hartmann 1998).

Since the Reynolds number is expected to be high ($Re \gg 1$), the disks are highly turbulent.

3. Accretion process in disks

Although there are estimations for α, the physics that produce turbulence is still a matter of debate. The mechanism that causes turbulence should be suitable to extract energy from the rotational motion and keep turbulence active.

Based on the well-known Rayleigh criterion for stability, the epicyclic frequency (which is a complex number by definition) defined as

$$\kappa^2 = \frac{2\Omega}{R}\frac{d(\Omega R^2)}{dR},$$
(3.26)

should be $\kappa^2 < 0$ for instability. Since in protoplanetary disks $\Omega R^2 \sim R^{1/2}$, purely hydrodynamical disks are linearly stable. Note, however, that linearly stable disks might not be stable non-linearly. For example, Mukhopadhyay (2008) found that purely hydrodynamic disks are non-linearly turbulent, causing $\alpha \simeq 0.01$ turbulent viscosity. Moreover, Johnson & Gammie (2005) found a possible mechanism for angular momentum transport in low-ionization disks, with two important caveats: a mechanism must be found to inject vorticity into the disk, and the vortices must not decay rapidly due to three-dimensional instabilities.

The most accepted mechanism to generate turbulent viscosity producing outward angular momentum transport is the magneto-rotational instability (MRI), first numerically confirmed by Balbus & Hawley (1991); Hawley et al. (1995). In short, the MRI mechanism can be described by the following phenomena. As the magnetic field lines are coupled to the fluid motions, the field lines are carried along by the flow. The distance of two radially displaced disk elements is increasing with time due to the differential rotation of fluid ($d\Omega/dR < 0$). The magnetic tension generated by this displacement removes and gives angular momentum to the fluid elements orbiting closer and farther to the central object, respectively. As a result, a runaway process arises, whose net effect is an outward angular momentum transport, i.e., the appearance of turbulent viscosity.

4. DOUBLE-LAYER DISK MODEL

In the thermal disk model used in this work, the double-layer flaring disk approximation of Chiang & Goldreich (1997) is assumed. In this approximation, the protoplanetary disk is heated by the stellar irradiation and accretion processes. The incident stellar flux heats the disk atmosphere, which reprocesses the stellar light and irradiates the disk interior. The accretion processes heat the disk interior directly. In this way an optically thick disk interior and an optically thin disk atmosphere can be distinguished. The main characteristics of this double-layered approximation is given in Sect. 4.1. The optical depth of the atmospheric CO that determines the disk emission spectra is described in Sect. 4.2. The temperature profiles in the disk atmosphere and interior developed in the radiative equilibrium disk is presented in Sect. 4.3. In an unperturbed protoplanetary disk the orbits of the gas parcels are circular. For this case, the shape of the line profiles emitted by the disk is determined by the apparent inclination angle described in Sect 4.4. The motion of gas parcels is perturbed by stellar companions or embedded planets, as a result the orbit of gas parcels are no longer circular Keplerian, rather eccentric. Section 4.5 describes the main effect of the disk eccentricity on the line profile shape.

4.1 Double-layered disk

In the simplest scenario, the disk is modeled as a geometrically flat blackbody emitter, it lacks intrinsic luminosity and passively reradiates the energy absorbed from the central star. In this model, the infrared excess in the Spectral Energy Distribution (SED) is produced by the reprocessed radiation of small dust grains in the superheated optically thin surface layer of the disk, in addition to the emission of cooler layer of the disk interior. Interestingly, an opaque and geometrically thin disk heated by solely the steady state accretion processes results in the same SED (Lynden-Bell & Pringle 1974). Thus, the SEDs of passively irradiated and accretionally active disks have the same spectral index $n = 4/3$, representing the wavelength dependence of the disk luminosity $\nu L_\nu \nu^n$ (Adams et al. 1987). In contrast to these standard models, most sources exhibit flattish spectra

4. Double-layer disk model

in the range of $3\,\mu\text{m} \leq \lambda \leq 100\,\mu\text{m}$, having $0 \leq n \leq 3/4$ (see, e.g., Beckwith et al. (1990) and references therein). Kenyon & Hartmann (1987) proposed a solution to this problem: they investigated blackbody disk whose surface (also called as disk atmosphere) flares outward with increasing radius as a consequence of vertical hydrostatic equilibrium. Flared disk intercepts more stellar radiation than flat ones, therefore the spectral index increased. Graphical representations of flat and flared disks are shown in Fig. 4.1. Other models invoke additional heating of the disk or tenuous dusty envelope surrounds the system either scatters stellar radiation back onto the disk or absorbs and reemits it in the infrared (Natta 1993; Calvet et al. 1994).

In the interior and the atmospheric layers of the disk, the gas is thermalized by collisions with the dust grains. In the double-layered disk model, the interior layer is optically thick to the visual and infrared radiation too, while the atmosphere is optically thin to the infrared radiation. The boundary between the two layers lies at visual optical depth of $\tau_V = 1$. Taking into account the solution to the radiative transfer problem given by Eq. (2.13), the intensity of the radiation from the top of interior layer (where $\tau_\nu = \kappa_\nu \Sigma \gg 1$ and Σ is the surface mass density of the disk interior) at frequency ν is

$$I_\nu = B_\nu(T_\mathrm{i}), \tag{4.1}$$

where T_i is the temperature of interior layer. Applying again Eq. (2.13) for the disk atmosphere (where $\tau_\nu = \kappa_\nu \Sigma \leq 1$ and Σ is the surface mass density of the disk atmosphere), the intensity of the radiation at frequency ν is

$$I_\nu = B_\nu(T_\mathrm{i})e^{-\tau_\nu} + B_\nu(T_\mathrm{a})(1 - e^{-\tau_\nu}), \tag{4.2}$$

where T_a is the temperature at the surface layer. Here it is assumed that the intensity at the bottom of the disk atmosphere is equal to the continuum emission of the disk interior, $I_\nu(0) = B_\nu(T_\mathrm{i})$.

In a more elaborated model, one must consider that the dust and gas components of the disk may not be in thermal equilibrium at the disk atmospheric layer due to the lack of strong dust-gas coupling. If a mechanism heats the dust and gas with different efficiency[1], their temperatures may differ. For this case, one should involve two sources in the second term of Eq. (4.2): the emission of dust (with temperature T_d, density ρ_d, and mass absorption coefficient $\chi_{\mathrm{d}\nu}$), and the emission of gas (with temperature T_g, density ρ_g, and mass absorption coefficient $\chi_{\mathrm{g}\nu}$). While the total absorption coefficient of the medium is

$$\kappa_\nu = \rho_\mathrm{d}\chi_{\mathrm{d}\nu} + \rho_\mathrm{g}\chi_{\mathrm{g}\nu}, \tag{4.3}$$

---

[1] In some cases, the gas is superheated above the dust temperature by UV or X radiation of the young central star.
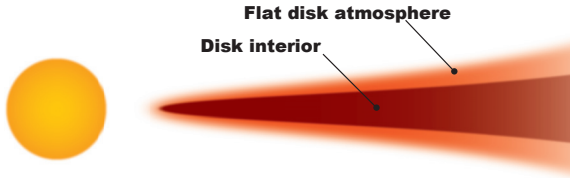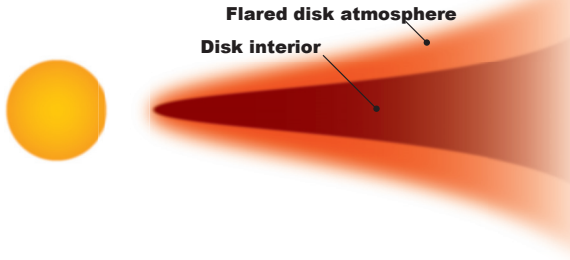
FIGURE 4.1: Graphical representations of flat (*top panel*) and flared (*lower panel*) disk models. For the flat disk model, the disk aspect ratio (H/R, where H is the disk height) is constant, while for the flared disk model, $H/R \sim R^\gamma$, where γ is the so-called flaring index.

and the emission is

$$j_\nu = \rho_d \chi_{d\nu} B(T_d) + \rho_g \chi_{g\nu} B(T_g). \tag{4.4}$$

Consequently, the source function introduced in Eq. (2.8) becomes

$$S_\nu = \frac{\rho_d \chi_{d\nu} B_\nu(T_d) + \rho_g \chi_{g\nu} B_\nu(T_g)}{\rho_d \chi_{d\nu} + \rho_g \chi_{g\nu}}. \tag{4.5}$$

Considering these equations in a double-layer model and taking into account the decoupling of dust and gas temperatures, the emission intensity of the radiation given by Eq. (4.2) becomes

$$I_\nu = B_\nu(T_i) e^{-\tau_\nu} + \frac{\rho_d \chi_{d\nu} B_\nu(T_d) + \rho_g \chi_{g\nu} B_\nu(T_g)}{\rho_d \chi_{d\nu} + \rho_g \chi_{g\nu}} \left(1 - e^{-\tau_\nu}\right), \tag{4.6}$$

where the optical depth of medium is $\tau_\nu = D(\rho_d \chi_{d\nu} + \rho_g \chi_{g\nu})$.

According to the first studies on surface gas temperatures by Jonkheid et al. (2004) and Kamp & Dullemond (2004), the gas temperature can be superheated several times of dust temperatures. If the mass contribution of the hydrogen becomes larger than 1%, H_2 line cooling becomes important, and the molecular line emission cools the gas down to below 100 K. The results of detailed gas models differs for the various molecular lines: while O[I] and C[II] line profiles strongly affected by superheated gas, the CO emission profiles less affected as the CO forms deeper in the disk.

4.2 Optical depth in the disk atmosphere

The atmospheric optical depth at the near-infrared wavelengths (τ_ν) which is required to calculate the disk emission given by Eq. (4.2) is the sum of optical depths of dust and gas in the disk atmosphere, i.e.

$$\tau_\nu = \kappa_{\nu_{ds}} D\rho_{ds} + \kappa_{\nu_{gs}} D\rho = \kappa_{\nu_{ds}} \Sigma_{ds} + \kappa_{\nu_{gs}} \Sigma_{gs}, \tag{4.7}$$

where $\kappa_{\nu_{ds}}$, $\kappa_{\nu_{gs}}$ are the mass absorption coefficients of dust and gas, Σ_{ds} and Σ_{gs} are the dust and gas surface density in the disk atmosphere. By definition the optical depth at the bottom of the disk atmosphere is unity, therefore the total surface density in the disk atmosphere is
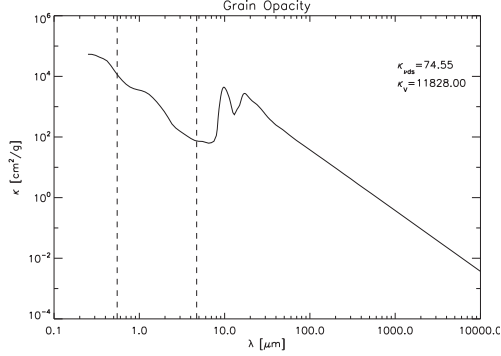
$$\Sigma_s = \frac{\delta}{\kappa_V}, \tag{4.8}$$

FIGURE 4.2: Dust opacity against the wavelength. The dust grain size is assumed to be $0.1\,\mu$m, composite of equal amount of Fe and Mg, and the grain density is assumed to be $2\,\mathrm{g\,cm^{-3}}$.

where δ is the grazing angle of the stellar irradiation measured at the top of the disk atmosphere, and κ_V is the overall opacity of dust in the disk atmosphere at visual wavelengths. The atmospheric dust and gas surface densities are

$$\Sigma_\mathrm{ds} \simeq X_\mathrm{ds}\Sigma_\mathrm{s}, \ \ \Sigma_\mathrm{gs} \simeq X_\mathrm{gs}\Sigma_\mathrm{s}, \tag{4.9}$$

where X_ds and X_gs are the dust and gas mass ratios to the H_2, respectively. Thus, the monochromatic optical depth at frequency ν can be given as

$$\tau_\nu \simeq X_\mathrm{ds}\delta\frac{\kappa_\mathrm{ds}}{\kappa_\mathrm{V}} + X_\mathrm{gs}\delta\frac{\kappa_{\nu_\mathrm{gs}}}{\kappa_\mathrm{V}}. \tag{4.10}$$

As one can see, the amount of overall opacity at visual wavelengths κ_V should be known to determine the surface density at the disk atmosphere. The dust opacity against the line lengths is shown in Fig. 4.2, assuming pure astronomical silicate dust with 50% Mg and 50% Fe composition, with grain size of 0.1μm, density of $2\,\mathrm{g\,cm^{-3}}$ (Weingartner & Draine 2001). For this dust model,

31

the dust opacity at visual wavelengths ($\lambda \simeq 0.55 \, \mu$m) is

$$\kappa_V \simeq 11828 \, \frac{\text{cm}^2}{\text{g}}, \tag{4.11}$$

while at the wavelengths of the ro-vibrational transitions of CO molecule ($\lambda \simeq 4.7 \, \mu$m) is

$$\kappa_{ds} \simeq 74.55 \, \frac{\text{cm}^2}{\text{g}} \tag{4.12}$$

As a matter of fact, the dust consists of different size grains (Mathis et al. 1977), for which case the mass absorption coefficient can be given by

$$\kappa_{\nu_{ds}} = \frac{\pi}{\Sigma} \int_{r_{\min}}^{r_{\max}} \mathbf{f}(r) r^2 \epsilon_\nu dr, \tag{4.13}$$

where the size distribution of dust grains with radius r is

$$\mathbf{f}(r) = r^{-q}. \tag{4.14}$$

Using the standard value of $q = 3.5$ places the most of the geometric surface area in the smallest grains and most of the mass in the largest grains. Note that, the largest grain size is smaller in the disk atmosphere than in the interior, because the larger grains tend to settle into the disk mid plane.

In summary, collecting Eqs. (2.26), (2.33), and (2.34) the optical depth of the disk atmosphere according to Eq. (4.10) can be determined. To calculate the CO line profiles emitted by the disk according to Eq. (4.2), the disk radial temperature profile, determining the population levels of the emitting molecules according to Eq. (2.26) and the grazing angle of the stellar irradiation δ determining the atmospheric optical depth according to Eq. (4.10) must be known, which are described in the next section.

4.3 Disk temperature profiles

In the simplest approximation, the stellar radiation can be described by a blackbody radiation at temperature T_*, thus, the flux radiated by the star is

$$F_* = \sigma T_*^4, \tag{4.15}$$

where T_* is the temperature of stellar photosphere and σ is the Stefan–Boltzmann constant. For this case, the flux of stellar irradiation incident upon the disk at a distance R is

$$F(R) = \frac{\delta}{2} \left(\frac{R_*}{R} \right)^2 \sigma T_*^4,$$ (4.16)

where δ is the grazing angle of the radiation that strikes the disk at distance R (see, e.g., Fig. 4.3). Supposing that the disk is in local thermodynamical equilibrium – namely the emitted and absorbed energy by a given disk element equilibrates – everywhere, the effective temperature of the disk at a distance R is

$$T_e(R) \simeq \left(\frac{\delta}{2} \right)^{\frac{1}{4}} \left(\frac{R_*}{R} \right)^{\frac{1}{2}} T_*.$$ (4.17)

4.3.1   Radiative equilibrium disk

According to the double-layer disk model of Chiang & Goldreich (1997), the disk can be described by two layers: a cooler interior and a hotter atmosphere. In the optically thin atmospheric layer, the dust grains are exposed to the light in the visual wavelengths emitted from the central star, whose radiation energy is reprocessed by the dust and reemitted in the infrared wavelengths. The inner region of the disk is optically thick, and irradiated from the atmosphere.

At the atmosphere, the radiation coming from the central star strikes the surface at grazing angle δ and is absorbed within visible optical depth of unity ($\tau_V = 1$). The optical depth normal to the disk plane caused by the superheated atmospheric dust at visual wavelengths ν_V is

$$\tau_{a\perp}(\nu_V) = \sin(\delta \tau_a(\nu_V)) \simeq \delta \tau_a(\nu_V) \simeq \delta,$$ (4.18)

assuming that the disk is geometrically thin. The optical depth normal to the disk plane caused by the superheated atmospheric dust at infrared wavelengths ν_{ir} is

$$\tau_{a\perp}(\nu_{ir}) = \epsilon_a \tau_{a\perp}(\nu_V) \simeq \delta \epsilon_a,$$ (4.19)

where ϵ_a is the dust emissivity, i.e, the ratio of Planck mean opacities measured at T_* and T_a. The disk atmosphere is opaque to the infrared radiation, i.e., it is optically thin at infrared wavelength ($\tau_{a\perp}(\nu_{ir}) \ll 1$). Thus, according to the analytical solution of the radiation transfer equation given by Eq. (2.13), the infrared intensity emitted by the disk atmosphere is

$$I(\nu_{ir}) = B(T_a) \left(1 - e^{-\tau_{a\perp}(\nu_{ir})} \right) \simeq B(T_a) \delta \epsilon_a,$$ (4.20)

33

4. Double-layer disk model

and the radiation flux is

$$F_{\mathrm{a}}(R) = \int \nu B(T_{\mathrm{a}}) \delta\epsilon_{\mathrm{a}} d\nu = \sigma T_{\mathrm{a}}^4 \delta\epsilon_{\mathrm{ds}}. \tag{4.21}$$

Since the disk is assumed to be in local thermodynamic equilibrium, and the stellar hemispheres that seen by the dust elements is one half of the total stellar surface[2], the reradiated and irradiated flux of dust atmospheres are equal, $F_{\mathrm{a}}(R) = (1/2)F_*(R)$. Equating half of the flux incident from the star given by Eq. (4.16) and emitted by the atmospheric dust given by Eq. (4.21), the disk atmosphere is superheated to the temperature

$$T_{\mathrm{a}}(R) \simeq \left(\frac{1}{4\epsilon_{\mathrm{a}}}\right)^{\frac{1}{4}} \left(\frac{R_*}{R}\right)^{\frac{1}{2}} T_*. \tag{4.22}$$

Now we have to determine the emissivity of the atmospheric dust ϵ_{a} heated to temperature of T_{a}. Let us use the definition of emissivity given by Dullemond et al. (2001), which is

$$\epsilon_{\mathrm{a}} = \frac{\kappa_{\mathrm{P}}(T_{\mathrm{a}})}{\kappa_{\mathrm{P}}(T_*)}. \tag{4.23}$$

The mean Planck opacity at temperature T can be defined as

$$\kappa_{\mathrm{P}}(T) = \frac{\int_0^\infty B_\nu(T)\kappa_\nu d\nu}{\int_0^\infty B_\nu(T)d\nu}. \tag{4.24}$$

Assuming that the dust opacity is proportional to the wavelength as $\kappa_{\mathrm{a}}(\lambda) \sim \lambda^{-\beta}$, where $\beta > 0$ (seen Fig. 4.2), and using small temperature approximation to the near infrared blackbody emission

$$B_\lambda(T) \simeq \frac{2hc^2}{\lambda^5} \frac{1}{e^{\frac{hc}{\lambda k T}}}, \tag{4.25}$$

Eq. (4.23) can explicitly be given as

$$\epsilon_{\mathrm{a}} \simeq \left(\frac{T_*}{T_{\mathrm{a}}}\right)^{\beta}. \tag{4.26}$$

With this result, the atmospheric dust temperature is

$$\boxed{T_{\mathrm{a}}(R) \simeq \left(\frac{1}{4}\right)^{\frac{1}{4+\beta}} \left(\frac{R_*}{R}\right)^{\frac{2}{4+\beta}} T_*.} \tag{4.27}$$

---

[2]The disk has two atmospheric layers, see Fig. 4.1 for an example.

It is important to note that the dust temperature distribution in disk atmosphere determined by Eq. (4.27) is independent of the grazing angle δ of the incident stellar irradiation.

Now let us estimate the disk interior temperature. Because of the plane-parallel symmetry of the disk, about half of the reprocessed atmospheric radiation will be radiated away, and only the other half will heat the disk interior. Only a fraction (i.e., $1 - e^{-\tau_i(\nu_{ir})}$ part of the irradiation, where $\tau_i(\nu_{ir})$ is the optical depth of interior layer at the infrared wavelength) of the radiation emitted by the atmospheric layer is absorbed by the disk interior (Dullemond et al. 2001). In local thermodynamic equilibrium, the absorbed energy equates to the half of the atmospheric emission:

$$(1 - e^{-\tau_i(T_i)})\sigma T_i^4 = \frac{1}{2}(1 - e^{-\tau_i(T_a)})\sin\delta\sigma T_a^4,\tag{4.28}$$

therefore knowing the dust temperature of the disk atmosphere (T_a) given by Eq. (4.22), the interior layer is heated to the temperature

$$T_i(R) = \left(\frac{\delta}{4}\right)^{1/4}\left(\frac{1 - e^{-\tau_i(T_i)}}{1 - e^{-\tau_i(T_a)}}\right)^{\frac{1}{4}}\left(\frac{R_*}{R}\right)^{\frac{1}{2}}T_*,\tag{4.29}$$

due to the atmospheric irradiation. As can be seen, the disk interior can be separated into three distinct ranges. In the innermost region (r_1), the disk interior is optically thick both to its own and the atmospheric radiations, ($\tau_i(T_a) > 1$ and $\tau_i(T_i) > 1$), where the interior is heated to the temperature

$$T_{i_1}(R) \simeq \left(\frac{\delta}{4}\right)^{\frac{1}{4}}\left(\frac{R_*}{R}\right)^{\frac{1}{2}}T_*.\tag{4.30}$$

Beyond this region (r_2), the disk interior is optically thin to its own radiation ($\tau_i(T_i) = \kappa_i\Sigma = \epsilon_i\kappa_V\Sigma$), where

$$T_{i_2}(R) \simeq \left(\frac{\delta}{4}\right)^{\frac{1}{4}}\left(\frac{1}{\epsilon_i\kappa_V\Sigma}\right)^{\frac{1}{4}}\left(\frac{R_*}{R}\right)^{\frac{1}{2}}T_*.\tag{4.31}$$

In the outermost region of the disk (r_3), the interior is optically thin both to its own and the atmospheric radiations ($\tau_i(T_a) = \kappa_i\Sigma = \epsilon_a\kappa_V\Sigma$), which leads to interior temperature of

$$T_{i_3}(R) \simeq \left(\frac{\delta}{4}\right)^{\frac{1}{4}}\left(\frac{\epsilon_a}{\epsilon_i}\right)^{\frac{1}{4}}\left(\frac{R_*}{R}\right)^{\frac{1}{2}}T_*.\tag{4.32}$$

In Eqs. (4.31) and (4.32), ϵ_i is the dust emissivity in the disk interior, which can be given similarly to Eq. (5.24) as

$$\epsilon_i(R) = \left(\frac{T_i}{T_a}\right)^{\beta}.\tag{4.33}$$

With this, the explicit form of interior temperature in the region r_1 is

$$T_{i_2}(R) \simeq \left(\frac{\delta}{4}\right)^{\frac{1}{4+\beta}} \left(\frac{1}{4}\right)^{\frac{\beta}{(4+\beta)^2}} \left(\frac{1}{\kappa_V \Sigma}\right)^{\frac{1}{4+\beta}} \left(\frac{R_*}{R}\right)^{\frac{2+3\beta}{(4+\beta)^2}} T_*,$$

(4.34)

while in the outermost region r_3 is

$$T_{i_3}(R) \simeq \left(\frac{\delta}{4}\right)^{\frac{1}{4+\beta}} \left(\frac{R_*}{R}\right)^{\frac{2}{4+\beta}} T_*.$$

(4.35)

Note that the dust temperature distribution in the disk interior for all three regimes determined by Eq. (4.30), (4.34) and (4.35) are dependent on, while the atmospheric temperature given by Eq. (4.27) is independent of the grazing angle δ of the stellar irradiation impinged on the disk atmosphere.

4.3.2 Effect of disk geometry

As shown in the previous section, the grazing angle of the stellar irradiation affects the temperature distribution of disk interior, which is exclusively determined by the disk geometry, i.e., the height of the visible photosphere above the disk midplane H. In this section, I investigate two disk geometries: flat and hydrostatic equilibrium disk.

A disk with a constant opening angle ($H/R = h$, where h is constant) is called flat disk. In flat disk with small aspect ratio ($H/R \ll 1$), the grazing angle can be given as

$$\delta(R) = \frac{4}{3\pi} \frac{R_*}{R}.$$

(4.36)

Assuming that the disk is in vertical hydrostatic equilibrium, the grazing angle is

$$\delta(R) \simeq \frac{4}{3\pi} \frac{R_*}{R} + R \frac{d}{dR} \left(\frac{H}{R}\right),$$

(4.37)

according to Kenyon & Hartmann (1987). Calculating H/R according to Chiang & Goldreich (1997), one can get

$$\frac{H}{R} \simeq 4 \left(\frac{T_*}{T_c}\right)^{\frac{4}{7}} \left(\frac{R}{R_*}\right)^{\frac{2}{7}},$$

(4.38)

where T_c can be expressed as

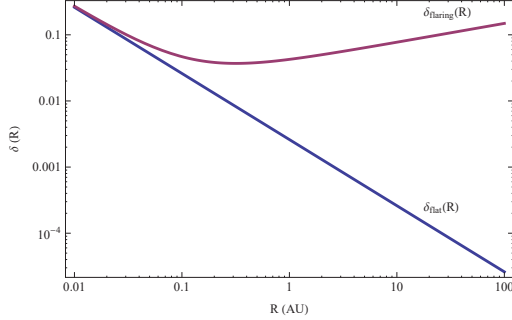$$T_c = \frac{G M_* \mu_g}{k R_*},$$

(4.39)

FIGURE 4.3: Grazing angle $\delta(R)$ as a function of the distance R to the central star for flat (*blue curve*) and hydrostatic equilibrium (*red curve*) disk geometries. As can be seen, $\delta(R)$ continuously decreases with R for flat disks, while begins to increase for hydrostatic equilibrium disk beyond a certain distance, i.e. the disk height is flared.

where μ_{g} is the mean molecular weight of the gas molecule in the disk[3] Using Eqs. (4.38) and (4.39), the grazing angle as a function of the radial distance for a disk in hydrostatic equilibrium can be given as

$$\delta(R) = \frac{4}{3\pi} \frac{R_*}{R} + \frac{8}{7} \left(\frac{T_*}{T_{\mathrm{c}}}\right)^{\frac{4}{7}} \left(\frac{R_*}{R}\right)^{-\frac{2}{7}}. \tag{4.40}$$

Figure 4.3 shows the grazing angle $\delta(R)$ for flat and hydrostatic equilibrium disks. In hydrostatic equilibrium disk, the grazing angle is higher than in flat disk at large distances, i.e., the disk height is flared. The grazing angle reaches its minimum value at a distance of

$$R_{\alpha_{\min}} = \left(\frac{1}{8}\right) \left(\frac{7}{2}\right)^2 \left(\frac{21}{2\pi}\right)^{\frac{7}{9}} \left(\frac{T_{\mathrm{c}}}{T_*}\right)^{\frac{4}{9}} R_*, \tag{4.41}$$

for flaring disks. Comparing the disk interior temperatures of flat and flaring geometry, shown in Fig. 4.4, one can see that the temperature distribution of flat disk is slightly steeper than in flaring

---

[3]The most abundant molecular component in the disk is the H_2 molecule, hence the mean molecular weight of the disk gas can be approximated by the mass of H_2 molecule.
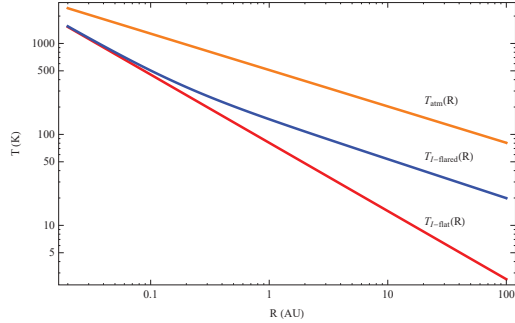
4. Double-layer disk model

FIGURE 4.4: Disk interior and atmospheric temperature profiles as a function of the distance R to the central star for flat and flaring disk geometries. The stellar parameters required for the calculations were: $T_* = 4000\,\mathrm{K}$, $R_* = 2.5R_\odot$, $M_* = 0.5\,M_\odot$.

disk. Using the Eqs. (4.30), (4.34), (4.35), and (6.8), the temperature distributions in the three regions of the disk interior are

$$
\begin{aligned}
T_{i_1}(R) &= \left(\frac{1}{3\pi}\right)^{\frac{1}{4}} \left(\frac{R_*}{R}\right)^{\frac{3}{4}} T_*, \\
T_{i_2}(R) &= \left(\frac{1}{3\pi}\right)^{\frac{1}{4}} \left(\frac{R_*}{R}\right)^{\frac{3}{4}} T_*, \\
T_{i_3}(R) &= \left(\frac{1}{3\pi}\right)^{\frac{1}{4+\beta}} \left(\frac{R_*}{R}\right)^{\frac{3}{4+\beta}} T_*
\end{aligned}
\tag{4.42}
$$

of flat disks, while

$$T_{i_1}(R) = \left(\frac{1}{3\pi}\right)^{\frac{1}{4}} \left(\frac{R_*}{R}\right)^{\frac{3}{4}} T_* \left[1 + 3\pi\frac{4}{7}\left(\frac{T_*}{T_c}\right)\left(\frac{R_*}{R}\right)^{-\frac{5}{7}}\right]^{\frac{1}{4}},$$

$$T_{i_2}(R) = \left(\frac{1}{3\pi}\right)^{\frac{1}{4}} \left(\frac{R_*}{R}\right)^{\frac{3}{4}} T_*,$$

$$T_{i_3}(R) = \left(\frac{1}{3\pi}\right)^{\frac{1}{4+\beta}} \left(\frac{R_*}{R}\right)^{\frac{3}{4+\beta}} T_* \times \left[1 + 3\pi\frac{4}{7}\left(\frac{T_*}{T_c}\right)\left(\frac{R_*}{R}\right)^{-\frac{5}{7}}\right]^{\frac{1}{4+\beta}}, \tag{4.43}$$

for flared disks.

4.4 Effect of disk inclination angle

If the disk plane is viewed by an angle[4] of $i > 0$, the Doppler shift $\Delta\nu$ of the intrinsic line profile emitted by a parcel of the disk atmosphere defined in Eq. (2.34) departs from zero. Assuming that the disk has a Keplerian rotation profile with line-of-sight velocity component of

$$v_\parallel = \cos(\theta)\sqrt{\frac{GM_*}{R}}, \tag{4.44}$$

the Doppler shift of the fundamental line centering at ν_0 emitted by an atmospheric disk parcel with azimuthal angle[5] θ at a distance R from the central star with mass M_* can be given as

$$\Delta\nu = \frac{\nu_0}{c}\sin(i)v_\parallel = \frac{\nu_0}{c}\sin(i)\cos(\theta)\sqrt{\frac{GM_*}{R}}. \tag{4.45}$$

The disk inclination affects the line-of-sight monochromatic optical depth of the disk atmosphere too. In Eq. (2.3), the thickness of the disk atmosphere D must be projected to the direction of the line-of-sight, which yields

$$\tau_\nu \simeq \kappa_\nu \frac{D}{\cos(i)}\rho = \kappa_\nu\Sigma_\nu\frac{1}{\cos(i)}. \tag{4.46}$$

Note that this method cannot be applied for large inclination angles, in which case the disk emission is self-absorbed by its own atmosphere, thus Eq. (4.46) gives a false result for edge on disks.

---

[4]The inclination angle definition is as follows: $i = 0$, if the disk is seen face on.

[5]The azimuthal angle θ is defined as: $\theta = 0$, where the velocity component of the Keplerian motion is maximal in receding.

4.5   Effect of disk eccentricity

If the orbits of gas parcels are not circular, i.e. the disk is eccentric, the Doppler shift caused by the line-of-sight velocity component of the rotation given by Eq. (4.44) is modified to

$$v_{\parallel} = (v_{\mathrm{x}} \sin(\theta_{\mathrm{p}}) + v_{\mathrm{y}} \cos(\theta_{\mathrm{p}})) \sin(i), \tag{4.47}$$

where θ_{p} is the elliptic orbit's perihelion angle measured from $\theta = 0$. In Eq. (4.47), the velocity components v_{x} and v_{y} of a given parcel of the disk on elliptical orbit are

$$v_{\mathrm{x}} = -\sin(\theta) \sqrt{\frac{GM_*}{r(1 + e\cos(\theta))}}, \tag{4.48}$$

$$v_{\mathrm{y}} = (\cos(\theta) + e) \sqrt{\frac{GM_*}{r(1 + e\cos(\theta))}}, \tag{4.49}$$

where e is the disk eccentricity. Thus, the Doppler shift of the fundamental line centering at ν_0 defined previously by Eq. 4.50 is modified to

$$\Delta\nu = \frac{\nu_0}{c} \left[-\sin(\theta)\sin(\theta_{\mathrm{p}}) + (\cos(\theta) + e)\cos(\theta_{\mathrm{p}}) \right] \sqrt{\frac{GM_*}{r(1 + e\cos(\theta))}} \sin(i) \tag{4.50}$$

for eccentric disks.

5. DETECTABILITY OF EMBEDDED PLANETS BY NEAR-IR CO SPECTRA

5.1 Abstract

Context: Planets are thought to form in protoplanetary accretion disks around young stars. Detecting a giant planet still embedded in a protoplanetary disk would be very important and give observational constraints on the planet-formation process. However, detecting these planets with the radial velocity technique is problematic owing to the strong stellar activity of these young objects.

Aims: We intend to provide an indirect method to detect Jovian planets by studying near infrared emission spectra originating in the protoplanetary disks around T Tauri stars. Our idea is to investigate whether a massive planet could induce any observable effect on the spectral lines emerging in the disks atmosphere. As a tracer molecule we propose CO, which is excited in the ro-vibrational fundamental band in the disk atmosphere to a distance of $\sim 2 - 3\,\mathrm{AU}$ (depending on the stellar mass) where terrestrial planets are thought to form.

Methods: We developed a semi-analytical model to calculate synthetic molecular spectral line profiles in a protoplanetary disk using a double-layer disk model heated on the outside by irradiation by the central star and in the midplane by viscous dissipation due to accretion. 2D gas dynamics were incorporated in the calculation of synthetic spectral lines. The motions of gas parcels were calculated by the publicly available hydrodynamical code FARGO which was developed to study planet-disk interactions.

Results: We demonstrate that a massive planet embedded in a protoplanetary disk strongly influences the originally circular Keplerian gas dynamics. The perturbed motion of the gas can be detected by comparing the CO line profiles in emission, which emerge from planet-bearing to those of planet-free disk models. The planet signal has two major characteristics: a permanent line profile asymmetry, and short timescale variability correlated with the orbital phase of the giant planet. We have found that the strength of the asymmetry depends on the physical parameters of the star-planet-disk system, such as the disk inclination angle, the planetary and stellar masses, the orbital distance, and the size of the disk inner cavity. The permanent line profile asymmetry is caused by a disk in an eccentric state in the gap opened by the giant planet. However, the variable component is a consequence of the local dynamical perturbation by the orbiting giant planet. We show that a forming giant planet, still embedded in the protoplanetary disk, can be detected using contemporary or future high-resolution near-IR spectrographs like VLT/CRIRES and ELT/METIS.

5.2 Introduction

According to the general consensus, planets and planetary systems form in circumstellar disks. These disks consist of gaseous and solid dust material. There are two major mechanisms proposed for the formation of giant planets. The first is the disk instability, which requires a gravitationally unstable disk in which giant planets form by direct collapse of the gas as a consequence of its self-gravity, originally suggested by Kuiper (1951); Cameron (1978) and more recently by Boss (2001). Later on, the gas giant may collect dust, which after settling to its center, forms a solid core. The second mechanism is the core-accretion process (Bodenheimer & Pollack 1986; Pollack et al. 1996), which is the final stage of planet formation in the planetesimal hypothesis (Safronov 1972). In this hypothesis dust coagulates first and forms planetesimals (meter to kilometer-sized objects). The subsequent growth of planetesimals consists of two stages, the runaway (Wetherill & Stewart 1989) and the oligarchic growth (Kokubo & Ida 1998), in which the formed bodies are massive enough to increase their masses by gravity-assisted collisional accretion processes. In this way planetary embryos and, through their consecutive collisions, protoplanets, terrestrial planets, and planetary cores of giant planets can be formed. During the gas accretion phase the precursor of the proto giant planet reaches a critical mass (where the planetary envelope contains more material than its core), and at about the order of $10\,M_{\oplus}$ starts to contract, causing an increased accretion rate, which in turn raises radiative energy losses resulting in a runaway gas accretion. In this

model the planetary core rapidly builds up a massive envelope of gas from its surrounding disk, in less than $10\,\mathrm{Myr}$, and eventually a gas giant forms. Because the disk dispersal time is presumably about $5\,\mathrm{Myr}$ (Haisch et al. 2001; Hillenbrand 2005), this model should also incorporate planetary migration to explain giant planets observed well inside the snow line, see Alibert et al. (2004).

Both planetary formation processes have their weak points. Disk instability assumes a very massive disk that is gravitationally unstable or only marginally stable. Another as yet unsolved problem is that during the gravitational collapse an effective cooling mechanism should work to ensure the formation of gravitationally bound clumps. While the radiative cooling is not effective enough and the recently invoked thermal convection is also ineffective, the disk instability as a common planet-formation process is questionable (Klahr 2008).

Regarding the giant planet formation in the planetesimal hypothesis, Mordasini et al. (2009) convincingly presented the success of the core accretion model to produce giant planets within the disk lifetime in a planet population synthesis model, but the artificial slow-down of the type I migration was necessary. Type I migration has such a short time scale (Ward 1997) that the planet inevitably will be engulfed by the host star within the disk lifetime. Another unsolved issue of the planetesimal hypothesis is the so-called "meter-sized barrier problem": i.e. the formation of meter-sized bodies is impeded by their quick inward drift to the star (Weidenschilling 1977), and by mutual disruptive collisions due to their high relative velocities above $1\,\mathrm{m/s}$ (Blum & Wurm 2008). If no other physical processes are taking place, these two mechanisms would impede the formation of the meter-sized and consequently the larger planetesimals.

A wealth of information about the planet formation process would clearly be provided if newly formed planets, or at least their signatures, could be observed in still gas-rich protoplanetary disks. There are already attempts to discover signatures of giant planet-formation assuming the disk instability mechanism in the works of Narayanan et al. (2006) and Jang-Condell & Boss (2007). In the first study, for instance, the authors suggest observations of HCO^+ emission lines as a tracer of the accumulation of large clumps of cold material, arguing that with high-resolution millimeter and sub-millimeter interferometers the cold clumps can be directly imaged. The observability of an already formed planet embedded in a circumstellar disk has also been studied recently by Wolf & D'Angelo (2005) and Wolf et al. (2007). In these works the authors investigated whether the influence of a forming planet on the protoplanetary disk can be detected by analyzing the spectral energy distribution (SED) coming from the star-disk system. It was found that by studying only the SED it is impossible to infer the presence of an embedded planet. On the other hand, it was also concluded that the dust re-emission in the hot regions near the gap could certainly be detected

and mapped by ALMA for the nearby (less than $100\,\mathrm{pc}$ in distance) and approximately face-on protoplanetary disks.

Another interesting attempt was presented by Clarke & Armitage (2003), where the authors have investigated the possibility of detection of giant planets by excess CO overtone emission originating from the planetary accretion inflow in FU Ori type objects. Nevertheless, the periodic line profile distortions are observable only in tight systems in which the giant planet is orbiting within $0.25\,\mathrm{AU}$. Another possibility to detect embedded giant planets is based on the radial velocity measurements, which favor high-mass, short-period companions. The detectability limit of an embedded giant planet by radial velocity measurements is $\sim 10\,M_\mathrm{J}$ or $\sim 2\,M_\mathrm{J}$ (M_J is the mass of Jupiter) orbiting at 1 AU or 0.5 AU, respectively, due to heavy variability in the optical spectra of young ($< 10\,\mathrm{Myr}$) stars (e.g., Paulson & Yelda (2006); Prato et al. (2008)). Note that although there were attempts to detect planets by radial velocity measurements in young systems, no firm detection has yet been repeated see, e.g., Setiawan et al. (2008) for TW Hya b, debated later by Huélamo et al. (2008). The discovery of planetary systems by direct imaging nowadays is restricted to large separations $> 10 - 100\,\mathrm{AU}$ (Veras et al. 2009) and favors higher mass planets. As of today nine exoplanetary systems have been directly imaged in the optical or near-infrared band, but only five of them are still embedded: GQ Lup (Neuhäuser et al. 2005) and CT Cha (Schmidt et al. 2008), but they are rather hosting a stellar companion as the companion masses are, because high as $21.5\,M_\mathrm{J}$ and $17\,M_\mathrm{J}$, respectively; 2M1207 (Chauvin et al. 2004, 2005a) hosting a $4\,M_\mathrm{J}$ mass planet; UScoCTIO 108 (Kashyap et al. 2008) hosting a $14\,M_\mathrm{J}$ mass planet; β Pic (Lagrange et al. 2009a,b) hosting an $8\,M_\mathrm{J}$ mass planet. AB Pic (Chauvin et al. 2005b), HR 8799 (Marois et al. 2008) (triple system), SR 1845 (Biller et al. 2006) and Fomalhaut (Kalas et al. 2008) are mature planetary systems with ages of about 30 Myr, 60 Myr, 100 Myr, and 200 Myr. Note that centimeter wavelength radio observations of a very young ($< 0.1\,\mathrm{Myr}$) disk around HL Tau, presented by Greaves et al. (2008), revealed the possibility of a 12 Jupiter mass giant planet being in formation at $\sim 75\,\mathrm{AU}$.

We investigate a new possibility to detect young giant planets embedded in protoplanetary disks of T Tauri stars via line profile distortions in its near-IR spectra. Contrary to the studies mentioned above, instead of dealing with the disk's density perturbations, we investigate the gas *dynamics* in the disk, particularly near the gap opened by the planet. We have found that there is a reasonable possibility to discover giant planets embedded in the protoplanetary disk of young stars with our approach.

Our idea has been inspired by recent findings of Kley & Dirksen (2006), who showed that

a massive giant planet embedded in a protoplanetary disk produces a transition of the disk from the nearly circular state into an eccentric state. The mass limit for this transition is $3\,M_J$ for a disk with $\nu = 10^{-5}$ uniform kinematic viscosity (measured in dimensionless units, see details in Sect. 5.4.1). The most visible manifestation of the disk's eccentric state is that the outer rim of the gap opened by the giant planet has an elliptic shape. After performing a series of hydrodynamical simulations with the code FARGO (Masset 2000), we can also confirm the results of Kley & Dirksen (2006) even using α-type viscosity. Note that beside the elliptic geometry that is clearly visible in the disk surface-density distribution, the giant planet also disturbs the motion of the gas parcels near the gap. Using CO as tracer molecule of gas, which is excited to $\sim 3 - 5\,\mathrm{AU}$ (depending on the stellar mass) in the disk atmosphere (Najita et al. 2007), we investigate how the CO emission line profiles at $4.7\,\mu\mathrm{m}$ are distorted by the gas dynamics. With our semi-analytical synthetic spectral model we explore the influence of the mass of the giant planet, the disk inclination angle, the mass of the hosting star, the orbital distance of planet, and finally, the size of inner cavity on the line profile distortions.

The Chapter is structured as follows: in Sect. 5.3 we review the basic physics of our synthetic spectral line models. In Sect. 5.4 we present disk models and details of numerical simulations. Our results of the CO ro-vibrational line profile distortions, the detectability of an embedded giant planet, and its observability constraints are presented in Sect. 5.5. This Chapter closes with the discussion of the results and concluding remarks.

5.3   Synthetic spectral line model

To calculate the CO ro-vibrational spectra emerging from protoplanetary disks we developed a semi-analytical line spectral model. The thermodynamical model of the disk is based on the two-layer flared disk model, originally proposed by Chiang & Goldreich (1997), which describes the heating by stellar irradiation in a disk with a flared geometry. In our model we use the flared disk approximation, and assume the disk to consist of two layers: an optically thick interior, producing continuum radiation and an optically thin atmosphere, producing line emission or absorption in the spectra.[1] The boundary between the two layers lies where the dust becomes optically thick in

---

[1]We only consider the inner part of disk ($R \leq 5\,\mathrm{AU}$). A significant part of the fundamental band CO ro-vibrational emission arises in $R = 2 - 3\,\mathrm{AU}$, however the line-to-continuum flux at $4.7\,\mu m$ is sensitive to material that lies up to $5\,\mathrm{AU}$ in our models. In this way the outer part of disk, where the disk interior becomes optically thin to its own and even to the radiation from superheated atmosphere, is not considered.
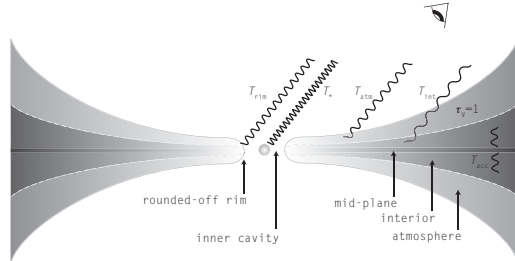
FIGURE 5.1: Double-layer flared disk model used in our simulations, after Chiang & Goldreich (1997). In our model the following emission components are included: the optically thin atmosphere emission, with a temperature T_{atm} above the optically thick disk interior, with the temperature T_{int}; the continuum emission of the rounded-off disk inner rim, with a temperature T_{rim} and the stellar continuum assumed to be a blackbody with a temperature T_*. The accretion heating of disk interior is also accounted for.

the visual wavelengths, i.e. at optical depth $\tau_{\mathrm{V}} = 1$ along the line of the incident stellar irradiation. The irradiation from the boundary layer formed at the inner edge of the disk (Popham et al. 1993) is neglected though because its existence had not yet been confirmed conclusively by observations yet. Nevertheless, the emission from the inner disk rim is substantial, resulting in strong near-IR bump in Herbig Ae/Be (Natta et al. 2001) and weaker one in T Tauri SEDs (Muzerolle et al. 2003). In addition it was found by Monnier et al. (2006) that the simple vertical wall assumption for the inner rim is inconsistent with the interferometric measurements. Indeed, the shape of the disk inner rim is presumably rounded-off, resulting in less inclination-angle-dependent near-IR excess emission (Isella & Natta 2005). A schematic representation of the disk model is shown in Fig.5.1. If the disk atmosphere is superheated by the stellar irradiation with respect to its interior, we may expect emission lines. Conversely, if the disk interior is heated above the temperature of the disk atmosphere by viscous dissipation, for example due to an abrupt increase in accretion rate, spectral lines are expected in absorption.

The vertical structure of a geometrically thin disk can be derived by considering vertical hydrostatic equilibrium (Shakura & Sunyaev 1973). Ignoring any contribution from the gravitational

force of the disk itself, the vertical density profile would be set by the equilibrium of gas pressure, the stellar gravitation and centrifugal force owing to orbital motion, resulting in a Gaussian vertical density profile. Because the thickness of the disk atmosphere in the double-layer model is principally determined by the grazing angle of the stellar irradiation, which is narrow ($\delta(R) \ll 1$) in our computational domain ($R \leq 5\,\mathrm{AU}$), we assume that the disk atmosphere has uniform vertical density distribution. Note that the surface density in the disk atmosphere according to Eq. (5.31) does not depend on the surface density ($\Sigma(R)$) distribution by definition.

The expected flux emerging from the double-layer disk is the result of the radiation of gas emission from the optically thin disk atmosphere above the continuum emission of dust in the optically thick disk interior and inner rim. Because the stellar continuum contributes considerably to the line flux in the near-IR band compared to the disk continuum, especially in disks with an inner cavity, we have to also take into account the stellar continuum in the total flux. In our model the stellar radiation is taken to be blackbody radiation of the stellar effective surface temperature. Because the gas temperature is regulated by collisions with dust grains and stellar X-ray heating (which is significant for a young star), the gas and dust components may be thermally uncoupled in the tenuous disk atmosphere below a critical density of $n_{\mathrm{cr}} \sim 10^{13} - 10^{14}\,\mathrm{cm}^{-3}$ (Chiang & Goldreich 1997). As a result the gas temperature can be as high as $\sim 4000 - 5000\,\mathrm{K}$ in a region where the column density is below $\sim 10^{21}\,\mathrm{cm}^{-2}$ (Glassgold et al. 2004). Because the gas column density is $\sim 10^{22}\,\mathrm{cm}^{-2}$ in our model disk atmosphere, we adopt thermal coupling of dust and gas, i.e. $T_{\mathrm{g}}(R) = T_{\mathrm{d}}(R) = T_{\mathrm{atm,irr}}(R)$, where $T_{\mathrm{atm,irr}}(R)$ is the atmospheric temperature defined by Eq. (5.13). Although Glassgold et al. (2004) and Kamp & Dullemond (2004) suggest the existence of an overheated layer above the superheated disk atmosphere, we did not consider this for simplicity's sake. In this model, assuming local thermodynamic equilibrium, the monochromatic intensity at frequency ν emitted by gas parcels at a distance R to the star and an azimuthal angle ϕ observed at inclination angle i ($i = 0°$ meaning face on disk) can be given by

$$
\begin{aligned}
I(\nu, R, \phi, i) &= B(\nu, T_{\mathrm{int}}(R))e^{-\tau(\nu,R,\phi,i)} + \\
&\quad B(\nu, T_{\mathrm{atm}}(R))\left(1 - e^{-\tau(\nu,R,\phi,i)}\right),
\end{aligned}
\tag{5.1}
$$

where $\tau(\nu, R, \phi, i)$ is the monochromatic optical depth of the disk atmosphere at a frequency ν along the line of sight, $B(\nu, T_{\mathrm{int}}(R))$ and $B(\nu, T_{\mathrm{atm}}(R))$ are the Planck functions of the dust temperature $T_{\mathrm{int}}(R)$ in the disk interior, and the gas temperature $T_{\mathrm{atm}}(R)$ in disk atmosphere, respectively. Regarding the disk inner edge, which has a temperature $T_{\mathrm{rim}}(R_0)$, it is assumed that it radiates as a blackbody ($I_{\mathrm{rim}}(\nu) = B(\nu, T_{\mathrm{rim}}(R_0))$), see Appendix 5.7.2 for details. The total

flux emerging from the protoplanetary disk seen by inclination angle i at frequency ν can thus be given as

$$
\begin{aligned}
F_{\text{disk}}(\nu, i) &= \int_{R_0}^{R_1} \int_0^{2\pi} I(\nu, R, \phi, i) \frac{R dR d\phi}{D^2} \cos(i) + \\
&\quad \frac{I_{\text{rim}}(\nu, R)}{D^2} A_{\text{rim}}(i) \cos(90 - i),
\end{aligned}
\tag{5.2}
$$

where R_0 and R_1 are the disk inner and outer radii and D is the distance of the source to the observer. In Eq. 5.2 $A_{\text{rim}} \cos(90 - i)$ is the visible area of the disk inner rim. If the disk inner rim were a perfect vertical wall, its surface area would be $A_{\text{rim}}(i) = 4\pi h(R_0) R_0^2$, where $h(R_0)$ is the disk aspect ratio at the inner edge, which is taken to be 0.05. In order to be consistent with the observations regarding the inclination-angle dependence of the rim flux (Isella & Natta 2005), the rim is taken to be a vertical wall seen under a constant 60 degree inclination angle.

To calculate the synthetic spectra numerically, we first set up the two-dimensional computational domain with N_{R} logarithmically distributed radial and N_ϕ equidistantly distributed azimuthal grid cells. For a given set of stellar parameters, shown in Table 5.1, first the grazing angle of the incident stellar irradiation is determined according to Eq. (5.10). The temperature distributions in the disk atmosphere and interior are calculated according to Eq. (5.13) and Eqs. (5.15, 5.17, 5.22, 5.23), respectively. After determining the dust surface-density of the disk atmosphere with Eq. (5.31), the optical depth along the line of sight is calculated by Eq. (5.33) using the gas opacity given by Eq. (5.34) and considering Eqs. (5.37)-(5.41) to calculate appropriate intrinsic line profiles and Doppler shifts. In order to determine the mass absorption coefficient of the $^{12}\text{C}^{16}\text{O}$ molecule we used the transition data provided by Goorvitch (1994), such as transition probability A, lower and upper state energy E_{l}, E_{u} and statistical weight g_{u}. Knowing the optical depth ($\tau(\nu, R, \phi, i)$), the temperature in disk atmosphere and interior in the 2D computational domain the expected flux along the line of sight can be calculated by applying Eq. (5.1) and Eq. (5.2) at each frequency in the vicinity of the investigated transition.

5.4 Disk models

In this section we describe in detail our disk models that fed into the synthetic spectral line model. As a first step, we calculated the disk surface-density and velocity distribution perturbed by a massive embedded planet with the publicly available hydrodynamical code FARGO of Masset (2000). A very important difference to the planet-free case is that the disk surface-density distribution is

very heavily modified. It shows a clear elliptic character of the gap opened by the giant planet. According to Kley & Dirksen (2006), D'Angelo et al. (2006), and also to our calculations (see below), the disk becomes eccentric after several hundred orbits of the embedded planet. With regard to our synthetic spectral line model, the most relevant are those effects that are originating from the gas dynamics caused by the giant planet. It is well known that a pure Keplerian motion of the gas parcels on circular orbits results in symmetric double-peaked emission line profiles (Horne & Marsh 1986). As the CO emission is strongly depressed $2 - 3\,\mathrm{AU}$ in our models, the origin of the double-peaked profiles is clear. Any deviation of the gas dynamics from the pure rotation will break this symmetry, resulting in the distortion of line profiles. If the distorting effect is strong enough, the line profile distortion could be significant to be detected by high-resolution spectroscopic observations.

Indeed several T Tauri stars show symmetric but centrally peaked CO line profiles that can be explained by radially extent CO emission overriding the double peaks (Najita et al. 2003; Brittain et al. 2009). Stronger CO emission can be expected if UV fluorescence plays a role (Krotkov et al. 1980), or the gas temperature is not well coupled to the dust (Kamp & Dullemond 2004; Glassgold et al. 2004). In the tenuous region above the disk atmosphere the gas can be significantly hotter than is predicted by the double-layer model. As a consequence the slowly rotating distant disk parcels could produce a substantial contribution to the low-velocity part of the line profile, resulting in a centrally peaked profile. Nevertheless, for simplicity's sake here we do not consider any of the above mentioned effects.

5.4.1 Hydrodynamical setup

We adopt dimensionless units in hydrodynamical simulations, for which the unit of length and mass is taken to be the orbital distance of the planet, and the mass of the central star, respectively. The unit of time, t_0, is taken to be the reciprocal of the orbital frequency of the planet, resulting in $t_0 = 1/2\pi$, setting the gravitational constant to unity. In each disk model we assigned four planetary masses to the embedded planet, which are in increasing order $q = m_{\mathrm{pl}}/m_* = 0.001$, 0.003, 0.005, and 0.008, where m_{pl} and m_* are the planetary and stellar masses. Regarding the disks geometry, the flat thin disk approximation was assumed with an aspect ratio of $H(R)/R = 0.05$. The disk extends between $0.2 - 5$ dimensionless units. This computational domain was covered by 256 radial and 500 azimuthal grid cells. The radial spacing was logarithmic, while the azimuthal spacing was equidistant. This results in practically quadratic grid cells, because

5. Detectability of embedded planets by Near-IR CO spectra

the approximation $\Delta R \sim R\Delta\phi$ is valid at each radius. The disks are driven by α-type viscosity (Shakura & Sunyaev 1973), which is consistent with our thermal disk model with an intermediate value of α, which was taken to be 1×10^{-3}. Note that assuming a cold disk (therefore virtually non-ionized) the viscosity generated by magnetohydrodynamical turbulence is hard to explain, although, according to Mukhopadhyay (2008), the transient growth of two or three-dimensional pure hydrodynamic elliptic-type perturbations could result in $\alpha \simeq 10^{-1} - 10^{-5}$, depending on the disk scale height (decreasing α with increasing scale height). The disk's initial surface density profile is given by a power law $\Sigma(R) = \Sigma_0 R^{-1/2}$, where the surface density at 1 distance unit Σ_0 is taken to be 2.15×10^{-5} in dimensionless units. For simplicity, an isothermal equation of state is applied for the gas, and the disk self-gravity is neglected. While the inner boundary of the disk is taken to be open, allowing the disk material to leave the disk on accretion timescale, the outer boundary is closed, i.e. no mass supply is allowed.

Below we assign physical units to the dimensionless quantities. If the stellar mass is assumed to be $m_* = 1 M_\odot$, the planetary masses in our models correspond to $1 M_J$, $3 M_J$, $5 M_J$, and $8 M_J$. Thanks to the dimensionless calculations it is possible to scale the results to different stellar masses. For different stellar masses, the mass of the giant planet scales with the stellar mass, i.e. $m_{pl} = 1 \times 10^{-3} m_*$, $3 \times 10^{-3} m_*$, $5 \times 10^{-3} m_*$, $8 \times 10^{-3} m_*$, and the stellar masses are taken to be $m_* = 0.5 M_\odot$, $1 M_\odot$, $1.5 M_\odot$. Furthermore, the distance unit is set to the distance of the planet to the star, i.e., the planet orbits at 1 AU. Below we extended our models to tight and wide systems, where the giant planets are orbiting at 0.5 and 2 AU, respectively. In $1 M_\odot$ stellar mass disk models the surface density at 1 AU is $\Sigma_0 = 2.15 \times 10^{-5} M_\odot \, \mathrm{AU}^{-2} \simeq 191 \, \mathrm{g/cm^2}$ at the beginning of simulation, which is also scaled with the mass of the central star. But note that the solution to the hydrodynamical system of equations is independent of Σ_0, if there is no back-reaction to the planet, see the vertically integrated Navier-Stokes equations in Kley (1999). For $0.5 M_\odot$, $1 M_\odot$ and $1.5 M_\odot$ stellar mass model the disk mass in the computational domain ($0.2 \, \mathrm{AU} \leq R \leq 5 \, \mathrm{AU}$) is $5 \times 10^{-4} M_\odot$, $1 \times 10^{-3} M_\odot$ and $1.5 \times 10^{-3} M_\odot$. These values refer to the mass of the inner disk only, as the whole disk may extend to several tens or hundreds of AU, and the total disk mass is in the conventional range of $0.01 - 0.1 M_\odot$. More details about the models can be found in Table 5.1.

TABLE 5.1: Stellar and disk parameters in our hydrodynamical models. The stellar parameters were taken from a publicly available tool (Siess et al. 2000). The disk extends between $0.2 - 5\,\mathrm{AU}$ and the orbital distance of the massive planets is $1\,\mathrm{AU}$.

Model No.	$m_* \, (M_\odot)$	$T_* \, (\mathrm{K})$	$R_* \, (R_\odot)$	$i \, (°)$	$m_\mathrm{p} \, (M_\mathrm{J})$
#1	0.5	3760	1.4	20,40,60	0.5
#2	0.5	3760	1.4	20,40,60	1.5
#3	0.5	3760	1.4	20,40,60	2.5
#4	0.5	3760	1.4	20,40,60	4
#5	1	4266	1.83	20,40,60	1
#6	1	4266	1.83	20,40,60	3
#7	1	4266	1.83	20,40,60	5
#8	1	4266	1.83	20,40,60	8
#9	1.5	4584	2.22	20,40,60	1.5
#10	1.5	4584	2.22	20,40,60	4.5
#11	1.5	4584	2.22	20,40,60	7.5
#12	1.5	4584	2.22	20,40,60	12

5.4.2   Synthetic spectral calculation setup

We calculate the spectral line of a fundamental band CO transition (V $= 1 \rightarrow 0$P(10), $\lambda_0 = 4.7545\,\mu$m), which is not blended by the higher excitation V=2$\rightarrow$1 and V=3$\rightarrow$2 lines, although in our thermal model the temperature is not high enough to excite the higher vibrational levels at all.[2] The CO rotational and vibrational level populations were calculated in local thermodynamical equilibrium. The line profiles were calculated in 200 wavelengths and in the same numerical domain that was used in hydrodynamical simulations. According to our preliminary tests on "circularly Keplerian"[3] disks, the CO fundamental band spectra did not show significant changes with increasing outer disk boundary. This can be explained by the fact that a substantial part of the CO fundamental band emission is arising in the inner disk, consequently the outer part of the disk ($R > 3 - 5$ AU, depending on the stellar mass) does not contribute to the disk emission at 4.7 micron. Contrary to this, the distance of the inner boundary of the disk to the central star heavily influences the CO fundamental band spectra, i.e. the closer the disk inner boundary to the star the line-over-continuum is weaker and broader. This is because the disk innermost regions give stronger contribution to the continuum, which in turn weakens the CO emission normalized to continuum, although the CO emission itself is also getting stronger due to an increased amount of hot CO. The line broadening is a natural consequence of the larger orbital velocity of gas orbiting closer to the star.

Because we investigate disks with already formed planets, it is reasonable to assume that a cavity is formed at the very inner disk like the ones found in disks of several T Tauri stars (Akeson et al. 2005; Eisner et al. 2005, 2007; Salyk et al. 2009). If dust evaporation takes place close to the star, the CO will be depleted too, due to the disappearance of the dust which protects the CO molecules against UV photo dissociation. In this way, the observed inner radius of CO (R_{CO}) should intuitively be similar or slightly larger than the dust sublimation radius R_{sub}. Indeed, R_{CO} was found to be larger than R_{sub} by a factor of a few in several disks, e.g., see Fig. 5. of Eisner et al. (2007) or Fig. 10 in Salyk et al. (2009). Contrary to this, Carr (2007) found that the CO inner radius is ~ 0.7 that of the dust. If the gas disk extends as far as 0.05 AU, there would be an additional broad component to the emission that is not modeled here. Taking these argumentations

---

[2] In our thermal model the temperature stayed below 1500 K everywhere in the computational domain. At this temperature the $V \geq 2$ vibrational levels are not thermally excited.

[3] We note that the term "Keplerian", widely used in the literature, here means "circularly Keplerian" motion. On the other hand, elliptic motion is also Keplerian, but below we will use the widely accepted nomenclature for circular motion, though we think it is not entirely correct.

into account it is reasonable to assume that the CO inner radius is set by the dust sublimation. The dust sublimation radius R_{sub} is given by

$$R_{\mathrm{sub}} \simeq 0.03 \left(\frac{T_*}{T_{\mathrm{sub}}} \right)^{5/2} \frac{R_*}{R_\odot} \mathrm{AU}, \tag{5.3}$$

where Eq. (5.13) with standard dust opacity law, $\beta = 1$ (Rodmann et al. 2006) was used. Assuming $T_{\mathrm{sub}} = 1500\,\mathrm{K}$ for dust sublimation temperature, $T_* \sim 4000\,\mathrm{K}$ and $R_* = 1.8\,R_\odot$ for stellar surface effective temperature and radius, appropriate for a 2.5 Myr solar mass star, we obtain $R_{\mathrm{sub}} = 0.05\,\mathrm{AU}$. To keep this simple, we set the disk inner boundary (namely the CO inner radius) fixed to $R_{\mathrm{CO}} \equiv 4R_{\mathrm{sub}} = 0.2\,\mathrm{AU}$, which is an acceptable value in disks hosted by T Tauri stars with 3500-5000 K surface temperature and $1.4 - 2.2\,R_\odot$ radius. Note that R_{sub} was fixed throughout our models (except the ones where we investigated the effect of the size of the inner cavity) to make them comparable, neglecting the effect of the change in stellar luminosity on the R_{sub}.

It is reasonable to assume that a disk that is $2.5\,\mathrm{Myr}$ old contains a considerable amount of gas and tracer CO also in the inner disk, hence the stellar age is taken to be $2.5\,\mathrm{Myr}$ in all models. Note that according to Haisch et al. (2001), half of the observed young stars in nearby embedded clusters (NGC 2024, Trapezium, IC 348, NGC 2264, NGC 2362, NGC 1960), with ages of about $3\,\mathrm{Myr}$, show near-IR excess, which is related to the excess emission of dust in disks. Furthermore, Hillenbrand (2005) also concluded that the median lifetime of the optically thick inner disk is between $2 - 3\,\mathrm{Myr}$.

In order to simplify the models it is assumed that the dust consists of pure silicates with $0.1\,\mu m$ grain size (Draine & Lee 1984). According to this the mass absorption coefficient of the dust is taken to be $2320\,\mathrm{cm}^2/\mathrm{g}$ at visual wavelength. Note that neither the effect of the coagulation nor the settling out of tenuous atmosphere of grains with a large size are taken into account. The size distribution and therefore the overall mass absorption coefficient of the dust is taken to be the same in the interior and the atmosphere. In this way the dust opacity is slightly overestimated. According to Eq. (5.33) the atmospheric gas density and thus gas line emission strength is slightly underestimated. The dust-to-gas and CO-to-gas mass ratios are assumed to be constant throughout the disk and are taken to be 10^{-2} and 4×10^{-4} (measured per gram of gas+dust mass) in the disk atmosphere and interior, respectively.

For the planet-free disks circular Keplerian velocity distribution is applied to determine the observed line center shift, given by Eq. (5.41). For a massive planet-bearing disk observed under inclination angle i, the Doppler shift of the emission from a single patch of gas in the disk
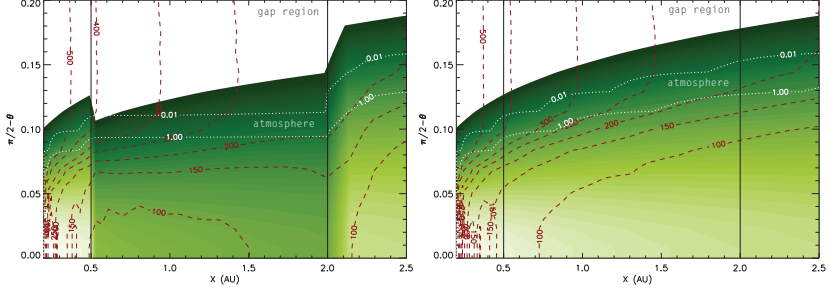
FIGURE 5.2: Logarithmic density (*green shaded* in g/cm^3) and temperature contours (*red dashed contours* in K) of the disk. The density contours are stopped at a gas density $\rho = 10^{-34}\,g/cm^3$ to avoid color crowding, while the maximum is $\rho = 10^{-11}\,g/cm^3$. The height of the disk atmosphere, i.e the range where the radial optical depth is less than 1 is shown with *white dotted lines* in the disk inner region. Comparing the unperturbed case (*left*) to the disk in which a gap exists at $0.5\,\mathrm{AU} < R < 2\,\mathrm{AU}$, after depleting the density by 1/1000 (*right*), it is appreciable that however the disk atmosphere is decreased in height, the temperature distribution is not considerably changed.

compared to its fundamental frequency ν_0 emerging from a given R, ϕ point is calculated by

$$\Delta\nu(R, \phi, i) = \frac{\nu_0}{c} \{u_\mathrm{R}(R, \phi) \left[\sin(\phi) + \cos(\phi)\right] + \\ u_\phi(R, \phi) \left[\cos(\phi) - \sin(\phi)\right]\} \sin(i), \tag{5.4}$$

where the radial $u_\mathrm{R}(R, \phi)$ and azimuthal $u_\phi(R, \phi)$ velocity components of gas parcels are provided by the hydrodynamic simulations.

The perturbations in the surface density distribution of the disk interior and atmosphere were not taken into account, because the disk atmosphere density given by Eq. (5.31) is independent of the density distribution of the disk even in the gap, as long as there is enough dust in the gap to keep it optically thick. To test the optical thick assumptions, let us for a moment neglect the effect of disk shelf-shadowing that occurs in the inner edge of the gap. Applying the dust density in the disk $\Sigma_\mathrm{d}(R = 1\,\mathrm{AU}) \simeq \Sigma_0 X_d$, where $X_d = 0.01$ is the dust-to-gas ratio and the dust opacity
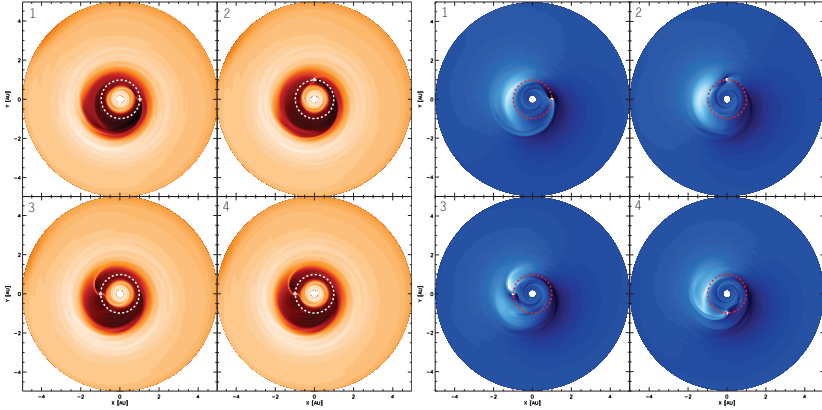
FIGURE 5.3: Surface density (*left four figures, orange colors* in the range of $0.2 - 250 \, \mathrm{g/cm^2}$) and the radial velocity component of the orbital velocity in the disk plane (*right four figures, blue colors* in the range of $-10.86 - +10.96 \, \mathrm{km/s}$) distributions of the disks gaseous material taken from four different azimuthal positions of the planet's 2000th orbit. In our model the total disk mass is $0.05 \, M_\odot$, the planet mass is $8 \, M_\mathrm{J}$, while the stellar mass is $1 \, M_\odot$. The planetary orbit is shown with a white and red dashed circle in the density and velocity plots. The gap (*in dark*) and the elliptic shape of its outer rim is clearly visible in the surface density distribution. In the vicinity of the gap the disk material shows a strong deviation from the circular Keplerian rotation, see the white clumps in the radial velocity component distribution.

5. Detectability of embedded planets by Near-IR CO spectra

$\kappa_V = 2320\,\mathrm{cm^2/g}$, in the gap, depleted to 0.1% of the surrounding density, the optical depth at visual wavelengths along the incident stellar irradiation is $\tau_V = \Sigma_d(R = 1\,\mathrm{AU})\kappa_V/\delta(R = 1\,\mathrm{AU}) \simeq 1000$. To argue that the shelf shadowing can be neglected we calculated the height of the disk atmosphere and temperature distribution in a planet-free and planet-bearing disk by a 2-D Monte-Carlo code RADMC for dust continuum radiative transfer (Dullemond & Dominik 2004a) with the same dust prescription as in our synthetic spectral model. In the planet-bearing disk model the gap is taken to be extended from 0.5 AU to 2 AU and artificially depleted in density to 0.1% that of the planet-free case. The amount of gap depletion is an average value measured in our hydrodynamic calculations. The results are shown in Fig. 5.2. It is evident that although the height of the disk atmosphere ($\tau_V = 1$ along the line of sight of stellar irradiation) above the mid-plane is decreased in the gap, the temperature in the disk atmosphere is not substantially changed. Because the temperature is not significantly decreased we neglect the surface density perturbations. Note that the effect of the distance of the gap from the central star on the shelf shadowing is not considered. The dust and gas temperature decoupling was also not taken into account. Because the gas has a temperature well in excess of the dust in depleted regions, where the gas column density is $\ll 10^{22}$ (Glassgold et al. 2004; Kamp & Dullemond 2004), we can expect increased contribution to the CO line flux originating from the gap. Contrary to this, if the base of the gap is shadowed completely by the inner wall, the gap does not contribute to the CO emission. Thus a gap could cause a strong permanent line profile asymmetry due to its asymmetric geometry (see Fig. 5.3), which requires further investigation.

Because the accretion heating has been taken into account according to Eq. (5.17), we had to set an appropriate accretion rate. The accretion rate measured in hydrodynamical simulations gives a value of about $2 \times 10^{-8}\,M_\odot/\mathrm{yr}$. Note that according to Fang et al. (2009) the accretion rate inferred from Hα emission luminosity in the young star population of Lynds 1630N and 1641 clouds in the Orion GMC with an age about $2-3\,\mathrm{Myr}$, is between $10^{-10} - 10^{-8}\,M_\odot/\mathrm{yr}$. In order to be consistent with the latter, the accretion rate is taken to be $5 \times 10^{-9}\,M_\odot/\mathrm{yr}$ for all our models. However, note that at this accretion rate the contribution of the viscous dissipation to the disk continuum is weak in the near-IR band.

5.5 Results

5.5.1 Effect of massive planets on the disk structure

Three groups of models were computed through 2000 planetary orbits, with stellar and planetary parameters listed in Table 5.1. In each run the planet was kept fixed on circular orbit during the first 1000 orbits. After the 1000th orbit the planet was released. It thus felt the (gravitational) backreaction of the disk, resulting in its inward migration. In a good accordance with the expectations, we found that a more massive planet opened a broader and deeper gap. The depletion is 0.25%-0.1% for planets with mass in the range of $1\,M_J - 8\,M_J$. After the first 1000 orbits a quasi steady state disk structure has developed in all simulations, which slightly changed during the following 1000 orbits, when the planet orbit was not fixed anymore.

To shed light on how the giant planet distorts the originally circularly Keplerian gas flow, several snapshots of density and velocity distributions were taken during the 2000th planetary orbit. Figure 5.3 shows four snapshots of the density and the radial velocity component of the orbital velocity of gas for an $8\,M_J$ mass planet orbiting an $1\,M_\odot$ star (model #8) during one orbit. It is evident that in a disk with an embedded massive planet the overall orbits of gas parcels are non-circularly Keplerian because the radial components of their orbital velocity distribution are strongly departing from zero. Moreover, we found that the elliptic gap, while preserving its shape, precesses slowly retrograde with a period of about 150 planetary orbits.

As we already mentioned, Kley & Dirksen (2006) found that an originally circular disk with an embedded giant planet can reach an *eccentric* equilibrium state if the mass of the embedded planet is larger than a certain limit ($3\,M_J$ for a $1\,M_\odot$ star). Kley & Dirksen found that for sufficiently wide gaps the growth of the eccentricity is induced by the interaction of the planet's gravitational potential with the disks material at the radial location of the 1:3 (outer) Lindblad resonance. For smaller planetary masses, this effect is damped mainly by the co-orbital and the 1:2 Lindblad resonances. If the gap is deep and wide enough, which is the case for a giant planet, the above resonances cannot damp the eccentricity-exciting effect appearing at the 1:3 Lindblad resonance, and the disk becomes eccentric. For a more detailed explanation of disk eccentricity growth see Lubow (1991a) and Kley & Dirksen (2006). The eccentric state of the disk in our simulations can also be clearly seen in Fig. 5.3 where the shape of the outer rim of the gap becomes elliptic in the surface density distribution.

The departure of the velocities of the gas parcels from the pure circularly Keplerian circular

5. Detectability of embedded planets by Near-IR CO spectra
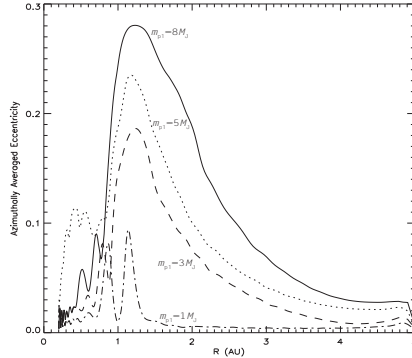

FIGURE 5.4: Azimuthally averaged eccentricities as the functions of radii after 2000 orbits of the giant planet. The eccentricity curves in models #5-#8 (where the planetary masses are $1\,M_J$, $3\,M_J$, $5\,M_J$ and $8\,M_J$ for $1\,M_\odot$ stellar mass) are shown with dot-dashed, dashed, dotted, and solid lines, respectively.

revolution can be characterized by calculating their eccentricities. Considering the eccentric equilibrium state of the disk, we expect that each gas parcel would move on a non-circular orbit, which may be characterized most conveniently by an average eccentricity value. Therefore, for each disk radius between 0.2 AU and 5 AU, the azimuthally averaged eccentricities of the orbits of the gas parcels were calculated in the following way

$$e(R) = \int_0^{2\pi} \sqrt{1 + 2h(R,\phi)c(R,\phi)^2}d\phi. \tag{5.5}$$

In Eq. (5.5) $c(R,\phi)$ and $h(R,\phi)$ stand for

$$c(R,\phi) = x(R,\phi)u_y(R,\phi) - y(R,\phi)u_x(R,\phi) \tag{5.6}$$

and

$$h(R,\phi) = \frac{u_x(R,\phi)^2 + u_y(R,\phi)^2}{2} - \frac{1}{\sqrt{x(R,\phi)^2 + y(R,\phi)^2}}, \tag{5.7}$$

where $u_x(R,\phi)$, $u_y(R,\phi)$ and $x(R,\phi)$, $y(R,\phi)$ are the Cartesian velocity components and coordinates at point R, ϕ. We found that the averaged eccentricities differ considerably from zero, and

each eccentricity curve reaches its maximum near the outer boundary of the gap (Fig. 5.4). A priori one would expect that the averaged eccentricity values are higher for more massive planets. Indeed we found that the maximum of the azimuthally averaged eccentricity is monotonically increasing with a planetary mass in the range of $1\,M_J \leq m_{pl} \leq 8\,M_J$. The eccentricity curve for the $8\,M_J$ mass planet peaks about $e_{max} \sim 0.3$, while the peak stays well bellow 0.1 for a $1\,M_J$ mass planet. Note that a very similar behavior of the disk eccentricity has already been found by Kley & Dirksen (2006). In their cases, however, the maximum of the eccentricity curves is somewhat lower than in our cases, and at least $3\,M_J$ is required to set the disk into eccentric state. This can be the consequence that we used an α-type viscosity in our simulations contrary to Kley & Dirksen (2006). The higher eccentricities we found are plausible inasmuch as Kley & Dirksen (2006) found that the eccentricity of the disk is increasing with decreasing viscosity and in our approach the kinematic viscosity $\nu(R) = \alpha H^2 \Omega_K(R)$ measured in dimensionless units is 2.5×10^{-6} at $R = 1$, which is smaller than the $\nu = 1 \times 10^{-5}$ used by Kley & Dirksen (2006).

As one can see, a giant planet has substantial impact on the density and velocity distributions of its host disk. It is an essential question, whether the velocity perturbations appear in the line-of-sight velocity with substantial strength. Figure 5.5 shows the subtracted distribution of the line-of-sight velocity in the perturbed and circularly Keplerian case. It is evident that the line-of-sight velocities show a significant departure from the circularly Keplerian fashion because the difference is non-vanishing. The radial velocity component of the orbital velocity and more importantly the line-of-sight velocity distributions have variable patterns following the planet on the top of a permanent excess seen at $0°$ and $180°$ position angle. Note that the the permanent pattern precesses slowly (with ~ 150 orbital periods), retrograde to the planet. The disk inclination angle i is taken to be $40°$ in the calculation of Fig. 5.5 and the disk was rotated to the line-of-sight in a way that the line-of-sight velocity component of dynamically perturbed gas parcels is maximized. Consequently we had expected that not only significant distortions appear in the line profiles, but that they vary in time within the orbital time scale of the giant planet. Because the deviation from circularly Keplerian velocity is in the range of $-7.92 - 4.88\,\mathrm{km/s}$, the width of variable component in the line profile should be $\sim 10\,\mathrm{km/s}$, depending on the inclination angle.

5.5.2 Distortion of CO lines

Below we address the following questions: (i) Does the line-of-sight component of the non-circularly Keplerian velocity distribution (Fig. 5.5) result in significant distortions in the CO
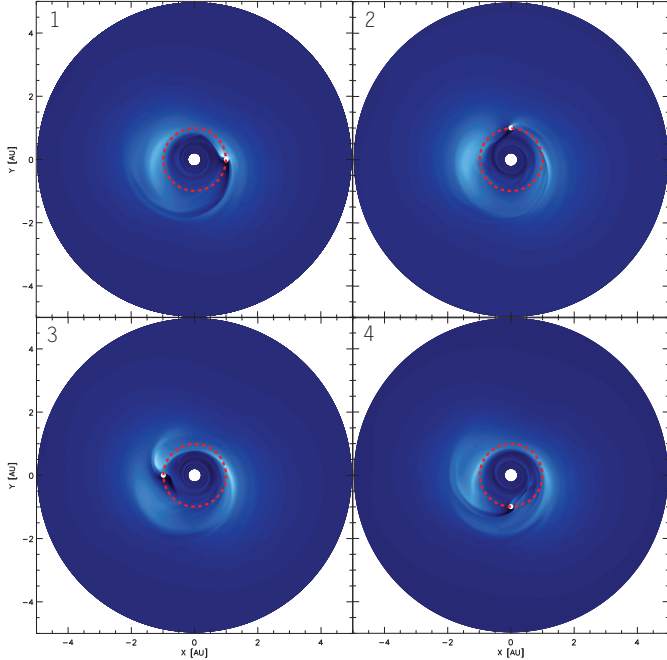
FIGURE 5.5: Offset of the line of sight component of the velocity distribution from circularly Keplerian values on the disk surface in the hydrodynamic simulations, in the same model presented in Fig. 5.3. Snapshots are calculated for four different azimuthal positions of the planet of the 2000th orbit. The velocity difference is in the range of $-7.92 - 4.88\,\mathrm{km/s}$. Here the inclination angle is taken to be $i = 40°$ and the viewing angle is taken to be $-90°$, i.e the disk is seen from the bottom of Fig. 5.3. The planetary orbit is shown with a red dashed circle. Two permanent high-velocity regions can be seen at position angle $0°$ and $180°$, and a variable pattern in the vicinity of the planet orbits. The strength of the variable component can reach that of the permanent one, e.g, in the panel at the bottom left (planet is at position angle $180°$).
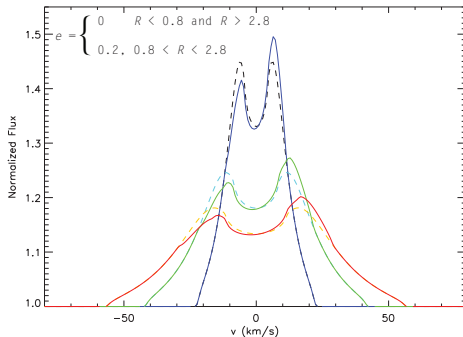
FIGURE 5.6: Asymmetric CO ro-vibrational line profile in a circularly Keplerian disk with a gap between $0.8 - 2.8\,\mathrm{AU}$ (similar to model #8), where the gas is flowing in eccentric orbit with $e = 0.2$. The gas outside the gap is in Keplerian circular orbit. It is evident that the line profiles are asymmetric. For comparison, we display the symmetric double-peaked line profiles (dashed lines) emerging from a planet-free disk as well.

spectral line profiles? (ii) Are these distortions varying in the planets orbital timescale? (iii) How do the distortions depend on the inclination angle, the planetary and stellar mass, the orbital distance of the planet, the size of the inner cavity and the disk geometry (if the disk is flared or not)? (iv) Are these distortions strong enough to be detected by high-resolution near-IR spectral measurements? A complete set of answers to the above questions may give us a novel method to detect massive planets embedded in protoplanetary accretion disks.

As was shown in Fig. 5.4 the disk eccentricity is considerable near the gap in all planet-bearing disk models. If the gas parcels move on pure elliptic orbits in the gap, the CO line profile becomes permanently asymmetric. This effect is illustrated in Fig. 5.6, where we have calculated the emerging line profile of a disk with an eccentricity $e = 0.2$ in the gap between $0.8\,\mathrm{AU} - 2.8\,\mathrm{AU}$ hosted by a $1\,M_\odot$ star viewed $20°$, $40°$ and $60°$ degree of inclination angles. Thus we can expect that the non-circularly Keplerian property of the velocity field shown in Figs. 5.3 and 5.5 will break the symmetry of the spectral lines. Although the orbits of the gas parcels can be characterized by average eccentricities, their orbits are more complicated than those of a pure elliptic motion, because of the perturbations induced by the planet.

First we examined the CO emission line profile distortions from a disk in which a $8M_J$ planet orbits a $1M_\odot$ star (model #8). As expected, the strongly non-circularly Keplerian velocity flow significantly modified the CO line profiles. In Fig. 5.8(a) we display the V=1-0 P(10) line profiles for three different inclination angles. The line profiles show a strongly asymmetric double-peaked shape. Studying Fig. 5.8 (a) two distortion patterns of the spectral line profiles can be recognized. An excess can be seen near the red peak of the lines at about $11\,\mathrm{km/s}$, $21\,\mathrm{km/s}$ and $29\,\mathrm{km/s}$, for inclinations $i = 20°$, $40°$ and $60°$, respectively. Moreover, a deficiency appears around the blue peak of each spectral line at slightly lower velocities. The above velocities correspond to the orbital velocity of the gas revolving around a $1\,M_\odot$ star at 0.8-0.9 AU, i.e. near the inner boundary of the gap, taking into account the appropriate inclination angles. Smaller-scale distortions also appear in the red and blue peaks as well, corresponding to the 0.8-2.9 AU region, i.e. the whole gap.

Calculating the line profiles at different orbital phases during one orbit, we found that the shape of the already distorted line profile varies in time, yielding a clear dependence on the orbital position of the planet, see results in Fig. 5.9 for model #8. The permanent asymmetry in lines is caused by the permanent velocity pattern seen at PA $0°$ and $180°$ in Fig. 5.5. Note that the expression "permanent" is not entirely correct because the velocity pattern slowly (~ 150 orbital periods of planet) precesses retrograde to the planet, but we still use it henceforward. The variable component indicated with arrows is moving in regions between $\sim \pm25\,\mathrm{km/s}$ due to the variable pattern following the planet. Note that the maximum width of variable component is $\sim 10\,\mathrm{km/s}$, as is expected, which is resolvable by CRIRES, whose maximum resolution is $3\,\mathrm{km/s}$. In this particular model the time scale of variations is on the order of weeks, because the orbital period of the planet is one year, thus the time elapsed between the snapshots is approximately 18 days.

5.5.3   Planetary and stellar masses

To gain further insights, it is useful to study the influence of the masses on the strength of the spectral line distortions. First we have investigated the cases in which a $1\,M_\odot$ star hosts a $1\,M_J$, $3\,M_J$, $5\,M_J$, and $8\,M_J$ mass planet at 1 AU, corresponding to models #5-#8. Parts of the results are presented in Fig. 5.8(b) for model #5 ($m_{\mathrm{pl}} = 1\,M_J$, $m_* = 1\,M_\odot$) and in Fig. 5.8(a) and Fig. 5.9 for model #8. One can conclude that for a less massive planetary companion the line profile distortions are weaker. The same conclusion can be obtained by the growing influence of the increasing planetary mass on the disk eccentricity, see Fig. 5.4.

A natural way to study the effect of the mass of the central star on the line profile distortions would be that the planetary mass is kept fixed, and the stellar mass is increased. On the other hand, we recall that dimensionless units were used in hydrodynamical simulations thus the mass of the planet is expressed in stellar mass units. Thus changing either the planet mass or the stellar mass is equivalent to changing the ratio between the planetary and the stellar mass. Therefore, one could conclude from the previous results that the larger the stellar mass, the stronger the line profile distortions. The situation is however a bit more complicated; if we change, for instance, the stellar mass, the luminosity of the star changes, which has an influence on the temperature distribution in the disk atmosphere and interior as well. The effect of the stellar mass can be therefore studied if the planetary-to-stellar mass ratio is kept fixed, while the mass along with the surface temperature and the stellar radius is changed in the synthetic spectral model. Due to the effect of the increased/decreased flux of stellar irradiation in case of the larger/smaller stellar mass, the outer boundary of the CO emitting region will be moved farther/closer to the star, and increased/decreased in size. To investigate the dependence of the observable line profile distortions on the stellar mass, we have recalculated the above presented line profiles for a $0.5\,M_\odot$ (models #1-#4) and a $1.5\,M_\odot$ (models #9-#12) central stars. Part of the results are shown in Fig. 5.8(c) (for model #4) and Fig. 5.8(d) (for model #12), respectively. Comparing the line profiles to those presented in Fig. 5.8(a) (for model #8), it is evident that the profiles are considerably narrower for $0.5\,M_\odot$ and broader for $1.5\,M_\odot$ models, due to the change in the Keplerian angular velocity $(\Omega_{\mathrm{K}}(R) = (Gm_*/R^3)^{1/2})$. Moreover, the line-to-continuum ratio at the maximum is slightly decreased and increased about a same amount for disks with 0.5 and $1.5\,M_\odot$ star. The change in line-to-continuum ratio can be easily explained: for a smaller mass star, the disk temperature is also decreased due to the decrease in stellar luminosity in a way that the ratio of the CO line to the disk plus star continuum is decreased too. The opposite is true for larger stellar masses. Finally, we can conclude that for a given planet-to-star mass ratio the larger the central stellar mass, the larger the observable CO line profile distortion caused by the giant planet. Here we have to note that although the observational data on T Tauri stars (Akeson et al. 2005) show that the size of the disk inner cavity is increasing with increasing stellar luminosity (which can be the consequence of the increased dust sublimation radius, see Eq. (5.3)), resulting in smaller continuum and stronger relative line strength, in our cases the size of inner cavity stayed fixed in order to make models comparable.

Analyzing Fig. 5.8(b) we conclude that the line profile distortions in model #5 ($m_{\mathrm{pl}} = 1\,M_{\mathrm{J}}$, $m_* = 1\,M_\odot$, 1 AU orbital distance) are so small that the giant planet signal below $1\,M_{\mathrm{J}}$ is strongly

suppressed. Note that a disk with a $1\,M_J$ mass planet embedded into it will not get into the eccentricity state at all, see Fig. 5.4. Planets orbiting the host star closer than 1 AU, however, can induce stronger distortions, as shown in the following section.

5.5.4 Orbital distance of the planet

In this section we investigate the effect of the orbital distance of the planet to the strength of the spectral line distortion. One would initially expect that the spectral line distortions are stronger/weaker as the orbital distance of the planet decreases/increases. We recalculated the hydrodynamical simulations in "tight" and "wide" models, where the planets orbit at 0.5 and 2 AU distances from the central star, respectively. In good agreement with the expectations, we found that the planet signature in the spectral line was strongly suppressed in the "wide" versions of models #1-#8, where $m_* = 0.5\,M_\odot$ and $m_* = 1\,M_\odot$. The reason for this is obvious: in wide systems the planet is orbiting in cold regions (the atmosphere temperature is varied between 200-350 K at 2 AU, depending on the stellar mass), where the atmospheric CO emission measured to the continuum is weak. As can be seen in Fig. 5.8(e), the "wide" version of model #8 ($m_{\rm pl} = 8\,M_J$, $m_* = 1\,M_\odot$, 2 AU orbital distance) shows considerably weaker planet signatures in the CO line profile than the original 1 AU model, see Fig. 5.8(a) for comparison. The distortion patterns appear at lower velocities owing to lower orbital velocities in $0.5\,M_\odot$ models. On the other hand, we found about the same strength of the planet signal in the "wide" version of model #12 ($m_{\rm pl} = 12\,M_J$, $m_* = 1.5\,M_\odot$, 2 AU orbital distance) as in model #8. This is expected, since in the latter case the luminosity of the host star is high enough to produce sufficient CO excitation even at 2 AU.

The resulting line profile calculated in the "tight" version of the model #8 ($m_{\rm pl} = 8\,M_J$, $m_* = 1\,M_\odot$, 0.5 AU orbital distance) is shown in Fig. 5.8(f). Because the giant planet orbits closer to the host star, where the disk atmosphere is heated to higher temperatures (the atmosphere temperature varies between 450-700 K at 0.5 AU, depending on the stellar mass), the emission emerging from the perturbed regions is stronger than in the original 1 AU models. It is also evident that the distorted peaks are slightly shifted to higher velocities compared to the original 1 AU models, because the orbital velocity of the gas parcels in dynamically perturbed orbits is higher in "tight" models. The disk is more eccentric on average in the latter case (Fig. 5.7), but the strength of the line profile distortion is increasing as the planetary orbital distance decreases. In order to demonstrate that smaller mass planets can also be detected in closer orbits we have calculated the
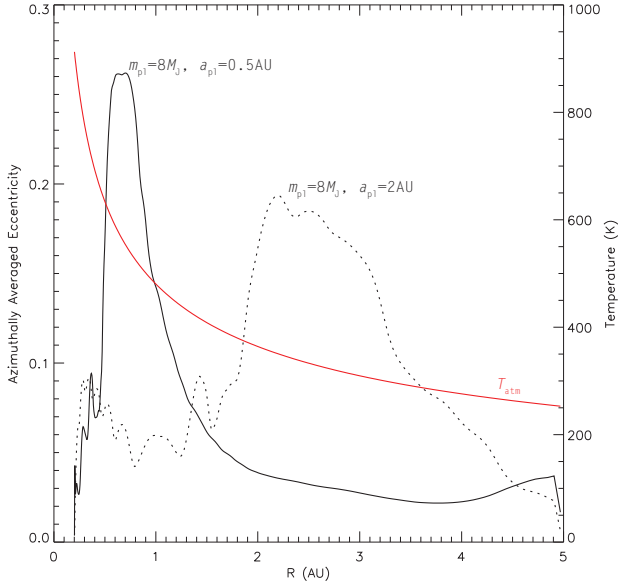
FIGURE 5.7: Azimuthally averaged eccentricities in the "wide" (dotted black) and "tight" (solid black) version of model #8 ($m_{\rm pl} = 8\,M_{\rm J}$, $m_* = 1\,M_\odot$) and the atmospheric temperature (red). It is apparent that even though the eccentricity maximum is smaller in the "wide" system, the disk is more eccentric on average than in the "tight" model. At the same time the planet signal becomes stronger in the "tight" (see Fig. 5.8(f)) than in the "wide" (see Fig. 5.8(e)) model, because the disk atmosphere is considerably hotter at 0.5 AU than 2 AU, where the disk is dynamically perturbed by the planet.

65

line profile in a "tight" version of model #2, $m_{\rm pl} = 1.5\, M_{\rm J}$, $m_* = 0.5\, M_\odot$, 0.5 AU orbital distance. We find that one could observe roughly the same strength line profile distortions as in model #8 ($m_{\rm pl} = 8\, M_{\rm J}$, $m_* = 1\, M_\odot$, 1 AU orbital distance).

5.5.5 Inner cavity size

Now we turn our attention to the question under which circumstances planets can be detected orbiting farther away from the star (farther than 2 AU for instance). In Sect. 3.2 we argued that there is a region around the star called inner cavity from which the CO is already depleted. In our simulations presented so far, we assumed that the radius of the inner cavity is fixed at 0.2 AU irrespective of the stellar luminosity. On the other hand, the size of the inner cavity is presumably dependent on the stellar mass, and indeed this is confirmed by observations (Akeson et al. 2005). As we mentioned in Sect. 3.2, the size of the inner cavity has a significant influence on the overall line-to-continuum ratio. In disks dynamically perturbed by planets orbiting at 1 AU and with a significant amount of CO lying inside 0.2 AU, the majority of CO flux is emerging from the unperturbed innermost regions, which eventually could smear out the planet signatures. On the contrary, if the size of the inner cavity is larger, the contribution of the perturbed regions to the total CO flux becomes stronger. In Fig. 5.8(g) we present the line profiles obtained in model #8, in which the inner cavity is increased to 0.4 AU in size, while the $8\, M_{\rm J}$ mass planet was still orbiting at 1 AU. As can be seen, the overall line-to-continuum ratio is decreased due to the absence of hot gas, but the level of the asymmetric pattern profile is more apparent than in models with an inner cavity extending only to 0.2 AU, see Fig. 5.8(a) for comparison. For larger inner cavities the continuum level of the disk interior and inner rim are decreased too, resulting in a moderate weakening of the line-to-continuum ratio and slight strengthening of planet signal. In this case the detection possibility of a planet orbiting at larger distances (> 2 AU) is growing.

5.5.6 Disk geometry

It is well known that many T Tauri sources present flatter than $\lambda F_\lambda \sim \lambda^{-4/3}$ SEDs. One attempt to explain this SED flattening was to assume that the disk is flaring (Kenyon & Hartmann 1987), resulting in a geometrically thicker disk atmosphere $H(R) \sim R^{\gamma+1}$, where γ is the flaring index. In the approach of Chiang & Goldreich (1997) the flaring index is $\gamma = 2/7$. In order to investigate the effect of disk geometry on the strength of the line profile distortions we recalculated several models using flat thermal disk approximation (the hydrodynamical inputs were the same). An
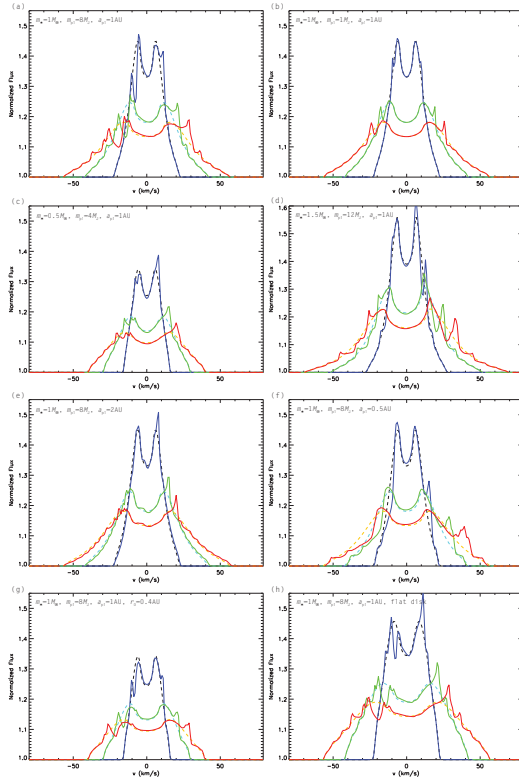
FIGURE 5.8: Distorted CO line profiles emerging in different models of planet-bearing disks. The disk inclinations were $20°$, $40°$ and $60°$ shown in blue, green and red colors. For comparison, we display the symmetric double-peaked line profiles (dashed lines) emerging from a planet-free disk as well. Line profiles shown in panel (a) and (b) show the dependence of the distortion strength on the planetary mass. In panels (c) and (d) the effect of stellar mass, in panels (e) and (f) the effect of the orbital distance is presented. The effect of the inner cavity size on the strength of the line profile distortions is presented in panel (g). The impact of the disk geometry is shown in panel (h), where the line profiles emerging in model #8 were calculated in flat-disk geometry. Note that the line profiles emerging in distinct models is calculated at orbital phases where the line profiles asymmetry is the most prominent, i.e., the orbiting planet is not always at the same position angle in each figure.
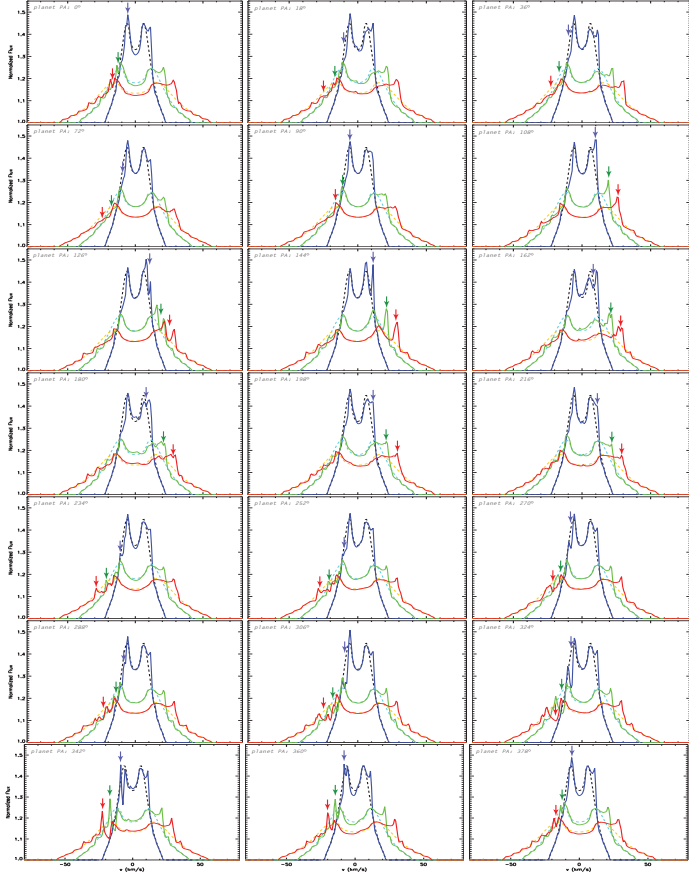
FIGURE 5.9: Permanent asymmetry and variations in the distorted CO ro-vibrational line profiles in a disk with an $8\,M_{\rm J}$ planet orbiting an $1\,M_{\odot}$ star at $1\,{\rm AU}$ (model #8). The subsequent epochs go across and down. The position angle (PA) of the giant planet is shown in each frame. The arrows point to the variable component moving in between $\sim \pm 25\,{\rm km/s}$. The normalized line flux is shown with the same scale as in Fig.5.8(a). The snapshots were calculated during one planetary orbit, thus about 2.5 weeks elapsed between the frames. The disk inclinations were $20°$, $40°$ and $60°$, shown in blue, green and red colors. For comparison, we displayed the symmetric double-peaked line profiles (dashed lines) emerging from a planet-free disk as well. As can be seen, the line profiles have permanent asymmetry and show a significant change in their shapes within weeks.

example of the flat version of model #8 ($m_{pl} = 8\,M_J$, $m_* = 1\,M_\odot$, 1 AU orbital distance) is shown in Fig. 5.8(h). Note that in order to have the same peak line-to-continuum ratio in flat as in flared models, the amount of emitting CO is arbitrary increased by decreasing the dust-to-gas ratio to 1.2×10^{-3} and keeping the disk mass unchanged. The reason for this is that although the atmospheric temperature does not differ in flared and flat disk models (see the atmospheric temperature given by Eq. (5.13)), the atmospheric surface density of CO is substantially smaller in flat than flared disk models (see the dependence of surface density given by Eq. (5.31) on the grazing angle, given by the first term of Eq. (5.10) in flat disk models). It is evident that the total line-to-continuum ratio is higher in the flat than in the flared disk model, but the line width at the wing of the line profile does not change. According to our calculations the line profile distortions in flat models compared to the flared one are less significant in "wide" systems where planets orbit at larger distances. This can be explained by the effect of flaring getting stronger with increasing distance to the host star.

5.5.7 Observational considerations

To observe the planet-induced distortions of the CO line profiles that we simulated, a spectroscopic facility is required that meets two basic demands: it needs sufficient spectral resolution to properly resolve the sub-structure in the line profile and sufficient sensitivity to bring out the low-contrast line profile distortions. In this section, we investigate the observability of the modeled effect in the context of contemporary facilities, and give a brief outlook into the ELT era. We present a quantitative example for the *CRyogenic high Resolution Echelle Spectrograph* (CRIRES) at the VLT (Kaeufl et al. 2004), which is currently the most powerful high-resolution spectrograph covering the M-band around $4.8\,\mu m$, capable of observing CO ro-vibrational spectra.

The main limiting factor for ground-based thermal infrared observations is the Earth atmosphere, which strongly absorbs the radiation from astronomical sources and causes a high thermal background. Particularly strong telluric absorption and emission is present at the wavelengths of low-excitation CO transitions. Within $\sim 10\,km/s$ from the line center the telluric transmission is so low and the background emission so high that these spectral regions are not accessible. However, depending on the location of the source with respect to the ecliptic, the CO features are Doppler shifted by up to $\pm 30\,km/s$ due to the Earth's orbital motion, making the whole CO line accessible over the course of several months, in principle. Note though that we can never measure the entire CO line profile simultaneously, there will always be an approximately $20\,km/s$ wide
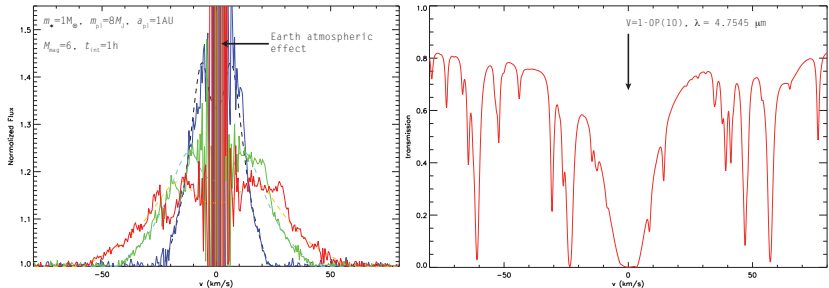
FIGURE 5.10: Effect of instrumental noise and atmospheric absorption on the observabil-
ity of line profile distortions (*left*) and the Earth atmospheric transmission at 4.7545μm
(*right*). The line profiles were calculated in model #8, shown already in Fig. 5.8(a), but
superimposed with an artificial noise expected for one hour of integration on $M_{mag} = 6$
brightness source with VLT/CRIRES.

"gap" in our spectral coverage at any observing epoch.

In order to test whether we would be able to detect the planet-induced permanent profile asym-
metries with currently available instrumentation, we have simulated a VLT/CRIRES observation
of model #8. We have assumed the source to have a brightness of $M = 6\,\mathrm{mag}$, and calculated
the achieved SNR as a function of wavelength using the VLT/CRIRES exposure-time calculator[4].
This calculation takes into account the telluric absorption and emission, the quality of the adaptive
optics correction, the system throughput and detector characteristics. We note that our simulation
only considers the signal-to-noise ratio, and assumes that systematic effects due to, e.g., time-
variable telluric absorption, can be well calibrated. The achieved SNR can be scaled according
to

$$SNR \propto 10^{0.4M} \sqrt{T_{\mathrm{int}}},\tag{5.8}$$

where M denotes the M-band magnitude and T_{int} the integration time. In Fig. 5.10 we show the
emerging V=1-0P(10) line profiles for model #8 (upper figure) and the atmospheric transmission

---

[4]We used version 3.2.8 of the ETC, assumed a water vapor column of 2.3 mm, an airmass of 1.4, a seeing of 1"0,
a slit width of 0"2, and adaptive optics correction using a guide star of $R = 10.0\,\mathrm{mag}$ and spectral type of M0V.
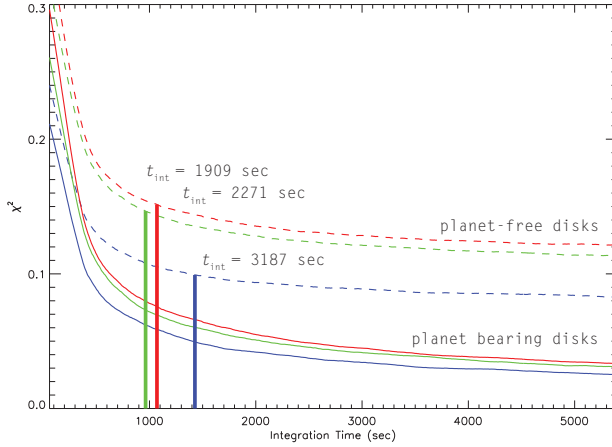
FIGURE 5.11: Goodness-of-fits of distorted line profiles contaminated with artificial noise obtained in planet-free (dashed lines) and giant planet-bearing disk (solid lines) models versus the integration time for $20°$, $40°$ and $60°$ inclinations, represented by blue, green and red colors, respectively. It is visible that for a reasonable signal-to-noise ratio, the planet-free models always provide fits with less confidence than the giant planet models, i.e the χ^2 is always larger. Moreover, the smaller the inclination angle, the larger the required minimal integration time ($t_{int} > 3187$ sec, 1909 sec and 2271 sec for the $20°$, $40°$ and $60°$ inclinations, respectively) to distinguish the planet-free and planet-bearing disk models.

71

5. Detectability of embedded planets by Near-IR CO spectra

(lower figure) for an assumed integration time of 1 hour on a source of $M = 6\,\text{mag}$. The model spectrum has been convolved with the 3 km/s CRIRES instrumental resolution. We have assumed zero relative velocity between the source and the Earth at the time of the observation. The effects of the telluric CO line are clearly seen around the line center, where no meaningful measurement can be obtained. The line wings, where the effects of the planet are most prominent, can be well measured.

In order to quantify the significance with which a planetary signal (the most prominent permanent asymmetric pattern) may be detected, we have tried to fit the modeled observation with both planet-free and planet-bearing models. In Fig. 5.11 we show the goodness-of-fits (reduced χ^2) as a function of integration time for both cases (with dashed line for planet-free and solid line for planet-bearing disk models) for $20°$, $40°$, and $60°$ inclination angles. Above a certain integration time (presented by vertical lines) the planet-bearing models yield a more than 50% better reduced χ^2 fit to the simulated data than those of the planet-free models. The asymmetric pattern induced by an embedded planet increase and thus become easier to detect with disk inclination.

Because the fundamental band ro-vibration R(0), R(1), R(12), R(13), R(19)-(21), R(25), R(26) and R(30)-(33), P(6-12) and P(22-32) CO lines are not blended by the higher vibrational lines[5], the line profiles can be averaged, using appropriate scaling, resulting in an increased signal-to-noise ratio. Note that the unblended lines with higher $J > 25$ or lower $J < 2$ rotational quantum numbers are too weak for averaging: using them would introduce only additional noise to the averaged profiles. Also note that, since the higher vibrational levels are not excited at all in disk atmospheres similar to that used in our models, the blended lines can also be used for averaging, resulting in an even more increased signal-to-noise ratio.

We conclude that in the confines of our model, the permanent asymmetric signals produced by an $8\,M_\text{J}$ giant planet orbiting at $\sim 1\,\text{AU}$ embedded in the disk of a T Tauri star of brightness $M = 6\,\text{mag}$ would be detectable with VLT/CRIRES with an integration time of 1 hour. Moreover, because the variable component at the top of the permanent asymmetry has a width of $\sim 5 - 10\,\text{km/s}$, exceeding the CRIRES $\sim 3\,\text{km/s}$ resolution, and $\sim 10\%$ magnitude, there is a certain possibility to strengthen its planetary origin.

With the next generation of giant, ground-base telescopes our sensitivity to low-contrast features in infrared spectra will increase greatly. We have used the ESO exposure-time calculator for the ELT (version 2.14) to simulate an observation with the proposed first generation infrared

---

[5]Assuming that the abundance of $^{12}\text{C}^{16}\text{O}$ isotopologues are low, thus their fundamental $V = 1 \rightarrow 0$ contribution to lines is negligible.

instrument *Mid-infrared E-ELT Imager and Spectrograph* (METIS) (Brandl et al. 2008). The exposure-time calculator necessarily incorporates planned telescope and instrument specifications, because this facility is yet to be built. We find that ELT/METIS yields an increase in sensitivity of a factor of ∼30 compared to VLT/CRIRES. Thus also sources that are substantially fainter or have weaker spectral features than those modeled here in the context of VLT/CRIRES are within reach of the observational facilities of the next decade.

5.6 Conclusions

We have shown that our semi-analytical 2D double-layer thermal disk model (in which the disk layers are heated mainly by stellar irradiation, and the emission of the disk inner rim is accounted for) is capable to reproduce the double-peaked Keplerian line profiles in CO fundamental ro-vibrational band in young (about $2.5\,\mathrm{Myr}$ old) T Tauri-type protoplanetary disks assuming canonical dust and gas properties. However, note that several T Tauri stars show centrally peaked symmetric profiles instead, which can be attributed to an enhanced CO flux formed in distant regions (up to 10 AU), presumably above the disk atmosphere. This can be explained by non-LTE heating, such as UV fluorescence (Krotkov et al. 1980), or dust gas temperature decoupling (Glassgold et al. 2004; Kamp & Dullemond 2004), resulting in highly excited CO emissions. These effects were not taken into account in our calculations. Thus the gas temperature at disk atmosphere provided by our thermal model is presumably somewhat lower than the realistic one. Our predictions, however, demonstrate a "the worst case" because the planet signal is getting stronger with increasing atmospheric temperature. It is revealed that significant line profile distortions appear in the CO fundamental ro-vibrational band caused by a giant planet. As we have demonstrated, a giant planet with a mass of at least $1\,M_\mathrm{J}$ can perturb the disk sufficiently to be detected by permanent asymmetry in line profiles and its short timescale variations. The permanent asymmetry in line profiles can be interpreted by the disk being in an eccentric state only in the gap, but the short timescale variability is certainly connected to the local dynamical perturbations of the orbiting planet. Depending on the signal-to-noise ratio and the resolution of the spectra, even lower-mass giant planets can be detected revolving on close orbits in disks observed with high-inclination angles and with large size inner cavities. The summary of our findings is:

(1) The dynamical perturbation induced by a giant planet significantly distorts the CO ro-vibrational fundamental emission line profiles.

5. Detectability of embedded planets by Near-IR CO spectra

(2) The line profile distortions are more apparent for larger inclination angles.

(3) The main component of line profile distortions is a permanent asymmetry. Its position in the line profile depends on the stellar mass and orbital distance of the planet. The permanent asymmetry shape depends on the orientation of the gas elliptic orbit with respect to the line of sight.

(4) The line profiles are changing with time, correlated to the orbital phase of the giant planet. The timescale of the variation is on the order of weeks, depending on the orbital period of the planet, i.e, the orbital distance and the mass of the host star. The magnitude of variable component is $\sim 10\%$, its width is $\sim 10\,\mathrm{km/s}$, depending on the inclination angle.

(5) The planet signal becomes stronger with increasing planetary mass.

(6) The planet signal strengthens/weakens with increasing/decreasing mass of the host star, neglecting the effect of the stellar luminosity on the size of the inner cavity

(7) The planet signal strengthens/weakens with decreasing/increasing orbital distance of the planet.

(8) The size of the inner cavity has a strong influence on the giant planet observability. If the size of the inner cavity is substantially smaller than 0.2 AU, we can detect a giant planet only at close (about 0.5 AU) orbit. On the contrary, if the cavity is larger (0.4 AU), a distant planet (in 2 AU orbital distance) can also be detected.

(9) The influence of disk geometry on the planet signal is modest. With a decreasing flaring index the strength of planet signal does not change although the line profiles are strengthened, except in "wide" flat models where the planet signal substantially suppressed.

(10) The lowest mass of giant planet orbiting at 1 AU that still can be detected is $0.5\,M_\mathrm{J}$ for a $0.5\,M_\odot$ star in the confines of our models.

(11) By high-resolution near-IR spectroscopic monitoring with VLT/CRIRES, giant planets with $\geq\ 1\,M_\mathrm{J}$ mass orbiting within 0.2-3 AU in a young disks may be detectable, if other phenomena do not confuse, mimic, or obscure the planet signature. The level of confidence is growing with increasing inclination angle.

In the light of our findings, we propose to observe T Tauri stars that shows an appreciable amount of CO in emission with high-resolution near-IR spectrograph to search for giant planet companions. The asymmetric and time-varying double-peaked line profiles can be explained by strongly non-circularly Keplerian gas flow in the disk caused by the giant planets, as was presented. Although higher $V \geq 2$ vibrational states of CO are not excited in our models, overlaps can occur, resulting in asymmetric line profile. To avoid this, one should consider only non-blended lines for profile averaging such as P(6)-P(12), and R(0), R(1), R(12), R(13), R(19)-(21), R(25), R(26) and R(30)-(33). Another possible source of permanent line profile distortions could be a large companion deforming the circumprimary disk to fully eccentric in mid-separation binaries (e.g. Kley et al. (2008); Regaly et al. in prep.). Last but not least, the distorted PSF, caused by tracking errors of the telescope or unstable active optics during an exposure, can induce artificial signals. A real signal from a bipolar structure will change sign when observed using antiparallel slit position angles whereas the artificial signal will not. Thus artificial signatures can be successfully identified with the comparison of the spectra of disks obtained at two antiparallel slit position angles, e.g. $0°$ and $180°$ (Brannigan et al. 2006). By detecting short time-scale (weeks to months) variations of the asymmetric profiles with similar patterns as presented in Fig. 5.9, we could infer the presence of a giant planet in formation.

The proposed instrument METIS for the ELT (Brandl et al. 2008), providing high-resolution ($\lambda/\Delta\lambda = 10^5$) infrared spectroscopy with an increase in sensitivity of a factor of ~ 30 to that of VLT/CRIRES will give the opportunity to even decrease more the mass and brightness limits of possible giant planets. If we revealed for instance the distance of the observed planets to the star as a function of the age of the star-disk system, we would be able to constrain planetary migration models. Moreover, determining the youngest star host planet-bearing disks could also provide constraints on planet-formation models.

Although our assumptions are reasonable from the point of view of finding a simple model of the signal of dynamical perturbations, it can be developed further of course. For example, if the gap is cleared by the planet to a fraction of the surrounding density, the disk is not directly irradiated, but is shadowed by the inner wall of the gap (Varnière et al. 2006). This mild heating causes a temperature drop at the inner gap wall, which results in a depressed CO flux. On the other hand, the outer edge of the gap is directly illuminated by the star, resulting in a slight temperature increase, which produces stronger CO emission from the regions where the eccentricity reaches its maximum (see e.g. Fig.5.4). According to our results the gap is strongly non-axisymmetric, thus 3D radiative transfer using 3D density structure needed to calculate the real temperature pro-

file in perturbed disks. Moreover, as the gap is depleted in large grains because of the trapping of dust grains larger than $\sim 10\,\mu m$ (Rice et al. 2006), the CO flux normalized to the continuum is strengthened. The gas and dust can be thermally uncoupled (see e.g., Glassgold et al. (2004); Kamp & Dullemond (2004); Woitke et al. (2009)) in the tenuous gap, which may result in CO being overheated to the dust. These effects could cause additional permanent line profile distortions due to the elliptic shape of the gap seen in density distribution (Fig. 5.3). If we consider an excess emission originating from the planetary accretion flow suggested by Clarke & Armitage (2003), or the density waves in disk surface caused by the orbiting planet, it would cause a varying planet signal. To these caveats, one might also consider the disk turbulence (e.g., due to MRI effects), which may add random asymmetries and "blobbiness" to the line profiles. We will investigate these effects in a forthcoming paper using a more sophisticated thermal disk model.

CO exists inside the dust sublimation radius in some T Tauri stars (Carr 2007) or Herbig Ae/Be stars (Brittain et al. 2009), where the disk is optically thin in the absence of dust. One possibility to excite CO in the optically thin inner disk close to the stellar surface is the UV fluorescence, which is far from LTE (Krotkov et al. 1980) applied in our calculations. Depending on the efficiency of X-ray heating the gas temperature can be as high as $\sim 4000 - 5000\,K$. Somewhat below this temperature, where CO still exists, the high-excitation vibrational levels of CO such as $V \geq 2$ are populated, resulting in significant $V = 2 \to 1$, $V = 3 \to 2$, etc. ro-vibrational lines. According to Skrutskie et al. (1990), the inner cavity in transitional disk may be formed by a close giant planet. Indeed, Lubow & D'Angelo (2006) found that an $1-5M_J$ mass planet significantly lowers the accretion of dust and gas to 10%-25% of the accretion rate outside the gap. We expect that the planetary signal forming in the optically thin inner disk is also detectable, which is strongly supported by the revealed line profile distortion strengthening with decreasing orbital distance of the planet. The UV pumping requires considerable UV flux from the central star, which is a characteristic of Herbig Ae/Be stars rather than smaller T Tauri stars. Considering that the CO may be excited up to to 10 AU by UV fluorescence (Brittain et al. 2007, 2009) in Hebig Ae/Be stars, planet orbiting at larger distances than 2 AU may be also detectable by CO ro-vibrational line profile distortions.

Spectroscopy of T Tauri stars shows emission of molecules such as H_2O, OH, HCN, C_2H_2, and CO_2, as well. Nevertheless CO is more abundant than these molecules by ~ 10 times, only H_2O could reach the abundance of CO, predicted by recent models that calculate the vertical chemical structure of the gas in disk atmosphere (e.g. Glassgold et al. (2004), Kamp & Dullemond (2004), and Woitke et al. (2009)). Indeed in some cases, like AA Tau (Carr & Najita 2008), and

AS 205A and DR Tau (Salyk et al. 2008), the rotational transitions of H_2O dominate the mid-infrared $(10-20\,\mu m)$ spectra, suggesting that H_2O is abundant in disk atmospheres. The strong water emission could be the consequence of turbulent mixing that carries molecules from the disk midplane, where they are abundant, to the disk atmosphere (Carr & Najita 2008), or the effects of an enhanced mechanical heating of the atmosphere (Glassgold et al. 2009). While the H_2O ro-vibrational lines probe the inner regions of disk out to radii $\geq 2\,AU$, the rotational lines are produced between radii 10-100 AU (Meijerink et al. 2008). The rotational and ro-vibrational line profiles of water are also subject to distortions caused by the dynamical perturbations of a giant planet. Thus it is reasonable to search for signature of giant planets in the high-resolution spectra of H_2O in the mid-infrared band (for planets orbiting int the inner disk), and rotational spectra of H_2O in the far-infrared band (for planets orbiting in the outer disk), as well. Because H_2O is heated by stellar X-rays and sub-thermally populated beyond 0.3 AU, X-ray-heating and non-LTE level population treatment is needed to calculate water lines (e.g., Meijerink et al. (2008); Kamp et al. (2010)).

Finally, we point out some noticeable resemblance to our findings revealed in observed CO line profiles. The V836 Tau transitional disk shows strongly distorted $4.7\,\mu m$ CO ro-vibrational line profile presented by Najita et al. (2008). The averaged CO line profiles shows very similar features to our results. According to Najita et al. (2008) the possibility of a massive planet is also restricted by current limits on the stellar radial velocity of V836 Tau, which constrain the mass of a companion within $0.4-1\,AU$ to $5-10\,M_J$. Because the disk extents to a limited range of radii $(\sim 0.05-0.4\,AU)$, the dynamical perturbation of a close orbiting planet with a mass smaller than $5\,M_J$ presumably could cause the observed line profile distortions. Note that radial velocity measurements indicate that no planet is present larger than $1-2\,M_J$ closer than $\sim 0.5\,AU$ (Prato et al. 2008). The transitional disks that encompass the young sources SR 21 and HD 135344 B have been observed by VLT/CRIRES (Pontoppidan et al. 2008) and they already show clear line profile asymmetries in CO fundamental ro-vibrational band. Our scenario of a planet is a reasonable explanation of the asymmetry. The presence of a planet was also proposed by Grady et al. (2009) for HD 135344 B and Eisner et al. (2009) for SR 21, based on SED and visibility data, respectively. EX Lupi (prototype of EXor type young variable stars) showed remarkable line profile variations during its 2008 outburst (Goto et al. 2010, in prep.). Goto et al. revealed that the CO emission has a spatially multiple origin. The quiescent component forms in the outer optically thick disk, while the outburst component in the inner optically thin gas disk, where the higher vibrational levels of CO are presumably excited by UV pumping. These high-excitation $V=2\to1$ and $V=3\to2$

lines are double peaked, strongly asymmetric and variable on a short (weekly) time scale. Thus for example, by measuring short timescale (on the order of weeks or less) periodic variations in the CO ro-vibrational spectra of these sources, by mid-IR monitoring observations would eventually indirectly detect an embedded Jupiter-like planet in birth.

5.7 Detailed description of the spectral model used

5.7.1 Temperature distribution in the disk

For the sake of completeness we present here the derivation of the dust temperature distributions in the disk interior and atmosphere according to Chiang & Goldreich (1997). Below we use the local thermodynamical equilibrium (LTE) assumption everywhere. The stellar flux in the disk atmosphere at a distance R from the stellar surface is

$$F_*(R) \simeq \frac{\delta(R)}{2} \left(\frac{R_*}{R}\right)^2 \sigma T_*^4, \tag{5.9}$$

where $\delta(R)$ is the grazing angle of the incident irradiation, R_* and T_* are the stellar radius and surface temperature, respectively, and σ is the Stefan–Boltzmann constant. Here we assumed that only half of the stellar surface is visible from a given point at a distance R from the star in the disk atmosphere. According to Chiang & Goldreich (1997) the grazing angle can be given by

$$\delta(R) = \frac{2}{5}\left(\frac{R_*}{R}\right) + \frac{8}{7}\left(\frac{T_*}{T_g}\right)^{4/7}\left(\frac{R_*}{R}\right)^{-2/7}, \tag{5.10}$$

in a flared disk assumed to be in hydrostatic equilibrium. In Eq. (5.10) T_g is the gravitational temperature at which the thermal energy of gas parcel balances the gravitational energy at the stellar surface, which can be given by

$$T_g = \frac{GM_* m_H}{k R_*}, \tag{5.11}$$

where m_H is the mean molecular weight of the gas, G and k is the gravitational constant and Boltzmann constant, respectively. Note that for a non-flared, i.e flat disk the grazing angle is defined by only the first term of Eq. (5.10).

By definition the optical depth of the disk atmosphere along the incident stellar irradiation is $\tau_V = 1$ in the optical wavelengths. The optical depth of the atmosphere at near-IR heated to

$T_{\text{atm,irr}}(R)$ perpendicular to the disk plane is $\tau_V \delta(R)\epsilon_{\text{atm}}(R)$, where $\epsilon_{\text{atm}}(R) = (T_{\text{atm,irr}}(R)/T_*)^\beta$ is the dust emissivity, and β is the power law index of the absorption coefficient of the dust, see Appendix 5.7.3 for details. The total flux emitted inward and upward by the optical thin atmosphere can be given by

$$F_{\text{atm}}(R) = 2\delta(R)\epsilon_{\text{atm}}(R)\sigma T_{\text{atm,irr}}(R)^4. \tag{5.12}$$

In LTE the absorbed flux of atmosphere equals to the emitted one ($F_*(R) = F_{\text{atm,irr}}(R)$), thus the disk atmosphere is heated to the temperature

$$T_{\text{atm,irr}}(R) = \left(\frac{1}{4}\right)^{1/(4+\beta)} \left(\frac{R_*}{R}\right)^{2/(4+\beta)} T_* \tag{5.13}$$

by stellar irradiation.

Assuming that the disk interior with a temperature $T_{\text{int,irr}}(R)$ is optically thick to its radiation everywhere in our computational domain,[6] the flux $F_{\text{int,irr}}(R)$ emitted by the disk interior is

$$F_{\text{int,irr}}(R) = \sigma T_{\text{int,irr}}(R)^4. \tag{5.14}$$

Considering that the absorbed stellar flux will be re-emitted by the disk atmosphere upward and downward only half of this flux heats the interior, i.e $0.5F_{\text{atm}}(R) = 0.5F_*(R) = F_{\text{int,irr}}(R)$. Accordingly, the temperature of the disk interior set by the stellar irradiation can be given by

$$T_{\text{int,irr}}(R) = \left(\frac{\delta(R)}{4}\right)^{1/4} \left(\frac{R_*}{R}\right)^{1/2} T_*. \tag{5.15}$$

Owing to the accretion process a significant amount of gravitational potential energy has to be dissipated by a viscous processes. According to Lynden-Bell & Pringle (1974), in a steady state disk[7] with a constant accretion rate $\dot{M}$, the flux $F_{\text{acc}}(R)$ released by the disk mid-plane due to the change of potential energy can be given by

$$F_{\text{acc}}(R) = \frac{3GM_*\dot{M}}{8\pi} \left(1 - \left(\frac{R_*}{R}\right)^{1/2}\right) R^{-3}. \tag{5.16}$$

In this way the disk mid-plane is heated to the temperature

$$T_{\text{acc}}(R) = \left[\frac{3GM_*\dot{M}}{8\pi\sigma} \left(1 - \left(\frac{R_*}{R}\right)^{1/2}\right)\right]^{1/4} R^{-3/4}. \tag{5.17}$$

---

[6]As mentioned before, in the computational domain, the disk interior remains optically thick to its own radiation.

[7]The disk being in steady state means that the density distribution corresponding to the surface density distribution does not considerably change in time.

Here we have to note that only half of the total accretion power is involved in Eq. (5.16), the remaining is stored in the kinetic energy of orbiting gas. This energy should be radiated away by the disk boundary layer (Popham et al. 1993, 1995) or by the accreting material in the funnel flow formed along the magnetic field lines in magnetospheric accretion model, see Hartmann et al. (1994); Bouvier et al. (2007). Because the disk boundary layer and the funnel flows are confined into such small volumes that the gas temperature reaches about 10000K emitting in the UV band, its radiation is not taken into account.

Now let us take into account the heating due to viscous dissipation in disk interior using the superposition principle, i.e the radiation at a given location is the sum of the radiations corresponding to different heating sources. To determine the disk interior temperature $T_{\mathrm{irr,acc}}(R)$ caused by the viscous dissipation first assume that the flux emitted by the optical thick disk interior is

$$F_{\mathrm{int,acc}}(R) = \sigma T_{\mathrm{int,acc}}(R)^4. \tag{5.18}$$

Because the disk mid-plane radiates the accretion flux into two directions $0.5F_{\mathrm{acc}}(R) = F_{\mathrm{int,acc}}(R)$, the disk interior is heated to

$$T_{\mathrm{int,acc}}(R) = (1/2)^{1/4} T_{\mathrm{acc}}(R) \tag{5.19}$$

by accretion. Taking into account the heating of the disk interior by irradiation of atmosphere and viscous dissipation together (simply summing the radiation fluxes), the resulting temperature of disk interior is

$$T_{\mathrm{int}}(R) = \left(T_{\mathrm{int,irr}}(R)^4 + T_{\mathrm{int,acc}}(R)^4 \right)^{1/4}. \tag{5.20}$$

5.7.2 Emission from the disk inner rim

To determine the temperature profile of the disk interior close to the disk inner edge, where the simple double-layer assumption cannot be applied, we first assume that the rim is a perfect vertical wall. Any given optically thick vertical slab with a thickness of dR at $R + dR$ distance from the central star is irradiated by the neighboring hotter slab located at R. Assuming that half of its radiation is received by the one at $R + dR$, the emitted and irradiated fluxes are in equilibrium in LTE, i.e.

$$\frac{1}{2}\sigma T_{\mathrm{rim}}(R)^4 = \sigma\epsilon(R) T_{\mathrm{rim}}(R + dR)^4, \tag{5.21}$$

where $\epsilon(R) = (T_{\rm rim}(R + dR)/T_{\rm rim}(R))^\beta$ is the emissivity of the slab at $R + dR$, see in Appendix 5.7.3. Note that here we neglect the irradiation of the neighboring slab at $R + 2dR$ with a lower temperature than the slab at $R + dR$. To calculate $T_{\rm rim}(R)$, we first approximate $T_{\rm rim}(R + dR)$ with $T_{\rm rim}(R) + T'_{\rm rim}(R)dR$. This results in an ODE for $T(R)$, which has the solution

$$T_{\rm rim}(R) = T_{\rm rim}(R_0) \exp\left[-\left(1 - \left(\frac{1}{2}\right)^{1/(4+\beta)}\right)(R - R_0)\right], \tag{5.22}$$

where R_0 is the radius of the disk inner edge. To take into consideration the additional irradiation of the rim at the opposite side, we assume that the temperature at the innermost slab is $T_{\rm rim}(R_0) = qT_{\rm int,irr}(R_0)$, where $q \simeq 1.2$ according to results of our simulations done by 2D RADMC (Dullemond & Dominik 2004a). Thus incorporating the additional heating by the disk rim, the disk interior temperature, previously given by Eq. (5.20), can be given by

$$T_{\rm int}(R) = \left(T_{\rm int,irr}(R)^4 + T_{\rm int,acc}(R)^4 + T_{\rm rim}(R)^4\right)^{1/4}. \tag{5.23}$$

where the superposition rule is applied.

5.7.3 Dust emissivity

In this section the derivation of dust emissivity at a specific temperature is given, assuming optically thick environment. Let us define the dust emissivity at a temperature $T_{\rm dust}$ heated by a blackbody of the temperature $T_{\rm irr}$ as the ratio of the Rosseland mean opacities

$$\epsilon_{\rm dust} = \frac{\langle\kappa(T_{\rm dust})\rangle_{\rm R}}{\langle\kappa(T_{\rm irr})\rangle_{\rm R}}. \tag{5.24}$$

The Rosseland mean opacity is defined by

$$\langle\kappa(T)\rangle_{\rm R} = \frac{\int_0^\infty dB(\nu, T)/dT d\nu}{\int_0^\infty dB(\nu, T)/dT \kappa(\nu, T)^{-1} d\nu}, \tag{5.25}$$

where $B(\nu, T)$ is the Planck function. The dust used in our model generates the $\kappa(\nu) = \kappa_0(\nu/\nu_0)^\beta$ opacity law, where $\beta > 0$. Note that wee use $\beta = 1$ throughout all our models (Rodmann et al. 2006). Following the calculations of Stahler & Palla (2005), we assume that the dust absorption coefficient can be given by

$$\kappa(\nu, T) = \kappa_0\left(\frac{kT}{h\nu_0}\right)^\beta x^\beta, \tag{5.26}$$

where k and h are Boltzmann and Planck constants, respectively, and $x = h\nu/kT$. Supposing that

$$\partial B(\nu, T)/\partial T\,d\nu = Af(x)dx, \tag{5.27}$$

where A is an appropriate dimensional constant, and substituting this into the definition of Rosseland mean opacity, Eq. (5.25), leads to

$$\langle \kappa(T) \rangle_{\mathrm{R}} = \kappa_0 \left(\frac{kT}{h\nu_0} \right)^\beta \frac{\int f(x)dx}{\int x^{-\beta} f(x)dx}. \tag{5.28}$$

Because the quotient of integrals is a pure number, the Rosseland mean opacity is proportional to T^β. Applying 5.24 and 5.28 we find that the dust emissivity can be given by

$$\epsilon_{\mathrm{dust}} = \left(\frac{T_{\mathrm{dust}}}{T_{\mathrm{irr}}} \right)^\beta. \tag{5.29}$$

5.7.4   Optical depth of the disk atmosphere

Assuming that the disk is observed with an inclination angle i, the monochromatic optical depth of the disk atmosphere is the sum of optical depths of dust and gas along the line of sight, i.e.:

$$\tau(\nu, R, \phi, i) = \frac{1}{\cos(i)} \left(\kappa_{\mathrm{d}}(\nu)\Sigma_{\mathrm{d}}(R) + \kappa_{\mathrm{g}}(\nu, R, \phi, i)\Sigma_g(R) \right), \tag{5.30}$$

where $\kappa_{\mathrm{d}}(\nu)$ and $\kappa_{\mathrm{g}}(\nu, R, \phi, i)$ are the dust and gas opacity at frequency ν, while $\Sigma_{\mathrm{d}}(R)$ and $\Sigma_g(R)$ are the dust and gas surface densities in the disk atmosphere. Note that because the dust opacity (κ_{d}) is taken to be uniform throughout the disk, the optical depth of the disk atmosphere depends on R and ϕ via the gas opacity characterized by the temperature distribution and the line-of-sight component of the orbital velocity of gas parcels. By definition the optical depth at the bottom of the disk atmosphere is unity at optical wavelengths along the stellar irradiation. Assuming that the only opacity source at visual wavelengths is the dust, the dust surface-density of disk atmosphere is

$$\Sigma_{\mathrm{d}}(R) = \frac{\delta(R)}{\kappa_{\mathrm{V}}}, \tag{5.31}$$

where κ_{V} is the overall opacity of dust at visual wavelengths. Assuming that the gas- and dust-mass ratio to the total mass (X_{g} and X_{d}, respectively) is constant throughout the disk (i.e. there are no vertical or radial variations in the mass ratios), the surface density of gas in the disk atmosphere is

$$\Sigma_{\mathrm{g}}(R) = X_{\mathrm{g}}\Sigma(R) = \frac{X_{\mathrm{g}}}{X_{\mathrm{d}}}\Sigma_{\mathrm{d}}(R), \tag{5.32}$$

using the dust surface-density Eq. (5.31). Thus, the optical depth in the disk atmosphere along the line of sight can be given by

$$\tau(\nu, R, \phi, i) = \frac{1}{\cos(i)} \left(\kappa_d(\nu) \frac{\delta(R)}{\kappa_V} + \frac{X_g}{X_d} \frac{\delta(R)}{\kappa_V} \kappa_g(\nu, R, \phi, i) \right),$$

(5.33)

where we used Eqs. (5.30-5.32).

5.7.5 Monochromatic opacities

In LTE the monochromatic opacity of the emitting gas at frequency ν with a molecular mass of m_{CO} due to transitions between states u→l can be given by

$$\kappa_g(\nu, R, \phi, i) = \frac{1}{m_{CO} 8\pi} \frac{1}{Q(T_{atm}(R))} \left(\frac{c}{\nu_0} \right)^2 A_{ul} g_u$$

$$\times \left(\exp\left[-\frac{E_l}{k T_{atm}(R)} \right] - \exp\left[-\frac{E_u}{k T_{atm}(R)} \right] \right)$$

(5.34)

$$\times \Phi(\nu, R, \phi, i)$$

(5.35)

where ν_0 is the fundamental frequency of the transition, $Q(T_{atm}(R))$ is the partition sum at the gas temperature $T_{atm}(R)$, A_{ul} and g_u are the probability of transition (i.e the Einstein A coefficient of the given transition) and the statistical weight of the upper state, respectively, while c is the the light speed. The partition sum can be given by

$$Q(T_{atm}(R)) = \sum_i g_i \exp\left[-\frac{E_i}{k T_{atm}(R)} \right],$$

(5.36)

where g_i and E_i are the statistical weight and energy level of the ith excitation state. In Eq. (5.34) the $\Phi(\nu, R, \phi, i)$ is the local intrinsic line profile originating by the natural thermal and the local turbulent broadening acting together. If the pressure of gas is negligible, the intrinsic line profile can be represented by a normalized Gauss function

$$\Phi(\nu, R, \phi, i) = \frac{1}{\sigma(R)\sqrt{\pi}} \exp\left[-\left(\frac{\nu - \nu_0 + \Delta\nu(R, \phi, i)}{\sigma(R)} \right)^2 \right],$$

(5.37)

where $\sigma(R)$ is the line width, $\Delta\nu(R, \phi, i)$ is the line center shift due to Doppler shift caused by the apparent motion of the gas parcels along the line of sight. The line width is determined by the natural thermal broadening

$$\sigma_{therm}(R) = \frac{\nu_0}{c} \sqrt{\frac{2k T_{atm}(R)}{m_{CO}}},$$

(5.38)

and the local turbulent broadening

$$\sigma_{\text{turb}}(R) = \frac{\nu_0}{c} \chi \sqrt{\frac{\gamma k T_{\text{atm}}(R)}{m_{\text{H}}}}, \tag{5.39}$$

assuming that the speed of turbulent motions is χ times the local sound speed. In Eqs. (5.38) and (5.39) m_{CO} and m_{H} are the molecular masses of H and CO and γ is the adiabatic index of the main constituent of the gas, i.e that of hydrogen. Considering the thermal and local turbulent broadening, the resulting profile will be the convolution of the two Gaussian line profiles, i.e

$$\sigma(R) = \sqrt{\sigma_{\text{therm}}(R)^2 + \sigma_{\text{turb}}(R)^2}. \tag{5.40}$$

In a planet-free disk, in which the gas parcels are moving on circularly Keplerian orbits, the line center at ν_0 fundamental frequency shifts due to the Doppler shift is

$$\Delta\nu(R, \phi, i) = \frac{\nu_0}{c} \sqrt{\frac{GM_*}{R}} \cos(\phi) \sin(i). \tag{5.41}$$

Here we neglect that the massive planet and the host star are orbiting the common center of mass, instead the center of mass is set to the center of host star. Moreover, the influence of the gas pressure on the angular velocity of gas parcels, which causes slightly sub-Keplerian orbital velocities due to radial pressure support, is also not taken into account.

6. SPECTRAL SIGNATURES OF DISK ECCENTRICITY

This Chapter presents an edited version of the paper published in 2011 by Regály, Zs.; Sándor, Zs.; Dullemond, C. P.; Kiss, L. L.; *Spectral signatures of disk eccentricity in young binary systems I. Circumprimary case*, Astronomy & Astrophysics, Volume 528, A93.

6.1 Abstract

Context: Star formation occurs via fragmentation of molecular clouds, which means that the majority of stars born are members of binary systems. There is growing evidence that planets might form in circumprimary disks of medium-separation ($\lesssim 50\,\text{AU}$) binaries. The tidal forces caused by the secondary generally act to distort the originally circular circumprimary disk to an eccentric one. Since the disk eccentricity might play a major role in planet formation, it is of great importance to understand how it evolves.

Aims: We investigate disk eccentricity evolution to reveal its dependence on the physical parameters of the binary system and the protoplanetary disk. To infer the disk eccentricity from high-resolution near-IR spectroscopy, we calculate the fundamental band ($4.7\,\mu\text{m}$) emission lines of the CO molecule emerging from the atmosphere of the eccentric disk.

Methods: We model circumprimary disk evolution under the gravitational perturbation of the orbiting secondary using a 2D grid-based hydrodynamical code, assuming α-type viscosity. The hydrodynamical results are combined with our semianalytical spectral code to calculate the CO molecular line profiles. Our thermal disk model is based on the double-layer disk model approximation. We assume LTE and canonical dust and gas properties for the circumprimary disk.

results: We find that the orbital velocity distribution of the gas parcels differs significantly from the circular Keplerian fashion. The line profiles are double-peaked and asymmetric in shape. The magnitude of asymmetry is insensitive to the binary mass ratio, the magnitude of viscosity (α), and

the disk mass. In contrast, the disk eccentricity, thus the magnitude of the line profile asymmetry, is influenced significantly by the binary eccentricity and the disk geometrical thickness.

Conclusions: We demonstrate that the disk eccentricity profile in the planet-forming region can be determined by fitting the high-resolution CO line profile asymmetry using a simple 2D spectral model that accounts for the velocity distortions caused by the disk eccentricity. Thus, with our novel approach the disk eccentricity can be inferred from high-resolution near-IR spectroscopy data acquired prior to the era of high angular resolution optical (ELT) or radio (ALMA, E-VLA) direct-imaging. By determining the disk eccentricity in medium-separation young binaries, we might be able to constrain the planet formation theories.

6.2 Introduction

Star formation occurs via fragmentation of molecular clouds causing about 60% of stars to be born as a member of a binary system (Duquennoy & Mayor 1991). Large initial specific angular momentum results in circumbinary disk formation around the protobinary, while circumstellar disks (a circumprimary and a circumsecondary) are formed around the protostars for lower initial specific angular momentum (Bate & Bonnell 1997). Bonavita & Desidera (2007) demonstrated that the overall frequency of giant planets in binaries and single stars does not statistically differ among planets discovered by radial velocity surveys. On the basis of a comprehensive survey for companions of 454 nearby Sun-like stars, Raghavan et al. (2010) revealed that both single and multiple stars are equally likely to harbor planets.

Most of the planet-bearing binaries have large separations where the planet formation might be unaltered by the companion's gravitational perturbation. However, stellar multiplicity might play a major role in planet formation in medium-separation ($\lesssim 50\,\mathrm{AU}$) binary systems. Based on Doppler surveys, Eggenberger & Udry (2010) showed that about 17% of circumstellar exoplanets are associated with binaries. Among this, five circumstellar exoplanets are known to date in $\lesssim 50\,\mathrm{AU}$ separation binary system (Queloz et al. 2000; Hatzes et al. 2003; Zucker et al. 2004; Lagrange et al. 2006; Chauvin et al. 2006; Correia et al. 2008). Two exceptional cases are also known, HW Virginis (Lee et al. 2009) and CM Draconis (Deeg et al. 2008), in which planets have been detected in circumbinary orbits. Thus, planet formation theories, such as core-accretion (Bodenheimer & Pollack 1986; Pollack et al. 1996) or gravitational instability (Boss 2001), must be able to explain the formation of planets in both circumprimary and circumbinary disk environments.

The circumprimary disk is tidally truncated at $0.35 - 0.5$ times the binary separation, depending on the binary mass ratio, binary eccentricity, and magnitude of the disk viscosity (Artymowicz & Lubow 1994). Owing to the angular momentum transfer between the disk and the companion (Papaloizou & Pringle 1977), the disk is truncated, resulting in a greatly reduced disk lifetime being available for planets to form in $\lesssim 50$ AU binaries (Cieza et al. 2009) that is a severe problem for core-accretion scenario. In contrast, the formation of gas giant planets by the relatively rapid-action of the gravitational instability might be induced by the secondary-generated shock waves if the gas cooling time is short. Nevertheless, the disk viscosity can heat the disk sufficiently to suppress the formation of clumps (Nelson 2000), but with small viscosity, gravitationally unstable clumps can still form (Boss 2006).

The disk gas feels the companion's periodic perturbation leading to strong interaction at the location of the Lindblad resonances. Waves launched at Lindblad resonances carry energy and angular momentum from the binary. The disk experiences changes in its angular momentum where the waves dampen, resulting in the development of an eccentric disk (Lubow 1991a). Several mechanism that may cause wave damping have been proposed, e.g. shocks that could be effective in colder disks, or turbulent disk viscosity acting as a dissipation source and radiative damping. Both SPH (Artymowicz & Lubow 1994) and grid-based (Kley et al. 2008) hydrodynamical simulations have confirmed the eccentricity development in binaries assuming spatially constant viscosity for the gas as a source of the wave damping. Since the orbit of bodies (dust particles or pebbles) is perturbed not only by the periodic gravitational potential of the binary but the gas drag as well, the development of disk eccentricity might influence the core-accretion processes.

The maximum size of the building blocks of planetesimals is affected by the impact velocity of sub-micron-sized grains in the dust coagulation process. According to Zsom et al. (2010), the aggregate sizes are lower in eccentric disks than in axisymmetric disk environments owing to the increase in the relative velocity between the dust particles. We note, however, that an investigation of the SED slopes of medium-separation T Tauri binaries by Pascucci et al. (2008) showed that the extent of dust processing in the disk surface layer and the degree of dust settling in binary disks do not differ significantly from those in disks around single stars.

The planetesimal accretion phase, leading to between km-sized planetesimals and several 100 km-sized planetary embryos, should proceed in an environment where the mutual encounter velocities of planetesimals are on the order of planetesimal surface escape velocities. In this environment, the planetary embryos could grow quickly by runaway growth mode (Wetherill & Stewart 1989). Since the runaway growth mode is sensitive to the encounter velocities, for increased

encounter velocities, e.g., due to the stirring up of the planetesimal swarm, runaway growth might be stopped. Thébault et al. (2006) showed that the impact velocity of different-sized planetesimals tends to increase owing to the interaction between the companion and the gaseous friction in binaries with separations of $10 \leq a_{\text{bin}} \leq 50 \, \text{AU}$. Paardekooper et al. (2008) found that the planetesimal encounter velocities with different sizes could be larger by an order of magnitude in eccentric disks than in the axisymmetric case. Consequently, planetesimal accretion might be inhibited in highly eccentric disks.

In accretion disks, the presence of the double-peaked emission lines are the natural consequence of the gas parcels moving in Keplerian orbits around the host star. Huang (1972) and Smak (1981) presented this in connection with the emission lines of Be and cataclysmic variable stars. Horne & Marsh (1986) investigated the emerging line profiles in accretion disks. Since the Keplerian angular velocity of gas parcels is highly supersonic in accretion disks, the Doppler shift of the line emitted by individual gas parcels exceeds the local line-profile width. Summing up the line profiles emitted by individual rings of gas parcels, and taking into account the radial dependence of the line surface brightness, the result is the well-known double-peaked broad symmetric line shapes (Horne & Marsh 1986). Azimuthal asymmetries in disk surface brightness (e.g. density perturbations in optically thin lines, or supersonic anisotropic turbulence in saturated lines), will break the line profile symmetry (Horne 1995). Gas parcels orbiting non-circularly (i.e., in elliptic orbit) might also produce the asymmetric line profiles presented by Foulkes et al. (2004) for cataclysmic variables, and Regály et al., (2010) for protoplanetary disks.

In this paper, we investigate the eccentricity evolution of a circumprimary disk in a young binary system. We perform an extensive parameter study to reveal the dependence of the disk eccentricity on several parameters, such as binary and disk geometry, and gas viscosity. The hydrodynamical simulations were done in 2D by a grid-based parallel hydrodynamic code FARGO (Masset 2000). We model the circumprimary disk evolution under the gravitational perturbation of the orbiting secondary assuming α-type viscosity (Shakura & Sunyaev 1973). We calculate the fundamental band ($4.7 \, \mu\text{m}$) ro-vibrational emission lines of the molecule $^{12}\text{C}^{16}\text{O}$ emerging from the disk atmosphere, providing a tool to determine the disk eccentricity from high-resolution near-IR spectroscopy by means of line profile distortions. Our thermal disk model is based on the double-layer disk model of Chiang & Goldreich (1997). Since the velocity distribution of the gas parcels show supersonic deviations from the circular Keplerian one, owing to the eccentric disk state, asymmetric molecular line profiles emerge from the optically thin disk atmosphere.

This Chapter is structured as follows. In the next section, we present our hydrodynamical sim-

ulation modeling of the evolution in general of disk eccentricity. The calculation of fundamental-band CO ro-vibrational emission lines emerging from an eccentric circumprimary disk are presented in Sect. 6.4. In Sect. 6.5, we present an extensive parameter study to investigate the evolution of the disk eccentricity for a wide range of binary and disk parameters. Section 6.6 deals with the comparison of our results to other recent simulations, and the observability of eccentric signatures. The Chapter closes with conclusions.

6.3 Hydrodynamic disk model

In our simulations, we use an isothermal version of FARGO, a publicly available parallel 2D hydrodynamical code (Masset 2000). We apply α-type disk viscosity (Shakura & Sunyaev 1973), assuming $\alpha = 0.02$ in our model. We adopt dimensionless units for which the unit of length is the orbital separation of the binary (a_{bin}), and the unit of mass is the mass of central star. The unit of time t_0 is obtained from the orbital period of the binary, thus $t_0 = 1/2\pi$, setting the gravitational constant G to unity.

The computational domain is covered by 270 radial and 500 azimuthal grid cells, and the origin of the grid is on the primary star. The radial spacing is logarithmic, while the azimuthal spacing is equidistant. The disk's inner and outer boundary is at $0.01 a_{\mathrm{bin}}$ and $1.5 a_{\mathrm{bin}}$, respectively. The initial orbital separation of the binary is $a_{\mathrm{bin}} = 1$, thus the computational domain contains the orbit and the Roche lobe of the system. Open boundary conditions are assumed at the inner and outer boundaries, i.e the disk material is allowed to flow out from the computational domain, but no inflow is allowed. The secondary is allowed to accrete the material flowing through its Hill sphere with the same rate as described in Kley (1999). The secondary feels the gravitational pull of the disk, thus its orbital elements can change.

We use a rotating frame that co-rotates with the binary. The binary orbit is initially circular ($e_{\mathrm{bin}} = 0$). The initial surface density profile follows a power-law distribution $\Sigma(R) = \Sigma_0 R^{-0.5}$. We use the canonical constant aspect ratio $h = 0.05$ disk approximation. The disk self-gravity is neglected because the Toomre parameter $Q(R) = h M_* / \pi R^2 \Sigma(R) \gg 1$ for our model (Toomre 1964).

To model an existing binary system V807 Tau with a sole circumprimary disk (Hartigan & Kenyon 2003), the secondary-to-primary mass ratio is set to 0.3. The binary eccentricity is neglected in this particular calculation. The distance unit is taken to be $40\,\mathrm{AU}$ accordingly to the measured separation (Pascucci et al. 2008). The initial disk mass is set to $2 \times 10^{-3}\,M_\odot$ by the

choice of $\Sigma = 17.2\,\mathrm{g/cm^2}$ at 1 AU. To prevent numerical instabilities at low density regions, an artificial density floor is applied: whenever the disk surface density is below a certain limit, it is reset to that limit, which is 10^{-12} in dimensionless units.

Initially, we placed the secondary on a circular orbit into the unperturbed disk, in which the surface density had been artificially damped. With this damping, the secondary orbits in a practically gas-free environment. We use a Gaussian damping, i.e., the density is damped as

$$\Sigma(R,\phi)_{\mathrm{trunc}} = \Sigma(R,\phi) \left(\Sigma_{\mathrm{s}} + (1 - \Sigma_{\mathrm{s}}) \exp \left[- \left(\frac{R - R_{\mathrm{tr}}}{\sigma_{\mathrm{tr}}} \right)^2 \right] \right), \tag{6.1}$$

where Σ_{s} is the surface density at the outer edge of the damped region, R_{tr} is the radius where the density damping begins, and σ_{tr} is the radial extent of the damped region. The damping parameters are $R_{\mathrm{tr}} = 0.6$, $\sigma_{\mathrm{tr}} = 0.2$, and $\Sigma_{\mathrm{s}} = 10^{-8}$.

6.3.1 Formation of eccentric disk

We present our results on the disk evolution through a couple of hundred orbits of the binary. The evolution of the 2D surface density is shown in Fig. 6.1, and the azimuthally averaged density profile in Fig. 6.2 (panel a).

After the first couple of binary orbits, a double spiral waves appear. In general, the disk remains approximately axisymmetric until the ~ 150th binary orbit (Fig. 6.1). Comparing the initial and the evolved density profiles in the 50th and 150th orbits, the profile becomes less steep, while the density at the disk inner edge increases as the disk material is piled up by the secondary (Fig. 6.2, panel a). The density profile is steepened during the subsequent orbits because of the angular momentum removal by the secondary.

The disk eccentricity is calculated at each individual grid cells using the radial and azimuthal velocity components applying the equations presented in Regály et al. (2010). To obtain the radial disk-eccentricity profiles, the eccentricity distribution is azimuthally averaged within the disk radius, which is defined as the radius containing 90% of the mass. From the 150th orbit, the disk eccentricity rapidly increases (see the evolution of disk eccentricity in Fig. 6.2 panel b). It is expedient to radially average the disk-eccentricity profiles at each secondary orbit, in which case we can assign a single value to each eccentric state of the disk. Since the disk radius and eccentricity profile (Fig. 6.2, panel d) slightly change as the disk and the secondary mutual positions vary, their values as a function of time are "noisy". To remove this "noise", the radius
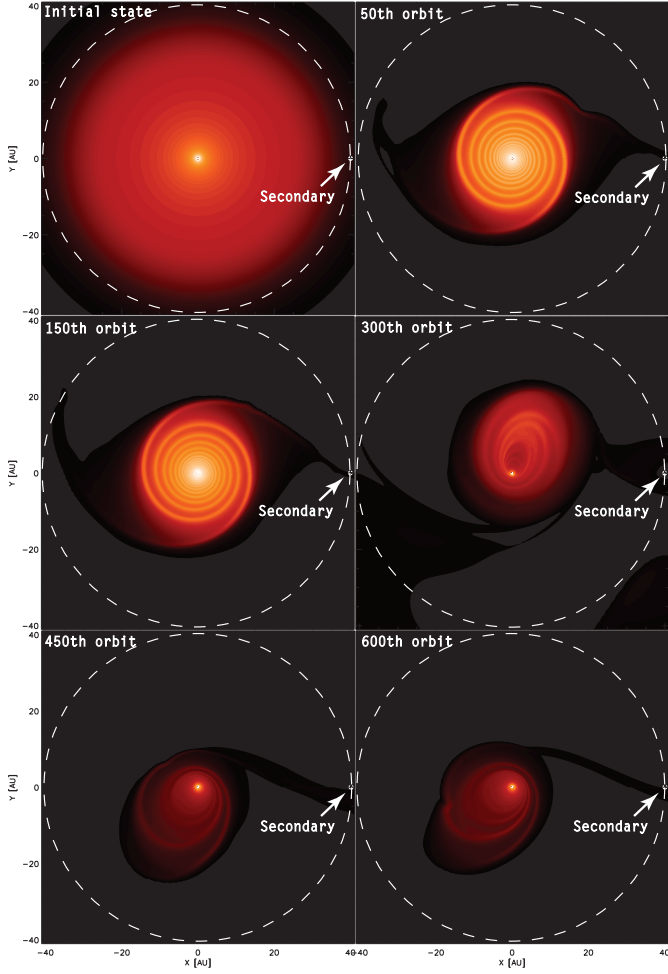
FIGURE 6.1: Evolution of the disk surface density shown in six snapshots taken at 0, 50, 150, 300, 450, and 600th orbits of the binary. The secondary's counter-clockwise orbit is shown with a white dashed circle.
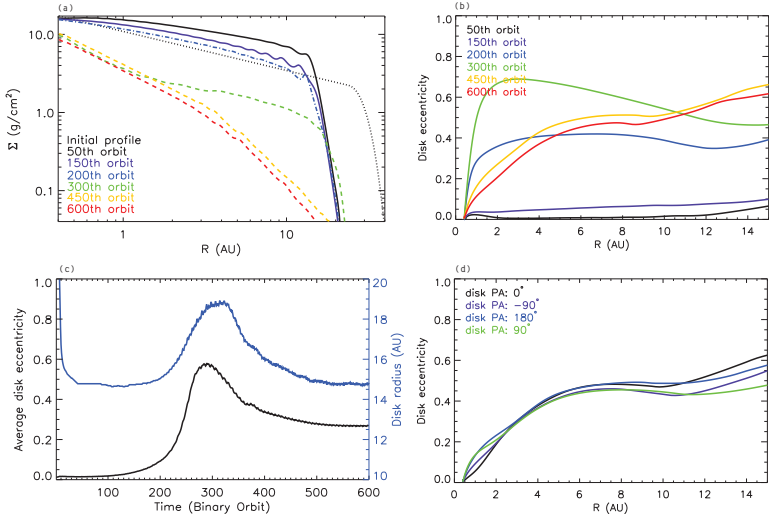
FIGURE 6.2: *Panel a*: evolution of the azimuthally averaged density profile shown in six epochs calculated at 0, 50, 150, 300, 450, and 600th binary orbits. The initial density profile is shown with black dotted curve. *Panel b*: evolution of the azimuthally averaged eccentricity shown in five curves calculated at 50, 150, 300, 450, and 600th binary orbits. Only the 0-20 AU region is shown in the plot, as the disk is significantly truncated beyond 20 AU. *Panel c*: evolution of the disk radius (with blue), and the averaged disk eccentricity (with black). The curves are smoothed to remove "noise" (see text for explanation). *Panel d*: variation in the disk eccentricity during a full disk precession period. The disk position angle (PA) is measured relative to the position of the orbiting secondary.

92

and eccentricity evolution curves calculated at each secondary orbit are smoothed (Fig. 6.2, panel c).

At the beginning of the simulation, the disk is truncated by the secondary to $\sim 15\,\mathrm{AU}$. From the 200th binary orbit, the disk begins to expand slightly, and the disk eccentricity starts to grow. The disk eccentricity reaches its overall maximum during the ~ 300th binary orbit, and begins to decline during subsequent orbits. The disk reaches a quasi-steady state by the ~ 450th binary orbit, in which neither the eccentricity nor the disk radius evolves further. By this time, the disk radius is stabilized at $\sim 15\,\mathrm{AU}$. Noteworthy is the correlation of the disk eccentricity and radius evolution.

Regarding the orbital parameters of the secondary, we found that they are not changed significantly. Until the 600th orbit, the secondary migrates slightly outward to 0.3% of its original distance because it gains angular momentum from the disk, while the binary eccentricity remains close to zero.

When the secondary passes close to the outer edge of the elliptic disk, a tidal tail develops through which the disk material increases the mass of the secondary, but by a negligible amount. The evolution of a tidal tail during the 300th orbit is shown in Fig. 6.3. The tidal tail persists for only a quarter of an orbit, and reappears in each binary revolution.

When the disk becomes elliptic, the velocity field departs significantly from the circular Keplerian one. The disk is non-axisymmetric, not only in density, but in velocity field too. The line-of-sight velocity component of the gas parcels calculated during the 600th binary orbit is shown in Fig. 6.4, assuming that the disk is seen to be inclined by $60°$. Gas parcels that are at the same distance to the primary star (shown with white dotted circles), hence at the same temperature, have different azimuthal velocities. Since the velocity asymmetry at a given radius can be larger than the local sound speed $(2 - 3\,\mathrm{km\,s^{-1}})$ for $R \leq 3\,\mathrm{AU}$, the Doppler shift of the lines emitted by a gas parcel exceeds the local line width. Consequently, the shape of emission lines emerging from the eccentric disk might be distorted (Horne & Marsh 1986). Therefore, we expect the molecular line profiles formed in an eccentric circumprimary disk of a young binary system to be asymmetric (see, e.g., Statler (2001)).

The elliptic disk precesses retrogradely with respect to the secondary's orbit, as if it were a rigid body. The precession period is ~ 6.6 orbital periods of the binary. As a consequence, the line profiles are expected to exhibit long-period variations.

The azimuthally averaged disk eccentricities calculated for four different disk position angles (PA) measured with respect to the secondary are shown in Fig. 6.2, panel d. The eccentricity of
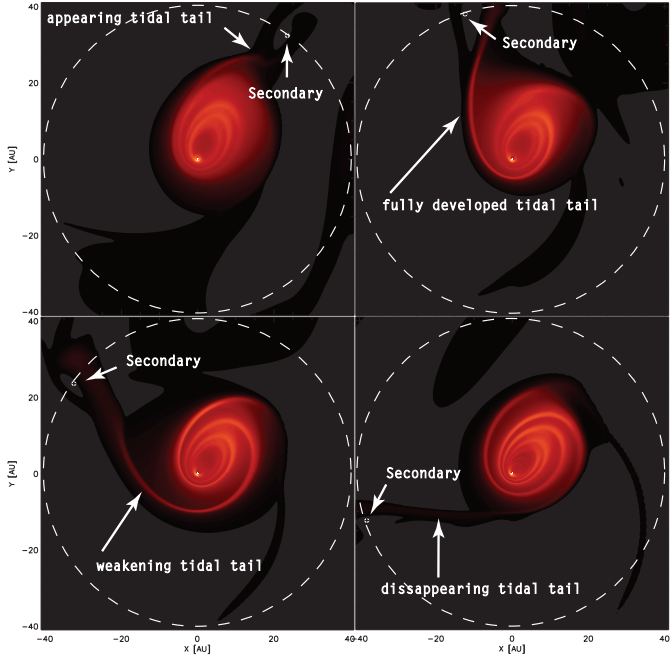
FIGURE 6.3: Development of the tidal tail appeared after the secondary passes closest to the disk apastron edge during the 300th orbit. The secondary's counter-clockwise orbit is shown with a white dashed circle. The density enhancement can reach two orders of magnitude in the tidal tail.
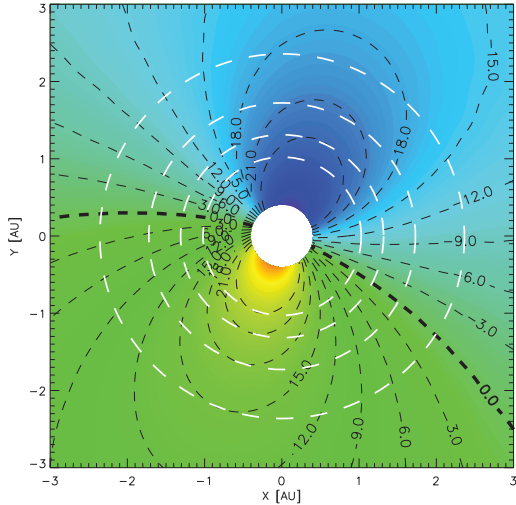
FIGURE 6.4: Line-of-sight velocity component of the gas parcels in the 600th orbit, assuming a $i = 60°$ disk inclination. The unit of contour lines is $km\,s^{-1}$. The reddish and bluish colors represent the receding and approaching part of the disk, respectively. Gas parcels at the same distance to the primary (*white dashed lines*) on the approaching side have significantly larger apparent velocities than those on the receding side.

the inner disk ($R \leq 3\,\mathrm{AU}$) shows periodic variation. The disk eccentricity reaches its maximum, when the disk is aligned with the binary at $\mathrm{PA} = 180°$, i.e., when the disk periastron edge is the closest to the secondary. When the disk apastron edge is closest to the binary, i.e., for $\mathrm{PA} = 0°$, the disk eccentricity reaches its overall minimum. Between these states, when the disk semimajor axis is perpendicular to the binary axis, the inner-disk average eccentricity has an intermediate value. As a consequence, the line profiles are also expected to display small periodic variations on the timescale of the binary orbit.

6.4 Fundamental band ro-vibrational CO line profiles

The spectral lines emerging from an axisymmetric disk with disk parcels on circular Keplerian orbits, have symmetric double-peaked shapes (Horne & Marsh 1986). Analyzing the hydrodynamical results, it is reasonable to expect that the optically thin atmosphere of an eccentric disk produces non-symmetric molecular lines as the disk parcels are moving on non-circular orbits. We note that several single T Tauri stars display centrally peaked symmetric CO line profiles. This might be attributed to an extended CO excitation by stellar UV photons (see e.g., Brittain et al. (2007)), in which case the line profiles are also expected to be asymmetric. In the following, we do not take into account the stellar UV flux, thus our investigation concentrates on systems that would produce double-peaked profiles.

To calculate the strengths of the CO ro-vibrational emission lines, we combine the hydrodynamic results with our recently developed semi-analytical line spectral model (Regály et al., 2010). In our approach, the thermal disk model is based on the double-layer disk approximation of Chiang & Goldreich (1997), in which the CO emission lines are formed in the superheated optically thin disk atmosphere above the cooler optically thick disk interior. The disk inner edge, where the simple double-layer assumption cannot be applied, is assumed to be a perfectly vertical wall. According to the stellar evolutionary tracks (Siess et al. 2000), the luminosity of a $0.3\,M_\odot$ pre-main-sequence star is negligible compared to that of an $1\,M_\odot$ primary ($L_{0.3M_\odot}/L_{1M_\odot} \simeq 0.2$), hence we neglect the irradiation from the secondary. We therefore assumed that the disk is heated solely by the stellar irradiation of the primary. We note that the accretion rate measured in our hydrodynamical simulations is below $2.5 \times 10^{-11}\,M_\odot \mathrm{yr}^{-1}$, thus viscous heating is negligible compared to the stellar irradiation. As a consequence, the disk atmosphere is hotter than the disk interior, where a superheated atmosphere is formed producing emission molecular spectra. We assume that the primary is similar to the one in the system V807 Tau. On the basis of the published spectral type of V807 Tau, i.e., K7 (Hartigan et al. 1994) and assuming that the primary is $\sim 2.5\,\mathrm{Myr}$ old, its radius and effective surface temperature are taken to be $R_* = 1.83\,R_\odot$, and $T_* = 4266\,\mathrm{K}$, respectively, using a publicly available pre-main-sequence database (Siess et al. 2000). It is assumed that the dust consists of pure silicates with a $0.1\,\mu\mathrm{m}$ grain size (Draine & Lee 1984). The mass absorption coefficient of the dust is taken to be $\kappa_\mathrm{V}^\mathrm{dust} = 2320\,\mathrm{cm}^2/\mathrm{g}$ at visual wavelengths and $\kappa_{4.7\mu m}^\mathrm{dust} = 200\,\mathrm{cm}^2/\mathrm{g}$ at $4.7\mu m$. The dust-to-gas and CO-to-gas mass ratios are assumed to be constant throughout the disk and being assumed to be $X_\mathrm{d} = 10^{-2}$ and $X_\mathrm{g} = 4 \times 10^{-4}$, respectively.

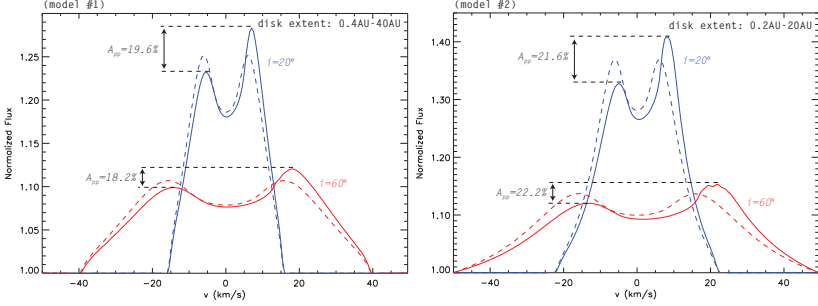Taking into account our dust opacity assumptions, the disk is optically thick within $3\,\mathrm{AU}$

FIGURE 6.5: $V = 1 \to 0$ P10 fundamental band CO ro-vibrational line profiles for circular Keplerian (*dashed lines*) and eccentric disk (*solid lines*) in the 600th binary orbit. The disk extensions were 0.4 AU-40 AU and 0.2 AU-20 AU for panel *left* and *right*, respectively. The line profiles for inclinations $i = 60°$ and $i = 20°$ are shown with blue and red colors, respectively. The magnitude of asymmetry is larger for higher inclination angles. Although the line fluxes normalized to the continuum are clearly different, the magnitude of asymmetry remains the same for model #1 and #2.

where the CO ro-vibrational fundamental band is excited, regardless of the significant depletion that occurs by the time the disk eccentricity has developed (see Fig. 6.2, panel a). The continuum optical depth normal to the disk midplane at 4.7μm is $\tau_{4.7\mu m}(R) = \Sigma(R)X_d\kappa_{4.7\mu m}^{dust}$, which drops below 1 (for one side of the disk) if the disk surface density is $\Sigma_d \leq 0.5 g/cm^2$. In our simulation, the surface density is $\Sigma \geq 1 g/cm^2$ within 3 AU (see Fig. 6.2, panel c), therefore the disk interior is optically thick at both 4.7 μm and optical wavelengths. However, the density drops below this critical value beyond 3 AU (see Fig. 6.2 panel a), thus the disk is no longer optically thick in the outer regions.[1] Nevertheless, beyond 2-3 AU the CO ro-vibrational fundamental band is not excited by the primary irradiation, and beyond 5 AU the disk interior has no contribution to the 4.7μm continuum.

---

[1]Note, however, that the density can be arbitrarily scaled up resulting in an optically thick disk, as the hydrodynamical simulations are independent of the assumed disk mass as long as the change in binary orbital elements are small. More details are given in the Discussion.

TABLE 6.1: CO line profile asymmetries for model #1 and #2

Model	i	I_b^a	I_r^b	A_{pp}^c
#1	$20°$	1.23	1.28	19.6%
	$60°$	1.10	1.12	18.2%
#2	$20°$	1.33	1.41	21.6%
	$60°$	1.12	1.15	22.2%

[a] Normalized intensity maximum at the red peak

[b] Normalized intensity maximum at the blue peak

[c] Peak-to-peak line profile asymmetry

6.4.1 Asymmetric line profiles

In advance, here we give a short summary of the physical background responsible for the shaping of molecular line profiles emerging in dynamically distorted disk atmospheres. The local line profile emerging from the disk atmosphere from a given point R, ϕ in cylindrical coordinates depends on the local Doppler shift. The fundamental line center ν_0 shifts because of the apparent motion of the gas parcels along the line-of-sight. The shift is significant compared to the line width if the apparent velocity of the gas parcels exceeds the local sound speed.[2] To calculate the Doppler shifts for circularly Keplerian disks and an eccentric disk, we used Eq. (E.8) and Eq. (4) of Regály et al. (2010), respectively. In the latter case the velocity components of the gas parcels ($u_R(R, \phi)$ and $u_\phi(R, \phi)$) were provided by the hydrodynamical simulations.

Figure 6.5 shows the line profiles emerging from an unperturbed (dashed line) and an eccentric disk (solid line), assuming $20°$ and $60°$ disk inclination angles. We performed the synthetic spectral calculations in two disk models with different disk sizes, using the same hydrodynamical output of the 600th binary orbit. The computational domain of the synthetic spectral calculation was $0.4 \, \text{AU} \leq R \leq 40 \, \text{AU}$ and $0.2 \, \text{AU} \leq R \leq 20 \, \text{AU}$ for model #1 and model #2, where the binary separation is $40 \, \text{AU}$ and $20 \, \text{AU}$, respectively (left and right panels of Fig. 6.5). In this way, the disk edge is at 0.4 AU and 0.2 AU for models #1 and #2, respectively. As the CO fundamental band is excited out to 2-3 AU (Najita et al. 2007), the disk material beyond 3 AU does not contribute to the CO line emission in our model. However, material beyond this radii out to $\sim 5 \, \text{AU}$

---

[2]We neglect the effect of turbulent line broadening, thus the intrinsic line width is determined by the thermal broadening alone.

TABLE 6.2: Flux ratios of models #1 and #2

Model	i	$F_{\mathrm{dc}}/F_*^{\mathrm{a}}$	$F_{\mathrm{de}}/F_*^{\mathrm{b}}$	$F_{\mathrm{dc+de}}/F_*^{\mathrm{c}}$
#1	20°	5.13	2.78	7.92
	60°	2.88	2.78	5.66
#2	20°	4.05	1.75	5.8
	60°	2.45	1.75	4.2

[a] Disk interior to stellar flux ratio

[b] Disk edge to stellar flux ratio

[c] Disk interior + disk edge to stellar flux ratio

must be considered for the line-over-continuum calculation, since the dust in the superheated disk atmosphere contributes considerably to the continuum at $4.7\mu m$.

It can be clearly seen that the line profiles formed in an eccentric disk (solid lines) are asymmetric, assuming that the semimajor axis of the elliptic disk is perpendicular to or at least not aligned with the line-of-sight. The line-to-continuum is stronger in model #2 than in model #1, owing to the disk continuum (disk + disk edge) of model #1 exceeding that of model #2 (see details of the calculated fluxes in Table 6.2) and the additional hot CO emission orbiting between 0.2 AU and 0.4 AU in model #2. The depressed disk continuum for model #2 may be due to: (1) the rim flux being smaller for a rim closer to the star, since the disk rim flux is $F_{\mathrm{rim}} \sim T_{\mathrm{edge}}^4 R_{\mathrm{edge}}^2$, where the $T_{\mathrm{edge}} \sim R^{-2/5}$ (see, e.g., Appendix A of Regály et al. (2010)), resulting in $F_{\mathrm{rim}} \sim R^{2/5}$; (2) the radial extension of the region close to the rim where the disk interior is irradiated directly by the rim (see, e.g. Appendix B of Regály et al. (2010)) is larger for model #1, resulting in a stronger continuum for model #1 than model #2.

The profile asymmetry does not differ significantly between the two models. Calculating the peak-to-peak line profile asymmetry as $A_{\mathrm{pp}} = |I_{\mathrm{b}} - I_{\mathrm{r}}|/(0.5[I_{\mathrm{b}} + I_{\mathrm{r}}] - 1)$, where I_{r} and I_{b} are the continuum normalized line fluxes at the red and blue peaks, respectively, the asymmetry is $A_{\mathrm{pp}} \simeq 20\%$ for all models (see details in Table 6.1). After closer inspection of Fig. 6.5, the line center is clearly seen to shift toward the peak, which is in excess. The magnitude of line center shift also depends on the disk inclination angle and the disk extension. Obviously, the larger the inclination angle, the larger the line center shift. Moreover, the magnitude of the line center shift is larger in model #2 than in model #1 because of the additional emission of hot gas parcels on

closer orbits in model #2.

6.4.2   Formation and variability of line profile asymmetry

The line profile distortion in eccentric disks occurs owing to the same phenomena as for the giant planet-bearing disks presented in Regály et al. (2010). But here the *whole disk is eccentric*, which allows us to give an even simpler explanation of the origin of asymmetry. This and the consequences of disk precession are explained in this section.

To provide insight into the cause of the line profile variations, we calculated the CO line profiles during a full disk-precession period in model #1. Part of the results are shown in Fig. 6.6. The line profile asymmetry is most prominent when the disk semimajor axis is seen perpendicular to the line-of-sight (Fig. 6.6, panel a and d). In contrast, the line profile asymmetry completely vanishes when the disk semimajor axis is seen parallel to the line-of-sight (Fig. 6.6, panel c).

The formation of the asymmetry can be explained by the temperature difference of the gas parcels with the same absolute values of receding and approaching velocities. In an elliptic orbit, the Y velocity component at cylindrical coordinates (R, ϕ) can be given by

$$V_{\mathrm{Y}}(R, \phi) = V_{\mathrm{K}}(R) \frac{\cos(\phi) + e}{\sqrt{1 + e\cos(\phi)}}, \tag{6.2}$$

where e is the orbital eccentricity of the gas parcels. For simplicity, we assume that the disk eccentricity is constant with radius. Gas parcels at the opposite side of the disk (one at apastron R_{ap} and the other at periastron R_{per}), have the same absolute value of the velocity along the line-of-sight ($V_{\mathrm{Y}}(R_{\mathrm{ap}}, \phi) = -V_{\mathrm{Y}}(R_{\mathrm{per}}, \phi)$) if the equality

$$R_{\mathrm{ap}} = \frac{1 - e}{1 + e} R_{\mathrm{per}} \tag{6.3}$$

holds, using Eq. (6.2). We note that gas parcels at R_{ap} and R_{per} are not on the same orbit. Here we align the cylindrical coordinate system such that at periastron $\cos(\phi) = 1$, and at apastron $\cos(\phi) = -1$. According to Eq. (6.3), $R_{\mathrm{ap}} < R_{\mathrm{per}}$ holds because the eccentricity is given by $0 < e < 1$ for elliptic orbits. As the gas parcels at apastron and periastron are approaching and receding, they contribute to the blue and red peaks, respectively. The disk is seen by the observer as shown in the subfigure of panel a of Fig. 6.6. Setting the radii of the gas parcels that contribute to the red and blue peaks to be $R_{\mathrm{red}} \equiv R_{\mathrm{ap}}$ and $R_{\mathrm{blue}} \equiv R_{\mathrm{per}}$, respectively, we find that $R_{\mathrm{red}} < R_{\mathrm{blue}}$. The temperature of the gas parcels at apastron exceeds that at periastron owing to
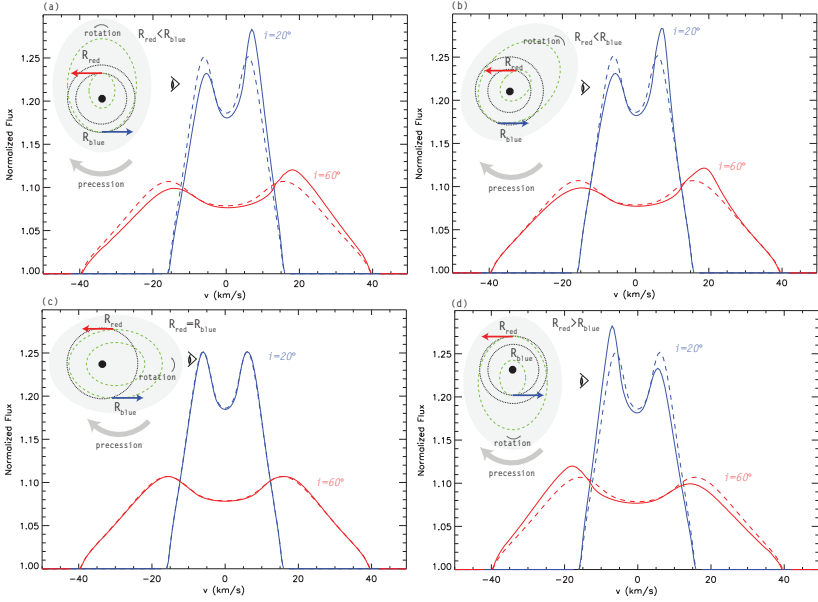
FIGURE 6.6: $V = 1 \rightarrow 0$ P10 ro-vibrational CO line-profile variations during a full precession period of eccentric disk calculated in model #1 after the 600th binary orbit. For comparison, the line profiles emerging in an unperturbed circularly Keplerian disk are shown with dashed lines. Small subfigures show the disk's apparent position with respect to the line of sight. The $i = 20°$ and $i = 60°$ inclination angles were assumed, shown in blue and red colors, respectively. The orbits of gas parcels are indicated by green dotted ellipses in the subfigures. *Panels* **a** and **d**: show that the asymmetric line profiles emerging in the disk when seen normal to its semimajor axis. *Panel* **c**: shows that the symmetric line profiles emerging in the disk when seen parallel to its semimajor axis. *Panel* **b**: shows that the line profiles with a smaller amount of asymmetry emerging from a disk with intermediate position angle.

the $T_{\mathrm{atm}}(R) \sim R^{-2/5}$ dependence of the atmospheric temperature on distance in the double-layer disk model. Thus, the gas parcels receding with speed V make a larger contribution to the red peak than the gas parcels approaching with speed $-V$ to the blue peak (Fig. 6.6, panel a).

Having precessed the disk by $45°$, the red peak remains in excess, since although the expression Eq. (6.3) does not hold, $R_{\mathrm{red}} < R_{\mathrm{blue}}$ (Fig. 6.6, panel b). Although the magnitude of peak asymmetry does not change significantly, the departure of the line profile shape from the Keplerian one is smaller in the line wings.

By the time the disk has precessed by $90°$, the distances of the gas parcels receding and approaching with the same speed are equal, thus $R_{\mathrm{red}} = R_{\mathrm{blue}}$. Obviously, their contributions to the red and blue peaks are just the same, resulting in no asymmetry in the line profile (Fig. 6.6, panel c).

The disk is seen again perpendicular to its semimajor axis in a subsequent $90°$ of disk precession (Fig. 6.6 panel d). In this phase, the gas parcels at periastron and apastron are now receding and approaching, respectively. In this case, $R_{\mathrm{red}} \equiv R_{\mathrm{per}}$ and $R_{\mathrm{blue}} \equiv R_{\mathrm{ap}}$, thus the distance relation of the receding and approaching gas parcels is found to be $R_{\mathrm{blue}} < R_{\mathrm{red}}$ using Eq. (6.3). The level of red-blue peak asymmetry is nearly the same for disks seen at antiparallel position angles perpendicular to the semimajor axis (Fig. 6.6, panel a and d). Although the disk eccentricity varies during the disk precession (Fig. 6.2, panel d), this can be explained by its amplitude being small in the regions $R < 2 - 3\,\mathrm{AU}$ where the CO is excited.

To illustrate the line profile variations during 200 binary orbits, we present trailed spectra of CO in Fig. 6.7. The periodic change in the red-blue peak asymmetry caused by the disk precession is clearly visible. In addition, smaller variations in the line wings with periods ~ 0.7 times the binary orbital period are also visible. This can be explained by small-magnitude disk eccentricity variations owing to its dependence on the apparent position angle of the secondary with respect to the disk semimajor axis. These variations are similar to those that occur in superhump binaries, where an additional period is present as a beat period between the precessing disk and the binary orbit. However, in the superhump case, the period is slightly longer than the binary period because of the prograde disk precession (Goodchild & Ogilvie 2006). In our case, the period is shorter than the binary orbital period because the disk precession is retrograde.

To summarize, the line profile becomes asymmetric in the quasi-steady eccentric disk state. The period of line profile asymmetry is equal to that of the disk precession. Two asymmetric phases alternate with each other, and there are two symmetric phases amongst them. However, the variation in the red-blue peak asymmetry is unlikely to be observed within a decade because of

the long precession period, which is $\sim 250\,\mathrm{yr}$ for a 40 AU separation binary. Nevertheless, as the line wings are also subject to variations of period ~ 0.7 times that of the binary period, it might be detectable for $\sim 10\,\mathrm{AU}$ separation binaries with $\sim 2\,M_\odot$ primaries.

6.5 Parameter study

To investigate under which conditions the disk will develop eccentricity, we performed an extensive hydrodynamical study. The following parameters were varied within physically reasonable intervals: the binary mass ratio q, the viscosity parameter α, the binary eccentricity e_{bin}, the disk aspect ratio h, the flaring index γ, and the disk-to-secondary mass ratio $q_{\mathrm{disk/sec}}$. In addition, we investigated the effects of the open outflow and the rigid boundary conditions at the inner boundary of the disk.

To speed up our calculations, we assumed a larger disk inner radius ($R_{\mathrm{in}} = 0.05a_{\mathrm{bin}}$) in the parameter study than used previously ($R_{\mathrm{in}} = 0.01a_{\mathrm{bin}}$) in Sect. 2. We ran several models with $0.01a_{\mathrm{bin}} \leq R_{\mathrm{in}} \leq 0.05a_{\mathrm{bin}}$. The results demonstrated that neither the disk eccentricity profile nor the evolution of the average disk eccentricity depends significantly on the choice of the disk inner radius. The hydrodynamical simulations performed in this parameter study cannot be used to calculate the strength of the CO emission lines, because when assuming that the distance unit is either 40 AU or 20 AU, the hot emitting inner part of the disk is not involved in the calculation. This does not prevent the evolution of the eccentric quasi-steady state of the disk being able to be studied and described in detail.

6.5.1 Results for the disk eccentricity and radius

The radial extension of a circumprimary disk is determined by the tidal truncation, whose efficiency depends on the binary mass ratio and possibly other physical parameters of the disk itself such as the magnitude of the disk viscosity. To characterize the time evolution of the disk size, we defined the disk radius as the distance measured from the primary star containing 90% of the disk material. The disk eccentricity is calculated at each individual grid cells as mentioned in Sect. 2.1. To characterize the disk eccentric state, the eccentricity distribution was azimuthally and within the disk radius radially averaged. Since the 3:1 Lindblad resonance point – which is responsible for the eccentricity excitation (Lubow 1991a) – is close to the outer disk edge, the disk eccentricity is strongly connected to the disk radius evolution. Therefore, it is crucial to describe
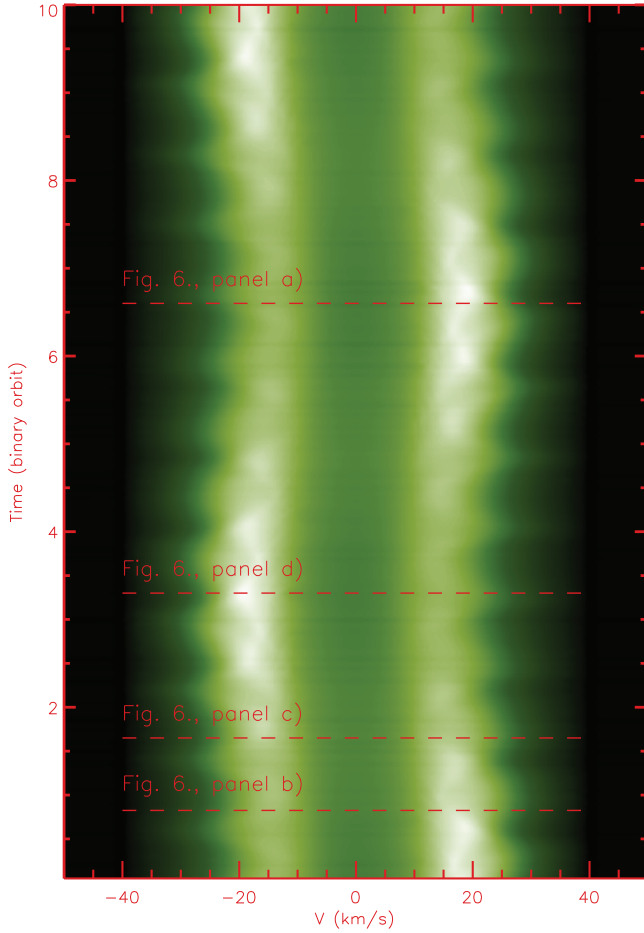
FIGURE 6.7: Trailed spectra of $V = 1 \rightarrow 0$ P10 ro-vibrational CO line profile at $4.7\mu m$ emerging from the quasi-steady eccentric disk state in model #1. The line profiles were calculated with cadence of 1/20 binary orbit, and the trailed spectra covers 10 binary orbits. Epochs of the line profiles shown in Fig. 6.6 are marked with dashed lines.
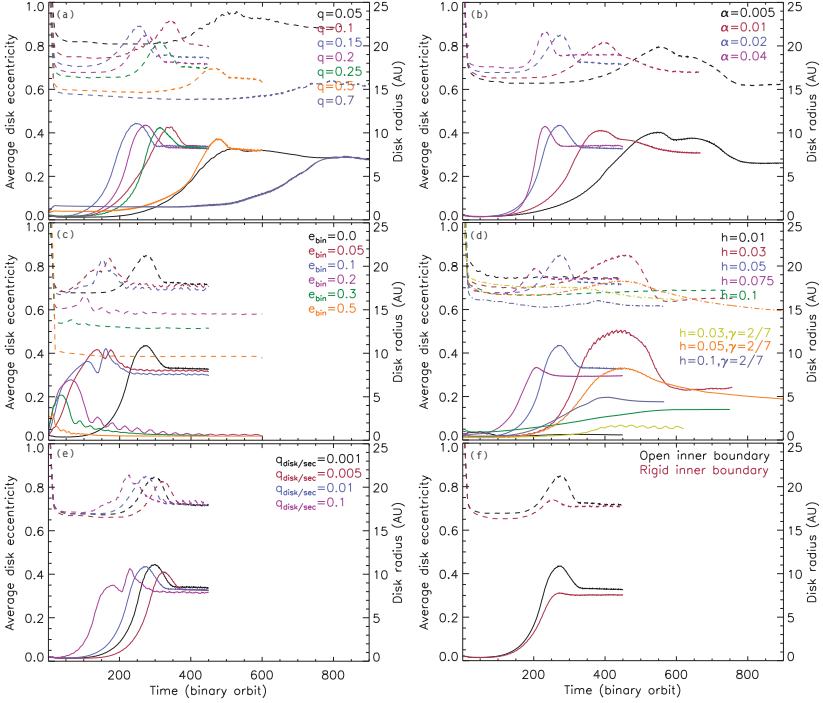
FIGURE 6.8: Evolution of the disk radii (dashed curves) and the average disk eccentricities (solid curves) for different models in our parameter study: *Panel* **a**) models with binary mass ratios $0.05 \leq q \leq 0.7$, viscosity parameter $\alpha = 0.02$, and aspect ratio $h = 0.05$; *Panel* **b**) models with $0.005 \leq \alpha \leq 0.4$, $q = 0.2$, and $h = 0.05$; *Panel* **c**) models with binary orbital eccentricity $0.0 \leq e_{\text{bin}} \leq 0.5$, $q = 0.2$, $\alpha = 0.02$, and $h = 0.05$; *Panel* **d**) models with $0.01 \leq h \leq 0.1$, $q = 0.2$, and $\alpha = 0.02$; flaring disk models with $\gamma = 2/7$ are shown with dot-dashed curves; *Panel* **e**) models with disk mass $0.001 \leq q_{\text{disk/sec}} \leq 0.1$, $q = 0.2$, $\alpha = 0.02$, and $h = 0.05$; *Panel* **f**) models with open outflow and rigid boundary conditions assuming $q = 0.2$, $\alpha = 0.02$, and $h = 0.05$.

the development of the disk radius and the average disk eccentricity in parallel.

The evolution of the average disk eccentricity tends to follow the evolution of the disk radius. The disk is tidally truncated after a few tens of binary orbits at a radius $R \simeq 0.35 - 0.54 a_{\mathrm{bin}}$ for all disk models. Later on, the disk increases in size, then shrinks, and finally approaches a size of $R \simeq 0.35 - 0.4 a_{\mathrm{bin}}$, when the quasi-steady eccentric state has been reached. The disk remains circular for a couple of hundred orbits, until at some point the average disk eccentricity increases abruptly reaching a temporary maximum, which is followed by a decrease. After this jump, the eccentricity curves retain their constant values, no further jumps or sudden changes occurring within the simulation time.

The evolution of the disk radius and average disk eccentricity differs fundamentally from the above-described general cases for thin ($h = 0.01$) and thick ($h = 0.1$) models, respectively. While in a thick model, the disk does not expand temporarily and the average disk eccentricity remains low, for thin models the disk eccentricity does not develop at all. Moreover, for significant binary eccentricity ($e_{\mathrm{bin}} \geq 0.2$), although the disk expands and becomes eccentric temporarily, the average disk eccentricity decays within ~ 100 subsequent binary orbits.

The final disk radius is significantly affected by the mass ratio q of the binary system in models with $0.05 \leq q \leq 0.7$ and $\alpha = 0.02$. We found that the larger the mass ratio, the smaller the final disk radius (Fig. 6.8, panel a, dashed curves). The final disk radius is in the interval $0.35 - 0.45 a_{\mathrm{bin}}$, which corresponds to 14-18 AU assuming $a_{\mathrm{bin}} = 40$ AU for binary separation. On the other hand, the magnitude of the final average disk eccentricity does not depend on q (Fig. 6.8, panel a, solid curves). We also found that the azimuthally averaged eccentricity profile are practically the same in the quasi-steady disk state for all models. The timescale of the disk eccentricity evolution shows no clear dependence on q. The eccentricity growth rate increases monotonically with increasing binary mass ratio in the range of $0.05 \leq q \leq 0.15$, while for $q \geq 0.2$ the growth rate decreases with increasing q.

To investigate the effect of the magnitude of the viscosity on the disk eccentricity evolution, we performed simulations with $0.005 \leq \alpha \leq 0.04$ and $q = 0.2$. We found that with increasing viscosity, the disk reaches a quasi-steady eccentric state at larger disk radius. The final disk radii are in the range of $0.33 a_{\mathrm{bin}} - 0.42 a_{\mathrm{bin}}$, corresponding to 13.5 AU-17 AU (Fig. 6.8, panel b, dashed curves). The magnitude of the viscosity, however, has no strong effect on the final value of the average disk eccentricity (Fig. 6.8, panel b, solid curves). Although the final azimuthally averaged disk eccentricity profiles are also very similar to each other, a slightly lower value of the final average disk eccentricity was found for the $\alpha = 0.005$ low viscosity model. On the other hand,

the time required to reach the quasi-steady eccentric disk state decreases with increasing values of α.

To investigate the effect of the initial orbital eccentricity of the binary on the disk eccentricity evolution, we performed simulations in which the secondary was placed on an initially eccentric orbit with the same apastron distance as used for circular models assuming $q = 0.2, \alpha = 0.02$. The initial eccentricity e_{bin} was in the range of 0.05-0.5. We found that the final disk radius is also sensitive to the binary eccentricity. As a general tendency, the final disk radius for an eccentric binary falls short of that of the circular binary case (Fig. 6.8, panel c, dashed curves). The final disk radius decreases with increasing binary eccentricity above $e_{\mathrm{bin}} = 0.2$. The disk becomes permanently eccentric only for $e_{\mathrm{bin}} \leq 0.2$ models, in which the final value of the average disk eccentricity is nearly the same (Fig. 6.8, panel c, solid curves). For higher binary eccentricity, the disk becomes only temporarily eccentric. There is no permanent eccentric disk state at all in $e_{\mathrm{bin}} \geq 0.2$ models. The lifetime of the temporary eccentric disk state decreases significantly with increasing binary eccentricity above $e_{\mathrm{bin}} = 0.2$.

We modeled circumstellar disks with various aspect ratios in the interval $0.01 < h < 0.1$ with $q = 0.2$ and $\alpha = 0.02$. We found that the choice of the disk aspect ratio substantially affects the final disk radius (Fig. 6.8, panel d, dashed curves), which increases with increasing h for models $0.03 \leq h \leq 0.05$, and decreases for thicker disks ($0.075 \leq h \leq 0.1$). For thick ($h = 0.1$) and thin disks ($h = 0.01$), the disk radii are stabilized early (no temporary disk puff-up being present) at ~ 17 AU and ~ 18 AU, respectively. The final average disk eccentricity displays a similar dependence on the aspect ratio as the disk radius (Fig. 6.8, panel d, solid curves). The final value of average disk eccentricity is at its largest for the $h = 0.05$ model, but for either larger or smaller aspect ratios the disk eccentricity profile is somewhat flatter. We note, however, that although the average disk eccentricity is lower for $h \geq 0.075$ than for $h = 0.05$, the azimuthally averaged eccentricity profile of the inner disk ($R < 4$ AU) is similar. For a very thick disk ($h = 0.1$), we found that there is no temporary high eccentric state, and the disk eccentricity is significantly lower than in the thinner models. We emphasize that disk eccentricity does not develop at all in the very thin disks ($h = 0.01$) case.

We also studied the eccentricity evolution for the flaring disk approximation, assuming a $\gamma = 2/7$ flaring index (Chiang & Goldreich 1997). The disk aspect ratio ($h(R) = h(a_{\mathrm{bin}})R^{\gamma}$) was $h(a_{\mathrm{bin}}) = 0.03 - 0.1$ at the distance of the secondary. In these models, the disk radius is stabilized at lower values than in the corresponding non-flaring models (Fig. 6.8, panel d, dot-dashed curves). The average disk eccentricity remains below that of the appropriate non-flaring ones, except for the

thick $h = 0.1$ disk case, where the disk eccentricity of the flaring model exceeds the appropriate non-flaring one (Fig. 6.8, panel d, dot-dot-dashed curves). Noteworthy is the significantly slower eccentricity growth rate for flaring models. In general, the azimuthally averaged disk eccentricity profiles of flared models stay below the corresponding non-flaring models, except for the thick ($h = 0.1$) model, where the flared eccentricity profile is above the corresponding non-flaring one.

The hydrodynamical equations do not depend on the disk mass since Σ_0 drops out of the hydrodynamical equations (Kley 1999). This is true as long as we use the isotherm equation of state ($p = \Sigma c_s^2$) and neglect the change in the binary orbital parameters. The gravitational potential of the secondary that perturbs the disk, however, is affected by the orbital parameters of the secondary, which might be subject to change. The magnitude of the torque exerted by the disk on the secondary indeed depends on the disk mass. Thus, the final dynamical state of the disk might be influenced by the disk-to-secondary mass ratio $q_{\text{disk/sec}}$. To investigate whether the disk mass influences the disk eccentricity evolution, we performed several simulations assuming a $0.0002 - 0.02\, M_\odot$ disk mass with $q = 0.2$ and $\alpha = 0.02$, corresponding to $0.001 \leq q_{\text{disk/sec}} \leq 0.1$. We found that the final disk radius does not depend on the initial disk mass (Fig. 6.8, panel e, dashed curves). Similarly, the final value of the average disk eccentricity is also insensitive to the disk mass (Fig. 6.8, panel e, solid curves). However, we concluded that the disk eccentricity evolution tends to begin at earlier epochs for the more massive disks. We note that the azimuthally averaged disk-eccentricity profile is practically independent of the disk mass being in the above-mentioned range. This can be explained by the changes in the orbital parameters of the secondary being negligible, i.e., $\Delta a / a_{in} < 0.001$ and $\Delta e_{\text{bin}} < 0.001$.

Finally, we investigated whether the choice of the inner boundary influences the disk eccentricity evolution. This is an important question because a feasible inner boundary condition might differ when the disk inner rim is close to or far from the primary. There are two extreme boundary conditions regarding the outflow mass flux at the inner disk edge: maximum allowed and minimum (zero) mass flux occurs for open and rigid-wall boundary conditions, respectively. An open boundary condition, in which case the mass accretion rate at the inner edge is not influenced by the star, seems to be feasible for cases when the inner disk is farther away from the star, e.g. when the inner disk is cleared by photoevaporation, for example Shu et al. (1993) and Clarke et al. (2001). When the disk inner edge is close to the stellar surface (i.e. at the magnetospheric radius) the radial velocity component of the migrating material practically vanishes owing to the equilibrium of the stellar magnetospheric pressure and the ram pressure of accreting material (Koenigl 1991). In an extreme situation, the accretion ceases, thus a perfectly rigid wall assumption might

be valid. Thus, we applied an open outflow (where both the azimuthal and the radial components of the velocity are the same in the ghost cells) and rigid inner boundary (at which the radial velocity component changes its sign without changing its magnitude in the ghost cells) conditions for model $\alpha = 0.02, q = 0.2$. Comparing the results of models with open and rigid inner boundary conditions, one can see that both the final disk radius and final averaged disk eccentricity profiles are independent of the choice of inner boundary condition (Fig. 6.8, panel f, dashed curves). The time needed to reach the quasi-steady eccentric disk state is also similar for both boundary conditions. Noteworthy is the difference in the magnitude of averaged disk eccentricity value during the temporarily high eccentricity states.

6.6 Discussion

In his pioneering work, Lubow (1991a,b) showed that tidally induced eccentricity develops in circumprimary disks of close-separation binaries because of the effect of the 3:1 eccentric inner Lindblad resonance. Kley et al. (2008) numerically investigated the eccentricity development in circumprimary disks using spatially uniform kinematic viscosity. Lubow (2010) then explored the eccentricity growth rate by linear eccentricity evolution formulated by Goodchild & Ogilvie (2006) neglecting the effect of viscosity. In our approach, however, the viscosity of the disk material is provided by the turbulence within the disk (Shakura & Sunyaev 1973), where the kinematic viscosity increases with increasing stellar distance. In what follows, we compare our results to that of Kley et al. (2008) and Lubow (2010).

6.6.1 Comparison of simulations

In line with these studies, our simulations demonstrate that the circumprimary disk becomes eccentric with final average eccentricity of $\bar{e} \simeq 0.25$, assuming α-type viscosity in the range $0.005 \leq \alpha \leq 0.04$. In good accordance with the results of Kley et al. (2008), we found that the disk's final average eccentricity does not depend on the binary mass ratio. In addition to the results of Kley et al. (2008), we confirmed these findings for mass ratios higher than 0.3. However, the time required to reach the quasi-steady eccentric disk state was found to decrease with increasing mass ratio only up to $q = 0.15$. Above this mass ratio, the disk eccentricity evolution decelerated significantly, and ever more slowly with increasing q in our simulations. Kley et al. (2008) found that the increase in the eccentricity growth rate is continuous up to $q = 0.3$. This behavior of

eccentricity growth rate can be explained if tidal forces lower the disk density near the resonance, where the eccentricity is excited, and the eccentricity growth rate then is reduced (Lubow 2010).

Lubow (2010) qualitatively expected that the eccentricity growth would accelerate as the viscosity increased because the disk is then more likely to spread outwards. Along with the results of Kley et al. (2008), we confirmed this prediction as the disk eccentricity growth rate is found to monotonically increase with α.

Kley et al. (2008) found that the disk final eccentricity decreases with decreasing values of the dimensionless kinematic viscosity up to $\nu_k \leq 10^{-5}$, while below this value the disk eccentricity is found to be saturated (Fig. 8. of Kley et al. (2008)). In the α-type viscosity approach, the kinematic viscosity is $\nu_k = \alpha h^2 R^{1/2}$. Hence, in our models the dimensionless kinematic viscosity is $2.5 \times 10^{-6} < \nu_k < 6.5 \times 10^{-5}$ within the disk radius assuming that $0.005 \leq \alpha \leq 0.04$, and a $h = 0.05$ non-flaring disk. Thus, the values of the kinematic viscosity modeled in our simulations are close to the range where the disk eccentricity is found to be independent of viscosity by Kley et al. (2008).

The evolution of the disk eccentricity departs significantly from the general trends for eccentric binaries with $e_{bin} \geq 0.2$. The 3:1 Lindblad resonance responsible for the disk eccentricity (Lubow 1991a) lies farther toward the primary, and the disk is truncated at smaller radius in an eccentric binary than in circular ones. As a consequence, the excitation of 3:1 Lindblad resonance might be inefficient, resulting in only a temporary eccentric state with maximum value of $\bar{e}_{disk} < 0.3$ that lasts for only a hundred binary orbits.

We have explored a slightly wider aspect-ratio range than Kley et al. (2008). In their investigation, the disk eccentricity displays a weaker linear increase, the aspect ratio being in the range of 0.02-0.06. Lubow (2010) concluded that the eccentricity growth rate increases with increasing sound speed, being equivalent to the disk geometrical thickness. We have confirmed this result. However, for very thick disks ($h \geq 0.75$) both the final disk eccentricity and the growth rate were found to be smaller than for the $h = 0.05$ models, meaning that the aspect ratio-eccentricity relation turns above $h = 0.75$. In addition, the disk eccentricity evolution is found to be inhibited for very thin disks ($h = 0.01$). To explain this odd relation between the disk geometrical thickness and eccentricity development, further theoretical investigation will be required in which the effect of the disk viscosity can also taken into account.

Noteworthy is the disk eccentricity evolution in flared disk models, namely, we have found that a significantly lower average disk eccentricity develops in the case of a flaring disk geometry than in a flat one. However, there is an exception, i.e., the $h(a_{bin}) = 0.1$ thick flared model, where

the resulting disk eccentricity is slightly above the corresponding non-flaring one. This may occur because a flaring disk is always thinner on average than the corresponding non-flaring one in our models. Thus, flaring disks are thinner at small R, where they are hence similar to the non-flaring models with small h, which also do not have high eccentricity.

6.6.2 Observability of the line profile asymmetry

We have shown that the eccentric circumprimary disk of a binary, containing considerable amount of gas, produces asymmetric CO ro-vibrational line profiles because of the eccentric orbits ($\bar{e}_{disk} \simeq 0.2$) of the CO emitting gas parcels. The largest line-profile asymmetry measured between the red and blue peaks of the $V = 1 \to 0$ P(10) transition is $\sim 20-25\%$, depending on the disk inclination angle. However, we keep in mind that the magnitude of the line profile asymmetry depends on the position angle of the eccentric disk on the sky with respect to the line-of-sight. To observe the largest line profile asymmetry, the disk must be aligned perpendicular with its semimajor axis to the line-of-sight (Fig. 6.6, panel a or d). Taking this consideration into account, we now present a method to determine the disk eccentricity profile by fitting the CO line profile asymmetry.

Assuming that the disk plane is aligned with the binary orbital plane (Monin et al. 2006), which is measurable by the well-known astrometric technique (Atkinson 1966), the disk inclination angle can be determined. The disk position angle on the sky can also be determined using the spectro-astrometric technique (Porter et al. 2005), which was applied successfully by Pontoppidan et al. (2008). Knowing the disk inclination and the position angle of the eccentric disk on the sky, the model degeneracy can be resolved. Taking these considerations together, one can find the best-fit disk model in terms of the disk eccentricity, using our semi-analytical spectral model presented in Regály et al. (2010). The Doppler shift of the gas parcels at a given R, ϕ point in the eccentric disk seen perpendicular to its semimajor axis and inclined by i can then be given by

$$
\begin{aligned}
\Delta\nu(R, \phi, i) \quad = \quad & \frac{\nu_0}{c} \frac{V_{\mathrm{K}}(R)}{\sqrt{1 + e(R)\cos(\phi)}} \times \\
& \{\sin(\phi) + (\cos(\phi) + e(R))\}\sin(i),
\end{aligned} \tag{6.4}
$$

where the disk eccentricity profile, $e(R)$, can be approximated by a quadratic polynomial function

$$
e_{\mathrm{disk}}(R) \simeq a_0 + a_1 R + a_2 R^2. \tag{6.5}
$$

Searching for a best-fit eccentricity profile for model #1, we found that $a_0 = -0.0385301$, $a_1 = 0.136924$, and $a_2 = -0.0092516$. Figure 6.9 shows the line profiles calculated in model #1

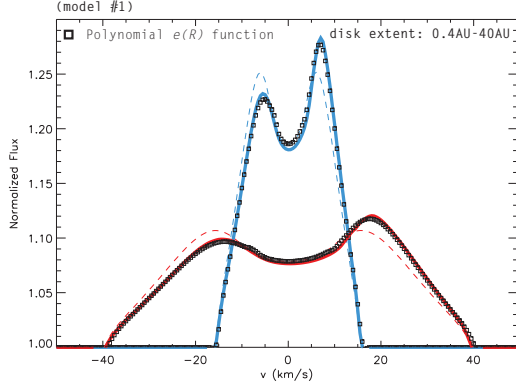*6. Spectral signatures of disk eccentricity*

FIGURE 6.9: Line profiles formed in circular Keplerian disks (dashed curves), eccentric disks using the velocity distribution given by the hydrodynamical simulations (solid curves), and eccentric disk using the best-fit eccentricity profile (squares). The line profiles are calculated for disk inclinations $i = 20°$ (blue) and $i = 60°$ (red).

using a circular Keplerian Doppler shift (solid curves) approximating the disk eccentricity using Eq. (6.4) (square symbols) befor calculating the Doppler shift. The line profiles emerging from the circular Keplerian disk are also shown (dashed curves). The line profiles are also calculated assuming $i = 20°$ (blue color) and $i = 60°$ (red color). One can see that the models using an approximated disk eccentricity (Eq. 6.5) perfectly fit the line profiles calculated by the models using the hydrodynamical velocity distributions. Consequently, the disk eccentricity profile can be estimated by searching for the best-fit model of an asymmetric CO ro-vibrational line profile, with knowledge of both the disk position angle and the disk inclination angle.

A fundamental uncertainty about the observability of eccentric circumprimary disks whether is there enough time to develop the disk eccentricity at all, before the disk is depleted in the viscous timescale? Since the disk eccentricity evolution ceases within $\sim 0.2\,\mathrm{Myr}$ in all of our models (Fig. 6.8), we expect that the eccentric state is occurred well within the disk lifetime. We search for the best-fit function of the evolution time required to reach the maximal eccentric state as a

function of the viscosity in the form of $t_{max} = a\alpha^b$, finding that $a = 0.011$ and $b = -0.47$. Thus, within limitations of our modeling, the minimum viscosity required to develop an eccentric disk in a 40 AU separation binary is $\alpha > 6.8 \times 10^{-5}, 2.2 \times 10^{-6}$, and 5×10^{-7} assuming 1 Myr, 5 Myr, and 10 Myr gas depletion timescale, respectively.

6.6.3 Disk thickness for T Tauris

As we have shown, the circumprimary disk in a binary system with $e_{bin} \leq 0.2$ undergoes a significant increase in eccentricity for an aspect ratio in the range of $0.03 \leq h \leq 0.075$, although there might be exceptional cases. The final average disk eccentricity is found to be significantly lower for thick circumprimary disks with aspect ratios of $h \geq 0.1$ (Fig. 6.8, panel d). Moreover, for thin disks ($h \leq 0.01$) the disk does not become eccentric at all. In what follows, we predict the thickness of the protoplanetary disk formed surrounding a T Tauri type star.

We assume that the gas in the circumprimary disk is in vertical hydrodynamical equilibrium. Assuming that the disk is geometrically thin (i.e., $h(R) = H/R \gg 1, R \gg R_*$), the disk aspect ratio can be given by

$$h(R) = \sqrt{\frac{kT(R)R}{\mu_g m_p GM_*}},\tag{6.6}$$

where M_* is the stellar mass, $T(R)$ is the temperature profile of the disk, k is the Boltzmann constant, $\mu_g \simeq 2.3$ is the mean molecular weight of the disk gas, and m_p is the proton mass (see e.g. Dullemond & Dominik (2004b)). In the flaring disk model of Chiang & Goldreich (1997), the disk interior temperature is

$$T(R) \simeq \left(\frac{\delta(R)}{4}\right)^{1/4} \left(\frac{R_*}{R}\right)^{1/2} T_*,\tag{6.7}$$

assuming hydrostatic and radiative equilibrium. Here the accretion heating is neglected, i.e., only the stellar irradiation is taken into account. In Eq. (6.7), $\delta(R)$ is the grazing angle of stellar irradiation entering the disk atmosphere, which can be approximated as

$$\delta(R) \simeq \frac{2}{5}\frac{R_*}{R} + \frac{8}{7}\left(\frac{T_*}{T_c}\right)^{4/7}\left(\frac{R_*}{R}\right)^{-2/7},\tag{6.8}$$

where $T_g = GM_*\mu_g/kR_*$. For T Tauri stars, one can write $(T_*/T_g)^{4/7} \simeq 0.007$. For an average T Tauri star, if $R \gtrsim 0.1$ AU, $\delta(R)$ can be approximated by the second term of the right-hand side
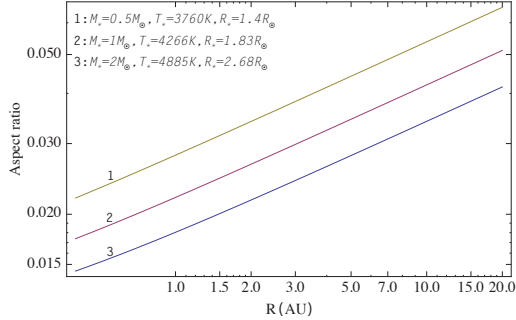
6. Spectral signatures of disk eccentricity

FIGURE 6.10: Disk aspect-ratio profiles calculated numerically using Eqs. (6.6)-(6.8) for three different mass T Tauri type stars. The stellar parameters assumed in the calculations are indicated.

of Eq. (6.8), because this term dominates the equation. After some algebra, we get

$$h(R) \simeq 0.02 \left(\frac{R_*}{R_\odot}\right)^{3/14} \left(\frac{T_*}{T_\odot}\right)^{1/2} \left(\frac{M_*}{M_\odot}\right)^{-1/2} \left(\frac{R}{\text{AU}}\right)^{4/7}. \tag{6.9}$$

Figure 6.10 shows the disk aspect ratio using Eq. (6.6)-(6.8) for three different masses of T Tauri type stars. (The stellar parameters were taken from Siess et al. (2000) assuming $2.5\,\text{Myr}$ for the stellar age.) As one can see, the disk aspect ratio increases with decreasing stellar mass, and is always above 0.01. Although the disk temperature is lower for lower mass stars, the squeezing effect of the stellar gravitational force is also smaller, resulting in a higher disk aspect ratio. Since the disk aspect ratio is $\sim 0.02 - 0.05$ on average, the disks around T Tauri type stars are thick enough to be eccentric. We note, however, that the SEDs of disks, mapping the dust rather than the gas disk around very low mass stars, can be fitted assuming significantly lower aspect ratios (Szűcs et al. 2010). Accordingly, we expect the circumprimary disks encircling a T Tauri type young primary star in a binary system with $e_{\text{bin}} \leq 0.1$ to produce asymmetric line profiles owing to the development of disk eccentricity.

6.6.4 Limits of our model

In this study we have used a simple 2D disk model, although our assumptions are reasonable to investigate the effect of dynamically perturbed circumprimary disk on CO ro-vibrational line profiles. In the hydrodynamical calculations, we have neglected the disk self-gravity. Although the Toomre parameter (Toomre 1964) is $Q \gg 1$ in our models, the disk self-gravity might modify the picture. For global disturbances, such as significant disk ellipticity, even though the disks are gravitationally stable, pressure and self-gravity can be equally important (Papaloizou 2002). In this case, the parameter measuring the importance of self-gravity becomes hQ, which is of the order of unity in our simulations. Marzari et al. (2009) found that the disk self-gravity appears to be an important factor, because when included the circumprimary disk eccentricity evolution is considerably slower than in non self-gravitating disk models. We note, however, that Marzari et al. (2009) follow the disk eccentricity evolution only to ~ 0.012 Myr, which is too short to develop significant eccentricity in our models. In addition, Adams et al. (1989) found that eccentric disk instabilities might also be excited by a process called as stimulation by the long-range interaction of Newtonian gravity for massive disks. Thus, the inclusion of self-gravity may also certainly improve our results.

For simplicity, we have assumed that the dust and gas temperature are well coupled in the disk atmosphere. However, Glassgold et al. (2004) and Kamp & Dullemond (2004) found that the dust and gas coupling ceases above the disk atmosphere. As a consequence, the gas in the tenuous region above the disk atmosphere might be significantly hotter than predicted by the double-layer model. Hence, the slowly rotating distant disk parcels above the disk atmosphere could produce a substantial contribution to the low-velocity part of the line profile, resulting in a centrally peaked profile. Nevertheless, the centrally peaked line profiles are expected to be asymmetric because of the supersonic Doppler-shift. To study the effect of the dust-gas temperature decoupling on the line profile asymmetry, a more sophisticated temperature model is needed.

We have neglected the irradiation flux coming from the secondary star. The luminosity of an 2.5 Myr old $0.3\,M_\odot$ mass secondary is $\sim 20\%$ that of the $1\,M_\odot$ primary (Siess et al. 2000). The final disk radius is $< 0.45a_{\rm bin}$ on average (Fig. 6.8), while the disk eccentricity can reach $e \simeq 0.4$ at the disk edge (Fig. 6.2, panel d). Thus, the minimal distance between the disk apastron-edge and the secondary is $> 0.37a_{\rm bin}$, taking into account the eccentric disk shape. This distance corresponds to 14.8 AU and 7.5 AU for model #1 and model #2, respectively. At these distances, the CO ro-vibrational fundamental band is not excited thermally by the secondary irradiation.

Therefore, the effect of the secondary's irradiation on the CO line profiles should be investigated only for close-separation ($< 20\,\text{AU}$) binaries.

A recent survey of Taurus medium-separation young binaries revealed that their secondary infrared fluxes are commensurable to their primary ones (Pascucci et al. 2008), hence, young binaries might have also circumsecondary disks. In some cases, the infrared flux of a circumsecondary disk is equal to that of the primary, and the common spectra of a system may also contain the presumably distorted line profiles of the secondary. To investigate these systems, more elaborate hydrodynamical simulations, incorporating the secondary's disk are needed.

As mentioned in Sect. 2., the secondary star induces a tidal wave during close encounters in each orbit. The gas is significantly compressed inside these temporary waves, as the density enhancement can reach two orders of magnitudes, according to our hydrodynamical simulations. Since the gas might be heated to temperatures high enough to excite the CO, the secondary mass flow might have a significant impact on the CO line profiles. Thus, to investigate the effect of the secondary mass flow on the line profile asymmetry, we need to incorporate the energy conservation in the 2D hydrodynamical simulations, which will be the subject of an upcoming paper.

6.6.5 Outlook

Spectroscopy of T Tauri stars detects the emission of molecules such as H_2O, OH, HCN, C_2H_2, and CO_2. Nevertheless, CO is more abundant than any of these molecules by a factor of ~ 10. Only H_2O could reach the abundance of CO predicted by recent models that calculate the vertical chemical structure of the gas in disk atmosphere (e.g., Glassgold et al. (2004), Kamp & Dullemond (2004), and Woitke et al. (2009)). In some cases, such as AA Tau (Carr & Najita 2008), and both AS 205A and DR Tau (Salyk et al. 2008), the rotational transitions of H_2O dominate the mid-infrared ($10 - 20\,\mu\text{m}$) spectra, implying that H_2O is abundant in disk atmospheres. In contrast to theoretical predictions, strong water emission could be the consequence of turbulent mixing that carries molecules from disk midplane, where they are abundant, to the disk atmosphere (Carr & Najita 2008), or the effects of an enhanced mechanical heating of the atmosphere (Glassgold et al. 2009). While the CO and H_2O ro-vibrational lines provide information about the inner regions of disk out to radii 2-3 AU, their rotational lines are excited in the radii range 10-100 AU (Meijerink et al. 2008; Beckwith & Sargent 1993). As the disk eccentricity beyond 3 AU might be large, $e_{\text{disk}} \geq 0.4$ (see, e.g., Fig. 6.2, panel d), the rotational lines are also subject to large distortions owing to the disk eccentricity. Thus, it is worthwhile to search for asymmetric line

profiles emerging from young binaries not only in the ro-vibrational spectra of CO and H_2O, but also in the rotational spectra of CO and H_2O. However, as the H_2O is heated by stellar X-rays and sub-thermally populated beyond 0.3 AU, X-ray heating and non-LTE level population treatment is needed to calculate water lines (e.g., Meijerink et al. (2008); Kamp et al. (2010)). The calculation of asymmetric mid-infrared rotational molecular line profiles emerging from young binaries will be the subject of a future study. Another interesting disk diagnostic tool could be the [OI] 6300 line. The stellar UV photons incident on the disk atmosphere are thought to photodissociate OH and H2O, producing a non-thermal population of excited neutral oxygen that decays radiatively. As a result, [OI] emission lines emerge from the disk atmosphere, as reported by Acke et al. (2005) for Herbig Ae/Be stars.

6.7   Summary

We have examined the effects of a secondary star on a gas-rich protoplanetary disk encircling the primary based on the previous work of Lubow (1991a,b) and Kley et al. (2008). While Kley at al. used spatially constant viscosity ν, we have assumed a α-type viscosity (Shakura & Sunyaev 1973), which has a spatial dependence given by $\nu \sim R^{1/2}$. According to our results, the circum-primary disk eccentricity begins to increase after the first couple of hundreds of binary orbits. We have found that the disk eccentricity grows to a certain maximum value, begins to decline, and then stabilizes at $\bar{e}_{\text{disk}} \simeq 0.2 - 0.35$. During the eccentricity growth, the disk extends and shrinks back to 0.35-0.45 times the binary separation. By the time the disk reaches a quasi-steady eccentric state, the surface density profile, the disk truncation radius, as well as the eccentricity profile no longer evolve.

We have found that the final average disk eccentricity is independent of the binary mass ratio in the range $0.05 \leq q \leq 0.7$ (Fig. 6.8, panel a), of the magnitude of α in the range $0.005 \leq \alpha \leq 0.02$ (Fig. 6.8, panel b), of the disk aspect ratio for non-flaring models with $0.03 \leq h \leq 0.075$ (Fig. 6.8, panel d), of the disk-to-secondary mass ratio in the range $0.001 \leq q_{\text{disk/sec}} \leq 0.1$ (Fig. 6.8, panel e), and of the choice of the inner boundary conditions (open outflow or rigid) (Fig. 6.8, panel f). In contrast, the disk eccentricity is lower for thick disks with aspect ratios above $h = 0.1$, while disk eccentricity does not develop at all for thin disks with $h \leq 0.01$ (Fig. 6.8, panel d). The disk average eccentricity is $\bar{e}_{\text{disk}} \simeq 0.2$ for a flaring geometry with flaring index $\gamma = 2/7$, while $\bar{e}_{\text{disk}} \simeq 0.35$ for non-flaring models assuming a reasonable $h(a_{\text{bin}}) \simeq 0.05$ for the disk aspect ratio (Fig. 6.10). We emphasize that the disk becomes eccentric only temporarily for models assumed

to have an eccentric binary orbit with $e_{\mathrm{bin}} \geq 0.2$. Thus, the binary's orbital eccentricity protects the disk against eccentricity formation that might inhibit the planet formation.

In the eccentric disk, the orbit of gas parcels is non-circular, rather than elliptic. The average disk eccentricity is $\bar{e}_{\mathrm{disk}} \simeq 0.2$ inside 2-3 AU (see, Fig. 6.2, panel d), where the ro-vibrational fundamental band of CO is excited by the primary's irradiation. Combining our hydrodynamical simulation with our semi-analytic double-layer disk model (Regály et al. 2010), we have calculated the fundamental band $V = 1 \rightarrow 0$ P10 ro-vibrational line profile of $^{12}\mathrm{C}^{16}\mathrm{O}$ at $4.75\,\mu\mathrm{m}$ emerging from the superheated disk atmosphere. Since the emission spectra of the CO is strongly affected by the supersonic Doppler shift, the CO line profiles emerging from the eccentric disk are asymmetric departing from their well-known symmetric double-peaked form (Horne & Marsh 1986). We have found that the maximum peak-to-peak asymmetry is $A_{\mathrm{pp}} \simeq 20\%$ for our models, which is above the detection limit of today's high-resolution mid-IR instruments such as CRIRES (Kaeufl et al. 2004). The peak-to-peak asymmetry exhibits periodic variations as the disk precesses on the timescale of several times the binary period (Fig. 6.7). As the disk precession period is several hundred decades in medium-separation binaries, the detection of peak-to-peak asymmetry variations is improbable within a decade. On the other hand, the slight variations seen on the line wings (Fig. 6.7) have periods shorter than the binary period, which thus might be detected.

6.8 Conclusion

Our study of both the hydrodynamic and eccentricity evolution of the circumprimary disk in medium-separation young binary systems has revealed the following findings:

(1) The quasi-steady eccentric disk state always develops in circumprimary disks of young medium-separation $(20 - 40\,\mathrm{AU})$ binaries within the average disk lifetime, if the viscosity is between widely accepted values $(0.01 \leq \alpha \leq 0.1)$.

(2) The CO line profiles are asymmetric $(A_{\mathrm{pp}} \simeq 20\%)$ as the average disk eccentricity is $\bar{e}_{\mathrm{disk}} \simeq 0.2$ inside 2-3 AU, where the CO is excited by the primary's irradiation.

(3) The orbital eccentricity of binary systems $e_{\mathrm{bin}} \geq 0.2$ or their high/low disk geometrical thickness $(h \leq 0.01/h \geq 0.1)$ might inhibit the development of the quasi-static disk eccentric state.

(4) The inner ($R \leq 2 - 3\,\mathrm{AU}$) disk eccentricity profile can be determined by fitting the observed high-resolution near-IR CO line profile asymmetry using a simple 2D spectral model.

Consequently, taking into account that the eccentricity of protoplanetary disks might strongly influence planet formation, by measuring it we might further constrain the planet formation theories in medium-separation binaries.

6. Spectral signatures of disk eccentricity

7. SUMMARY

A summary of my findings on the *detectability of giant planets still embedded in their hosting disk* and the *spectral signatures of disk eccentricity in young medium-separation binaries* have been given as an oral presentation held at IAU Symposium No. 276. In this Chapter, an abridged edition of Regály et al. (2010) is presented.

Scientific goals – Theories of planet formation predict the birth of giant planets in the inner, dense, and gas-rich regions of the circumstellar disks around young stars. These are the regions from which strong CO emission is expected. Observations have so far been unable to confirm the presence of planets caught in formation. It is well known that circular Keplerian protoplanetary disks are expected to produce symmetric double-peaked molecular line profiles (Horne & Marsh 1986). Contrary to this simple symmetric disk assumption, asymmetric CO line profiles in the fundamental band have been observed in several cases. Grid-based numerical simulations of Kley & Dirksen (2006) have shown that local disk eccentricity might form in planet bearing disk near the gap. The theory of resonant excitation mechanisms in accretion disks of Lubow (1991a) predicts that the circumstellar disks of close-separation young binaries might become fully eccentric due to the orbiting companion. Horne (1995) has shown that supersonic turbulence might cause observable line profile distortions. As the orbital velocity of gas parcels is highly supersonic in accretion disks, the disk eccentricity results in supersonic velocity distortions. Therefore distorted molecular line profiles are expected to form in giant planet bearing locally eccentric protoplanetary disks (Regály et al. 2010) and fully eccentric circumstellar disks of close-separation young binaries (Regály et al. 2011). This dissertation presents my investigations on the development of disk eccentricity (local for planet bearing disks, or global for young binaries) assuming α-prescription for the disk viscosity (Shakura & Sunyaev 1973), and the near-infrared ($4.7\,\mu$m) synthetic CO spectra calculated in non circular Keplerian, eccentric disks.

Spectral calculations combined with hydrodynamic simulations – In order to calculate the CO

spectra, we need to know the temperature distribution in the disk. In my study the double-layer flaring disk model of Chiang & Goldreich (1997) is assumed. In this model the disk is heated by the stellar irradiation and accretion processes. The incident stellar flux heats the disk atmosphere, which reprocesses the stellar light and irradiates the disk interior. The accretion processes heats the disk interior directly. In this way an optically thick interior and an optically thin atmosphere can be distinguished (Fig. 7.1). For low accretion rate, temperature inversion forms, resulting in emission spectra.
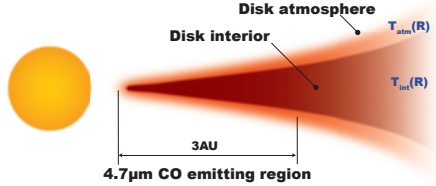
FIGURE 7.1: The double-layer disk model in which the disk atmosphere is superheated.

The fundamental band CO emission is formed in the optically thin disk atmosphere above the optically thick cooler disk interior. In the optically thin approximation the $I(\nu, R, \phi)$ monochromatic intensity of the radiation at frequency ν from a given gas parcel at R, ϕ cylindrical coordinates is the sum of the dust continuum of the disk interior and the optically thin atmospheric CO emission

$$I(\nu, R, \phi, i) = B(\nu, T_d(R))e^{-\tau(\nu, R, \phi, i)} + B(\nu, T_g(R))(1 - e^{-\tau(\nu, R, \phi, i)}), \quad (7.1)$$

where, $B(\nu, T)$ is the Planck function, $T_d(R)$ and $T_g(R)$ are the dust and gas temperatures in the disk interior and the disk atmosphere, respectively. Details of the spectral model can be found in Regály et al. (2010). For a disk perturbed by a companion (a planet or a secondary star) the velocity field is no longer circular Keplerian, in which case the local Doppler shift that affects the atmospheric optical depth ($\tau(\nu, R, \phi, i)$) can be given by

$$\Delta\nu(R, \phi, i) = \frac{\nu_0}{c}\sin(i)\left\{[u_{\rm R}(R, \phi)\cos(\phi) - u_\phi(R, \phi)\sin(\phi)] + [u_{\rm R}(R, \phi)\sin(\phi) + u_\phi(R, \phi)\cos(\phi)]\right\}, \quad (7.2)$$

where $u_R(R, \phi)$ and $u_\phi(R, \phi)$ are the radial and the azimuthal velocity components of the orbiting gas parcels. In order to calculate the local Doppler shift in a perturbed disks with embedded planet or a secondary star, the continuity and Navier-Stokes equations are solved by the 2D grid-based hydrodynamic code FARGO (Masset 2000). In this way, the $u_R(R, \phi)$ and $u_\phi(R, \phi)$ velocity components of gas parcels, were provided by the hydrodynamic simulations. For simplicity we used an isothermal equation of state for the gas. The α-type disk viscosity was applied (Shakura & Sunyaev 1973). The disk self-gravitation was neglected as the Toomre parameter is well above 1. For more details on the hydrodynamic simulations see Regály et al. (2010).
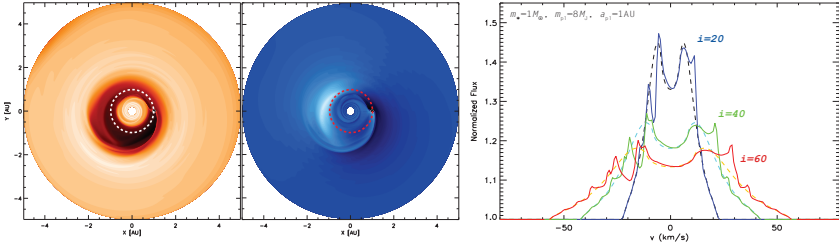
FIGURE 7.2: Surface density (*left panel*) and radial component of velocity (*middle panel*) distribution in a planet bearing protoplanetary disk. Distorted $V = 1 \rightarrow 0\,\mathrm{P10}$ CO lines (*right panel*) emerging from the gravitationally distorted disk, assuming $20°$, $40°$ and $60°$ disk inclinations.

Planetary signal: local disk eccentricity due to a giant planet – According to my simulations the density distribution shows permanent elliptic shape near the gap (Fig. 7.2, left panel), confirming the results of Kley & Dirksen (2006). I found that the orbits of gas parcels are eccentric in the vicinity of the planet (Fig. 7.2, middle panel). As the magnitude of the velocity distortion of the gas parcels exceeds the local sound speed, distorted non-symmetric line profiles are expected to form.

I have calculated the fundamental band P10 non-blended CO line for 20, 40 and 60 degree of disk inclination in a perturbed disk assuming an $8M_{\mathrm{Jup}}$ mass planet orbiting $1\,M_\odot$ mass star at
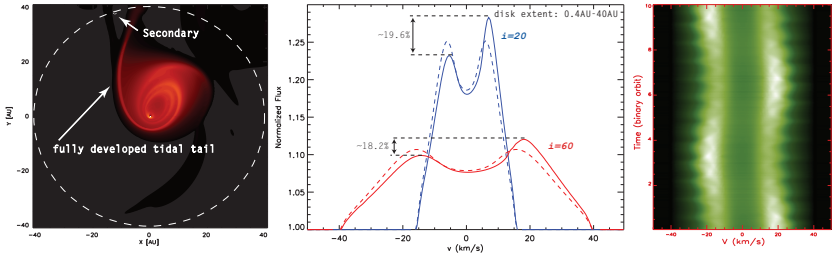
FIGURE 7.3: The circumprimary disk becomes eccentric due to the perturbations from the secondary. Asymmetric $V = 1 \rightarrow 0$ P10 CO line (*middle panel*), assuming $20°$ and $60°$ disk inclinations. Trailed spectra (*right panel*) covering a full disk precession shows the periodic variations in asymmetry with $\sim 6.5 P_{\text{bin}}$ and line wings with $\sim P_{\text{bin}}$.

1 AU (Fig. 7.2, right panel). The line shape is distorted and the relative strength of the distortions are increasing with increasing inclination angle. Calculating the line profiles with different orbital positions of the planet, we have found that the line shapes vary as the planet is orbiting.

In order to investigate the dependence of the line profile distortions on the model parameters, I have calculated the CO emission in several models assuming different planetary and stellar masses, and orbital distance of the planet. I found that the planetary and the stellar mass affect the line profiles by the same means: the larger the planetary or stellar mass, the stronger the distortion. The line profile distortion is found to be weakening with increasing orbital distance. According to our calculations, the signal of a Jovian planet orbiting a solar mass star at a distance of 1 AU can be detected with CRIRES (Regály et al. 2010).

Asymmetric lines: fully eccentric disk due to a secondary star – Circumprimary disks in young binaries become fully eccentric via the gravitational perturbations of the secondary, in form of resonant excitation mechanisms (Lubow 1991a; Kley et al. 2008)). Thébault et al. (2006) and Paardekooper et al. (2008) have shown that the planetesimal accretion might be inhibited by the disk eccentricity in core-accretion models. Recently, Zsom et al. (2011) have shown that the dust

coagulation process is also affected by the disk eccentricity in the core-accretion scenario.

According to my simulations, the average disk eccentricity is ~ 0.3 independently on the binary mass ratio and the magnitude of viscosity, assuming $h = 0.05$ aspect ratio for the disk, which is a reasonable assumption for a circumstellar disk around an average T Tauri star (Fig. 7.3, left panel). However, smaller disk eccentricity was found for thick ($h \geq 0.75$) and thin ($h \leq 0.03$) disks. I have found that the orbital eccentricity of the binary above 0.2 inhibits the development of disk eccentricity.

Calculating the $V = 1 \rightarrow 0 \, \text{P} 10$ non-blended CO lines with $20°$ and $60°$ disk inclination angle, we have found a maximum $\sim 20\%$ red-blue peak asymmetry (Fig. 7.3, middle panel). The profile asymmetry is due to the fact that the inner disk, where the fundamental band CO emission is formed, is fully eccentric. The peak asymmetry is inverted twice during a full disk precession, which takes about $\sim 6.5 P_{\text{bin}}$. Moreover, as the disk eccentricity slightly varies during one binary orbit, line profile variations might be observed in the line wings with $\sim P_{\text{bin}}$.

Future plans – I intend to continue my research in this interesting field and prove my concepts on indirect detection of embedded planets in protoplanetary disks and the determination of disk's eccentricity in young binary stellar systems. In 2010 and 2011, I was the principal investigator of two approved ESO-VLT/CRIRES proposals aiming at the indirect detection of giant planets embedded in disks (program 085.C-0736, in period 85A) and the determination of the disk's eccentricity in young binary systems (program 087.C-0462, in period 87A).

In program 085.C-0736 we detected the near-infrared spectra of two transitional disks (HD 135344 B and SR 21) in several epochs. Pontoppidan et al. (2008) have already been performed high spatial resolution spectro-astrometric observations of the 4.7 μm ro-vibrational lines of CO gas in the disk of these sources, but only in one epoch. The CO spectra of the two targets show clear deviations from Keplerian rotation profiles which were confirmed by Grady et al. (2009) for HD 135344 B. Reduction and the analysis of the high-resolution near-infrared spectra of the two sources are under way. Hoping the success, I plan to extend planet search to other young disks with CRIRES.

In program 087.C-0462 we will observe the CO spectra of four young medium-separation binary systems (RXJ1601.8-2445, RXJ1602.9-2022, ScoPMS 023, and ScoPMS 042a) of the Upper Scorpius star-forming region in the near-infrared wavelengths. We were granted 10 hour of telescope time, during which the CO lines will be measured in 4 different slit positions allowing

7. Summary

spectro-astrometric observation. By detecting departures from the symmetric Keplerian double-peaked line profiles with the help of spectro-astrometry the eccentricities of circumprimary disks will be inferred. Confronting the inferred eccentricity of the targets to the other physical parameters such as the mass ratio, separation, orbital eccentricity, etc., we intend to give constraints on the planet formation theories.

ACKNOWLEDGEMENTS

7. Summary

BIBLIOGRAPHY

Acke, B., van den Ancker, M. E., & Dullemond, C. P. 2005, A&A, 436, 209

Adams, F. C., Lada, C. J., & Shu, F. H. 1987, ApJ, 312, 788

Adams, F. C., Ruden, S. P., & Shu, F. H. 1989, ApJ, 347, 959

Akeson, R. L., Boden, A. F., Monnier, J. D., et al. 2005, ApJ, 635, 1173

Alibert, Y., Mordasini, C., & Benz, W. 2004, A&A, 417, L25

Andrews, S. M. & Williams, J. P. 2005, ApJ, 631, 1134

Andrews, S. M. & Williams, J. P. 2007, ApJ, 659, 705

Artymowicz, P. & Lubow, S. H. 1994, ApJ, 421, 651

Atkinson, R. d. 1966, PASP, 78, 242

Balbus, S. A. & Hawley, J. F. 1991, ApJ, 376, 214

Bate, M. R. & Bonnell, I. A. 1997, MNRAS, 285, 33

Beckwith, S. V. W. & Sargent, A. I. 1993, ApJ, 402, 280

Beckwith, S. V. W., Sargent, A. I., Chini, R. S., & Guesten, R. 1990, AJ, 99, 924

Biller, B. A., Kasper, M., Close, L. M., Brandner, W., & Kellner, S. 2006, ApJ, 641, L141

Blum, J. & Wurm, G. 2008, ARA&A, 46, 21

Bodenheimer, P. & Pollack, J. B. 1986, Icarus, 67, 391

Bonavita, M. & Desidera, S. 2007, A&A, 468, 721

BIBLIOGRAPHY

Boss, A. P. 2001, ApJ, 563, 367

Boss, A. P. 2006, ApJ, 641, 1148

Bouvier, J., Alencar, S. H. P., Harries, T. J., Johns-Krull, C. M., & Romanova, M. M. 2007, in Protostars and Planets V, ed. B. Reipurth, D. Jewitt, & K. Keil, 479–494

Brandl, B. R., Lenzen, R., Pantin, E., et al. 2008, in Society of Photo-Optical Instrumentation Engineers (SPIE) Conference Series, Vol. 7014, Society of Photo-Optical Instrumentation Engineers (SPIE) Conference Series

Brannigan, E., Takami, M., Chrysostomou, A., & Bailey, J. 2006, MNRAS, 367, 315

Brittain, S. D., Najita, J. R., & Carr, J. S. 2009, ApJ, 702, 85

Brittain, S. D., Simon, T., Najita, J. R., & Rettig, T. W. 2007, ApJ, 659, 685

Calvet, N., Hartmann, L., Kenyon, S. J., & Whitney, B. A. 1994, ApJ, 434, 330

Cameron, A. G. W. 1978, Moon and Planets, 18, 5

Carr, J. S. 2007, in IAU Symposium, Vol. 243, IAU Symposium, ed. J. Bouvier & I. Appenzeller, 135–146

Carr, J. S. & Najita, J. R. 2008, Science, 319, 1504

Chauvin, G., Lagrange, A., Dumas, C., et al. 2004, A&A, 425, L29

Chauvin, G., Lagrange, A., Dumas, C., et al. 2005a, A&A, 438, L25

Chauvin, G., Lagrange, A., Udry, S., et al. 2006, A&A, 456, 1165

Chauvin, G., Lagrange, A., Zuckerman, B., et al. 2005b, A&A, 438, L29

Chiang, E. I. & Goldreich, P. 1997, ApJ, 490, 368

Cieza, L. A., Padgett, D. L., Allen, L. E., et al. 2009, ApJ, 696, L84

Clarke, C. J. & Armitage, P. J. 2003, MNRAS, 345, 691

Clarke, C. J., Gendrin, A., & Sotomayor, M. 2001, MNRAS, 328, 485

Correia, A. C. M., Udry, S., Mayor, M., et al. 2008, A&A, 479, 271

D'Angelo, G., Lubow, S. H., & Bate, M. R. 2006, ApJ, 652, 1698

Deeg, H. J., Ocaña, B., Kozhevnikov, V. P., et al. 2008, A&A, 480, 563

Draine, B. T. & Lee, H. M. 1984, ApJ, 285, 89

Dullemond, C. P. & Dominik, C. 2004a, A&A, 417, 159

Dullemond, C. P. & Dominik, C. 2004b, A&A, 421, 1075

Dullemond, C. P., Dominik, C., & Natta, A. 2001, ApJ, 560, 957

Duquennoy, A. & Mayor, M. 1991, A&A, 248, 485

Eggenberger, A. & Udry, S. 2010, in EAS Publications Series, Vol. 41, EAS Publications Series, ed. T. Montmerle, D. Ehrenreich, & A.-M. Lagrange, 27–75

Eisner, J. A., Hillenbrand, L. A., White, R. J., Akeson, R. L., & Sargent, A. I. 2005, ApJ, 623, 952

Eisner, J. A., Hillenbrand, L. A., White, R. J., et al. 2007, ApJ, 669, 1072

Eisner, J. A., Monnier, J. D., Tuthill, P., & Lacour, S. 2009, ApJ, 698, L169

Fang, M., van Boekel, R., Wang, W., et al. 2009, A&A, 504, 461

Foulkes, S. B., Haswell, C. A., Murray, J. R., & Rolfe, D. J. 2004, MNRAS, 349, 1179

Frank, J., King, A., & Raine, D. J. 2002, Accretion Power in Astrophysics: Third Edition, ed. Frank, J., King, A., & Raine, D. J.

Glassgold, A. E., Meijerink, R., & Najita, J. R. 2009, ApJ, 701, 142

Glassgold, A. E., Najita, J., & Igea, J. 2004, ApJ, 615, 972

Goldreich, P. & Tremaine, S. 1980, ApJ, 241, 425

Goodchild, S. & Ogilvie, G. 2006, MNRAS, 368, 1123

Goorvitch, D. 1994, ApJS, 95, 535

Grady, C. A., Schneider, G., Sitko, M. L., et al. 2009, ApJ, 699, 1822

Greaves, J. S., Richards, A. M. S., Rice, W. K. M., & Muxlow, T. W. B. 2008, MNRAS, 391, L74

Haisch, Jr., K. E., Lada, E. A., & Lada, C. J. 2001, ApJ, 553, L153

Hartigan, P. & Kenyon, S. J. 2003, ApJ, 583, 334

Hartigan, P., Strom, K. M., & Strom, S. E. 1994, ApJ, 427, 961

Hartmann, L. 1998, Accretion Processes in Star Formation, ed. Hartmann, L.

Hartmann, L., Hewett, R., & Calvet, N. 1994, ApJ, 426, 669

Hartmann, L. & Kenyon, S. J. 1996, ARA&A, 34, 207

Hatzes, A. P., Cochran, W. D., Endl, M., et al. 2003, ApJ, 599, 1383

Hawley, J. F., Gammie, C. F., & Balbus, S. A. 1995, ApJ, 440, 742

Herbig, G. H. 1977, ApJ, 217, 693

Hillenbrand, L. A. 2005, STScI Symposium Series 19, A Decade of Discovery: Planets Around Other Stars, ed. M. Livio (Cambridge: Cambridge Univ. Press), arXiv:astro-ph/0511083

Horne, K. 1995, A&A, 297, 273

Horne, K. & Marsh, T. R. 1986, MNRAS, 218, 761

Huang, S. 1972, ApJ, 171, 549

Huélamo, N., Figueira, P., Bonfils, X., et al. 2008, A&A, 489, L9

Isella, A. & Natta, A. 2005, A&A, 438, 899

Jang-Condell, H. & Boss, A. P. 2007, ApJ, 659, L169

Johnson, B. M. & Gammie, C. F. 2005, ApJ, 635, 149

Jonkheid, B., Faas, F. G. A., van Zadelhoff, G.-J., & van Dishoeck, E. F. 2004, A&A, 428, 511

Kaeufl, H.-U., Ballester, P., Biereichel, P., et al. 2004, in Society of Photo-Optical Instrumentation Engineers (SPIE) Conference Series, Vol. 5492, Society of Photo-Optical Instrumentation Engineers (SPIE) Conference Series, ed. A. F. M. Moorwood & M. Iye, 1218–1227

Kalas, P., Graham, J. R., Chiang, E., et al. 2008, Science, 322, 1345

Kamp, I. & Dullemond, C. P. 2004, ApJ, 615, 991

Kamp, I., Tilling, I., Woitke, P., Thi, W., & Hogerheijde, M. 2010, A&A, 510, A18+

Kashyap, V. L., Drake, J. J., & Saar, S. H. 2008, ApJ, 687, 1339

Kenyon, S. J. & Hartmann, L. 1987, ApJ, 323, 714

Klahr, H. 2008, New Astronomy Review, 52, 78

Kley, W. 1999, MNRAS, 303, 696

Kley, W. & Dirksen, G. 2006, A&A, 447, 369

Kley, W., Papaloizou, J. C. B., & Ogilvie, G. I. 2008, A&A, 487, 671

Koenigl, A. 1991, ApJ, 370, L39

Kokubo, E. & Ida, S. 1998, Icarus, 131, 171

Krotkov, R., Wang, D., & Scoville, N. Z. 1980, ApJ, 240, 940

Kuiper, G. P. 1951, Proceedings of the National Academy of Science, 37, 1

Lagrange, A., Beust, H., Udry, S., Chauvin, G., & Mayor, M. 2006, A&A, 459, 955

Lagrange, A., Gratadour, D., Chauvin, G., et al. 2009a, A&A, 493, L21

Lagrange, A., Kasper, M., Boccaletti, A., et al. 2009b, A&A, 506, 927

Lee, J. W., Kim, S., Kim, C., et al. 2009, AJ, 137, 3181

Lequeux, J. 2005, The interstellar medium, ed. Lequeux, J.

Lin, D. N. C. & Papaloizou, J. 1980, MNRAS, 191, 37

Lin, D. N. C., Papaloizou, J. C. B., & Kley, W. 1993, ApJ, 416, 689

Lodato, G. 2008, New A Rev., 52, 21

Lubow, S. H. 1991a, ApJ, 381, 259

Lubow, S. H. 1991b, ApJ, 381, 268

Lubow, S. H. 2010, MNRAS, 406, 2777

Lubow, S. H. & D'Angelo, G. 2006, ApJ, 641, 526

Lynden-Bell, D. & Pringle, J. E. 1974, MNRAS, 168, 603

Marois, C., Macintosh, B., Barman, T., et al. 2008, Science, 322, 1348

Marzari, F., Scholl, H., Thébault, P., & Baruteau, C. 2009, A&A, 508, 1493

Masset, F. 2000, A&AS, 141, 165

Mathis, J. S., Rumpl, W., & Nordsieck, K. H. 1977, ApJ, 217, 425

Meijerink, R., Poelman, D. R., Spaans, M., Tielens, A. G. G. M., & Glassgold, A. E. 2008, ApJ, 689, L57

Monin, J., Ménard, F., & Peretto, N. 2006, A&A, 446, 201

Monnier, J. D., Berger, J., Millan-Gabet, R., et al. 2006, ApJ, 647, 444

Mordasini, C., Alibert, Y., & Benz, W. 2009, A&A, 501, 1139

Mukhopadhyay, B. 2008, International Journal of Modern Physics D, 17, 467

Muzerolle, J., Calvet, N., Hartmann, L., & D'Alessio, P. 2003, ApJ, 597, L149

Najita, J., Carr, J. S., & Mathieu, R. D. 2003, ApJ, 589, 931

Najita, J. R., Carr, J. S., Glassgold, A. E., & Valenti, J. A. 2007, in Protostars and Planets V, ed. B. Reipurth, D. Jewitt, & K. Keil, 507–522

Najita, J. R., Crockett, N., & Carr, J. S. 2008, ApJ, 687, 1168

Narayanan, D., Kulesa, C. A., Boss, A., & Walker, C. K. 2006, ApJ, 647, 1426

Natta, A. 1993, ApJ, 412, 761

Natta, A., Prusti, T., Neri, R., et al. 2001, A&A, 371, 186

Nelson, A. F. 2000, ApJ, 537, L65

Nelson, R. P., Papaloizou, J. C. B., Masset, F., & Kley, W. 2000, MNRAS, 318, 18

Neuhäuser, R., Guenther, E. W., Wuchterl, G., et al. 2005, A&A, 435, L13

Paardekooper, S., Thébault, P., & Mellema, G. 2008, MNRAS, 386, 973

Papaloizou, J. & Lin, D. N. C. 1984, ApJ, 285, 818

Papaloizou, J. & Pringle, J. E. 1977, MNRAS, 181, 441

Papaloizou, J. C. B. 2002, A&A, 388, 615

Papaloizou, J. C. B., Nelson, R. P., & Masset, F. 2001, A&A, 366, 263

Pascucci, I., Apai, D., Hardegree-Ullman, E. E., et al. 2008, ApJ, 673, 477

Paulson, D. B. & Yelda, S. 2006, PASP, 118, 706

Pollack, J. B., Hubickyj, O., Bodenheimer, P., et al. 1996, Icarus, 124, 62

Pontoppidan, K. M., Blake, G. A., van Dishoeck, E. F., et al. 2008, ApJ, 684, 1323

Popham, R., Narayan, R., Hartmann, L., & Kenyon, S. 1993, ApJ, 415, L127

Popham, R., Narayan, R., Kenyon, S. J., & Hartmann, L. 1995, in Revista Mexicana de Astronomia y Astrofisica, vol. 27, Vol. 1, Revista Mexicana de Astronomia y Astrofisica Conference Series, ed. S. Lizano & J. M. Torrelles, 229–+

Porter, J. M., Oudmaijer, R. D., & Baines, D. 2005, in Astronomical Society of the Pacific Conference Series, Vol. 337, The Nature and Evolution of Disks Around Hot Stars, ed. R. Ignace & K. G. Gayley, 299–+

Prato, L., Huerta, M., Johns-Krull, C. M., et al. 2008, ApJ, 687, L103

Queloz, D., Mayor, M., Weber, L., et al. 2000, A&A, 354, 99

Raghavan, D., McAlister, H. A., Henry, T. J., et al. 2010, ApJS, 190, 1

Regaly, Z., Kiss, L., Sandor, Z., & Dullemond, C. P. 2010, ArXiv e-prints

Regály, Z., Sándor, Z., Dullemond, C. P., & Kiss, L. L. 2011, A&A, 528, A93+

Regály, Z., Sándor, Z., Dullemond, C. P., & van Boekel, R. 2010, A&A, 523, A69+

Rice, W. K. M., Armitage, P. J., Wood, K., & Lodato, G. 2006, MNRAS, 373, 1619

Rodmann, J., Henning, T., Chandler, C. J., Mundy, L. G., & Wilner, D. J. 2006, A&A, 446, 211

Rybicki, G. B. & Lightman, A. P. 1986, Radiative Processes in Astrophysics, ed. Rybicki, G. B. & Lightman, A. P.

Safronov, V. S. 1972, Akademiia Nauk SSSR Vestnik, 10, 97

Salyk, C., Blake, G. A., Boogert, A. C. A., & Brown, J. M. 2009, ApJ, 699, 330

Salyk, C., Pontoppidan, K. M., Blake, G. A., et al. 2008, ApJ, 676, L49

Schmidt, T. O. B., Neuhäuser, R., Seifahrt, A., et al. 2008, A&A, 491, 311

Setiawan, J., Henning, T., Launhardt, R., et al. 2008, Nature, 451, 38

Shakura, N. I. & Sunyaev, R. A. 1973, A&A, 24, 337

Shu, F. H., Johnstone, D., & Hollenbach, D. 1993, Icarus, 106, 92

Siess, L., Dufour, E., & Forestini, M. 2000, A&A, 358, 593

Skrutskie, M. F., Dutkevitch, D., Strom, S. E., et al. 1990, AJ, 99, 1187

Smak, J. 1981, Acta Astron., 31, 395

Stahler, S. W. & Palla, F. 2005, The Formation of Stars, ed. Stahler, S. W. & Palla, F.

Statler, T. S. 2001, AJ, 122, 2257

Szűcs, L., Apai, D., Pascucci, I., & Dullemond, C. P. 2010, ApJ, 720, 1668

Thébault, P., Marzari, F., & Scholl, H. 2006, Icarus, 183, 193

Toomre, A. 1964, ApJ, 139, 1217

Varnière, P., Bjorkman, J. E., Frank, A., et al. 2006, ApJ, 637, L125

Veras, D., Crepp, J. R., & Ford, E. B. 2009, ApJ, 696, 1600

Ward, W. R. 1997, ApJ, 482, L211

Weidenschilling, S. J. 1977, MNRAS, 180, 57

Weingartner, J. C. & Draine, B. T. 2001, ApJ, 548, 296

Wetherill, G. W. & Stewart, G. R. 1989, Icarus, 77, 330

Woitke, P., Kamp, I., & Thi, W. 2009, A&A, 501, 383

Wolf, S. & D'Angelo, G. 2005, ApJ, 619, 1114

Wolf, S., Moro-Martín, A., & D'Angelo, G. 2007, Planet. Space Sci., 55, 569

Zsom, A., Sándor, Z., & Dullemond, C. P. 2011, A&A, 527, A10+

Zucker, S., Mazeh, T., Santos, N. C., Udry, S., & Mayor, M. 2004, A&A, 426, 695